Orbital evolution of levitated regolith particles in the 65803 Didymos binary system

Master of Science Thesis
Aleksander Fiuk

Technische Universiteit Delft

TU Delft

Orbital evolution of levitated regolith particles in the 65803 Didymos binary system

Master of Science Thesis

by

Aleksander Fiuk

to obtain the degree of Master of Science
at the Delft University of Technology,
to be defended publicly on Tuesday December 20, 2022 at 13:00.

Student number:	5149363	
Project duration:	February 3, 2021 – December 20, 2022	
Thesis committee:	Dr. SM Cazaux	TU Delft, chair
	Dr.ir. MJ Heiligers,	TU Delft, daily supervisor
	Dr. S Soldini,	University of Liverpool, external supervisor
	Ir. BTC Zandbergen	TU Delft, committee member

Cover photo: Asteroid moonlet Dimorphos as seen by the DART spacecraft 11 seconds before impact.
Courtesy of NASA/Johns Hopkins APL (source: `https://www.nasa.gov/`, accessed on Nov 26th, 2022).

Abstract

Modern technology provides the humanity with possibilities unimaginable just a few decades ago; one of such is the fact that space technology is considered mature enough to be used in a seemingly science-fiction scenario of a planetary defense mission. AIDA, a joint project of NASA and ESA, comprises two segments: NASA's impactor spacecraft DART and ESA's probe Hera. The primary scientific objectives of the AIDA mission are (1) to demonstrate the kinetic impact technique - one of the planetary defense methods to protect Earth from hazardous impacts, and (2) to study the dynamical environment of the Didymos system - a binary asteroid, which is the target of both spacecraft. The Didymos system is composed of Didymos, the primary asteroid, and Dimorphos, the much smaller secondary body. The DART spacecraft has impacted into Dimorphos on September 26th, 2022. The Hera spacecraft is expected to arrive to the Didymos system in late 2026 and perform *in situ* observations of the asteroids to study their properties and further investigate the effects of DART's collision.

To ensure successful execution of the Hera segment of the mission, the risk of collision with naturally-levitated regolith grains is studied to enable well-informed planning of *in situ* operations of the probe. A method to identify regions of high collision risk is proposed. As an example, results for a 5 cm radius of regolith particles is presented in the study. The assessment method comprises of (1) identification of regions of bounded motion, i.e., orbital neighborhoods in which particles may survive for extended periods of time or even follow quasi-orbit-like trajectories, (2) determination of regions of regolith levitation from the asteroidal surface followed by an analysis of their post-levitation fates, and (3) exploration of the trajectories connecting the initial states upon levitation and the final states in the bounded-motion trajectories. Two dynamical models are introduced. The augmented bicircular problem (ABP) is an expansion of the bicircular four-body problem obtained by substituting the point-mass gravity fields with spherical-harmonics models of ellipsoidal primaries, applying solar-radiation pressure and third-body perturbances. The ABP is used for trajectory propagation within the binary. However, to ensure convergence of the adopted dynamical model within the Brillouin sphere (BS) of the primary bodies, a proximity dynamical model (PDM) is introduced - a modification of the augmented bicircular problem, in which the spherical-harmonics gravity field of Didymos is substituted by a mass-concentration model.

The identification of levitation regions and determination of the fates of levitated particles are conducted using the PDM, when the motion takes place within Didymos's BS, and ABP elsewhere. In a study conducted on 16 sets of initial states of the system, an increased rate of escape from the binary is observed among the analyzed trajectories in certain states of the system. A gravity-assisted slingshot mechanism, i.e., a phenomenon of changing the path and velocity of a regolith grain by the gravitational pull of Dimorphos, is suggested as a rationale for this observation. The results show that a significant amount of levitated mass is anticipated to be transferred to the surface of the lesser body of the binary system. Surprisingly, the distribution of the regolith grains on Dimorphos is found to be favoring the non-Didymos-facing half of this tidally-locked moonlet. Moreover, levitated regolith particles are found to collide with the primary at all longitudes along the equator. This strongly suggests a complex mechanism of approximately uniform regolith relocation in the equatorial regions, which effectively slows down the depletion of the regolith material from Didymos.

A grid analysis in search for periodic orbits results in the demonstration of successful application of this technique to identify bounded-motion trajectories in the system. The grid search is conducted only for one set of initial state of the binary system represented in the ABP framework. Four of the most precise solutions are given as the results of this study. They include two quasi-satellite orbits and two distant retrograde orbits.

The distances between trajectories following the off-Didymos levitation of the grains and the trajectories of bounded motion are investigated. The methodology presented in this work does not render conclusive results with regards to the existence or absence of temporary-capture trajectories in the adopted model.

The primary region of hazard to the spacecraft is the vicinity of the ecliptic plane of the system. Three types of regolith particle trajectories that might be of significant hazard to the Hera spacecraft are identified: (1) levitated trajectories destined to escape the binary, (2) chaotic, non-periodic survived trajectories of particles levitated from Didymos, and (3) levitated particles captured into periodic orbits. Analysis of the results obtained in the study suggests the existence of two dust disks around the binary system: (1) the outer disk is composed of regolith particles following the escaping trajectories, it is uniform in density and highly ordered

as the particles follow similar outbound, spiral trajectories, whereas (2) the inner disk spans as far as 20 km from the barycenter of the binary, the motion of particles in this disk is chaotic, which drives the fluctuations in density. Given the small escape rates of the dust from the system after levitation, the regolith relocation mechanism proposed in this work suggests that the inner disk is an ever-changing, dynamic, and self-exciting dust cloud that may cause the most significant and unpredictable risk for the Hera spacecraft.

The study is based on several assumptions, such as the assumption of planar motion of the Sun around the binary, constant distance to the Sun, and the simplified shape of the primaries. Moreover, the range of diameters of particles under consideration may be expanded and applying multiple-shooting methods for identifying periodic orbit may be investigated. Furthermore, the recent arrival of the DART probe to the binary is expected to deliver much more detailed data on the binary and remove numerous uncertainties pointed out in this work.

Contents

List of Figures

List of Tables

List of Symbols

Physical quantities

(r, λ, δ)	normalized spherical coordinates: radius, inclination, azimuth [(-, deg, deg)]
(x, y, z)	Cartesian coordinates [-]
$\ddot{r}^*$	characteristic acceleration [ms^{-2}]
$\hat{\mathbf{S}}$	third body-pointing unit vector [-]
$\mathbb{R}$	rotation matrix [-]
$\mathbf{D}$	augmented state space [-]
$\mathbf{r}$	position vector in $\mathscr{F}$ [-]
$\mathbf{T}$	translation vector [-]
$\mathbf{x}, \mathbf{X}$	state vector and augmented state vector in $\mathscr{F}$
$\mathscr{F}$	reference frame [-]
$\tilde{C}_{\mathbf{X}}$	interpolated state history matrix of augmented state vector $\mathbf{X}$ [-]
$\underline{A}, \underline{B}, \underline{C}$	factors of a polynomial expression [-]
A	orbital semi-major axis [m]
a, b, c	ellipsoid semi-axes [m]
C	Jacobi integral of motion [-]
c_l	speed of light [ms^{-1}]
C_p	pressure coefficient [-]
$C_{\mathbf{X}/\mathbf{x}}$	state history matrix of augmented state vector $\mathbf{X}$/state vector $\mathbf{x}$ [-]
$C_{k,l}$	Stokes coefficient of k-th degree and l-th order [-]
D	semi-axis extent [m]
d	distance [-]
D^*	semi-axis extent of a Dynamically Equivalent Equal Volume Ellipsoid [m]
e	orbital eccentricity [-]
f	mean orbital motion [rad/h]
F, F_S	Cartesian and spherical functions describing an ellisoid [-]
G	universal gravitational constant [m^{3}s^{-2}kg^{-1}
i	orbital inclination [deg]
m	mass [kg]
M^*	characteristic mass [kg]

N	number of particles [-]
n	fraction of a total number of particles N [-]
R	distance to the Sun [m]
r	normalized distance [-]
R^*	characteristic distance [m]
R_{ell}	ellipsoid radius [-]
s	sigmoid contrast factor [-]
T	period [-]
t	time [-]
U	normalized gravity potential [-]
v	speed/magnitude of velocity [ms^{-2}]
V^*	characteristic velocity [ms^{-2}]
W_E	solar constant [Wm^{-2}

(λ, δ)	longitude, latitude [(deg, deg)]
(Λ_b, B_b)	orbital pole coordinates [(deg, deg)]
α	experienced slope [deg]
α_e	angle of rotation of an ellipse [deg]
β	SRP effective coefficient [-]
ϵ	relative error [-]
Λ	orientation of the primary body [rad]
Ω	angular velocity vector of the synodic frame [rad/-]
μ	mass parameter [-]
$\mu_{D/d}$	normalized mass of Didymos/Dimorphos [-]
Ω	angular rate of the synodic frame [rad/-]
Ω_s	revolution rate of a third body [rad/-]
ϕ	third-body azimuthal position in the synodic frame [rad]
Π	mesh size [-]
ψ	orbital obliquity [deg]
ρ	density [kg m^{-3}]
σ	area-to-mass ratio [m^{2}kg^{-1}]
τ	normalized time [-]
$\tilde{\mu}_{D/d}$	finite-density distribution of normalized mass of Didymos/Dimorphos [-]
$\tilde{\sigma}$	sigmoid function [-]

φ	arbitrary real number [-]
ξ	mass concentrations offset from the surface [-]

Superscripts

$*$	characteristic quantity

Subscripts

b	related to the binary system
D	Didymos
d	Dimorphos
E	Earth
e	eclipse
ell	ellipsoid
ext	extremum
h	related to the heliocentric orbit
i	generic notation for quantities referring to one of the primaries
l	levitation trajectory-related quantity
M_D, M_d	related to the non-spherical mass distribution of Didymos/Dimorphos
min, max	minimum, maximum value
o	periodic orbit-related quantity
p	related to the test particle
$proj$	projected value
ref	reference value

Other

$\ddot{\square}$	second time derivative
$\dot{\square}$	first time derivative
$\tilde{\square}$	quantity interpolated as a t-function
$\underline{\square}$	dimensional value of a normalized variable $\square$

List of Abbreviations

Abbreviation	**Definition**
AIAA	American Institute of Aeronautics and Astronautics
ABP	Augmented Bicircular Problem
AIDA	Asteroid Impact and Deflection Assessment
AU	Astronomical Unit
BDF	Backward-Differentiation Formula integrator
BP	Bi-circular Problem
BS	Brillouin Sphere
CR3BP	Circular-Restricted Three-Body Problem
CYM	Spherical-Earth Cylindrical Model
DART	Double Asteroid Redirection Test
DEEVE	Dynamically Equivalent Equal Volume Ellipsoid
DOP853	Runge-Kutta integrator with Dormand-Prince coefficients (Dormand-Prince method)
DO	Distant Orbit
DRO	Distant Retrograde Orbit
ESA	European Space Agency
JAXA	Japanese Aerospace Exploration Agency
LSODA	Adams/BDF method with automatic stiffness detection and switching
MC	Mass-Concentration gravity model
MOID	Minimum Orbit Intersection Distance
NASA	National Aeronautics and Space Administration
NEA	Near-Earth Asteroid
NEO	Near-Earth Object
PDM	Proximity Dynamical Model

Abbreviation	**Definition**
PHA	Potentially Hazardous Asteroid
PHO	Potentially Hazardous Object
QSO	Quasi-Satellite Orbit
RK(n)	(n-th order) Runge-Kutta integrator
SB3BP	Shape-Based Three-Body Problem
SH	Spherical Harmonics
SOI	Sphere of Influence
SRP	Solar Radiation Pressure

Preface

The graduation day and completion of this work mark an immensely important milestone for me both professionally and personally. The past two years have been a very maturing and challenging journey for me and I would like to acknowledge the support I have received.

Małgosia and Maciek, thank you for guiding me and watching me grow until this point. I owe you more than I could put on paper; therefore, it's better to say nothing. Just thank you.

Kacper, thank you for your wisdom despite your young age. You may have not realized but you've grown to be a man - a man I admire.

Tosia, thank you for the unconditional patience, warmth and support. I am truly grateful that I can be sharing this journey with you and become a better person every day thanks to you.

Filippo, Marco, Michał, we have come a long way together and I am looking forward to the rest of it. Building a space superpower can only be achieved by the power of hard work, trust, and a lekkerbek followed by a stroopwafel (there is no way around it). I cannot think of anyone else with whom it would be possible to work this hard, whom I'd trust as much, and who'd enjoy a lekkerbek followed by a stroopwafel just as much. Every day, I learn new things from you and grow as an engineer and as a friend.

Jeannette and Stefania, thank you for your remarkable supervision of my graduation project and allowing me to grow professionally on the way. You have always shown great personal support, understanding, and care; this means a lot to me.

Pippo, we have shared the ride together. Thank you for always being there and having my back (maybe besides the intermittent fasting you impose by making me wait for the 1am dinners).

There are still plenty of people I would like to express my gratitude to, either for helping me become the person I am now, or for your support in improving as an engineer. Let this go to all of you not named in this preface: thank you!

Aleksander Fiuk
Delft, December 2022

1

Introduction

Planetary defense is a branch of science and technology whose primary task is to monitor, evaluate and establish plans of mitigation risks from outer space. One of the most significant hazards is posed by a group of asteroids categorized as Near-Earth Asteroids (NEAs), i.e., asteroids of orbital perihelion within 1.3au from the Sun [16]. Past missions to minor bodies, like JAXA's Hayabusa that collected samples from 25143 Itokawa in 2005 (Figure 1.1a) or comet-directed NASA's DIXI/EPOXI (Figure 1.1b) and ESA's Rosetta missions (Figure 1.1c), have delivered answers to many fundamental questions regarding the formation of the Solar System [18]. Two missions are in progress at the moment of writing; JAXA's Hayabusa2 returned to Earth samples collected on 162173 Ryugu and is now on its way to 1998 KY_{26} (Figure 1.1e), whereas NASA's OSIRIS-REx probe is on its way to Earth with samples collected from the surface of 101955 Bennu (Figure 1.1d) - all three of these objects fall under the label of NEAs [18]. Among the Near-Earth Asteroids, one can distinguish Potentially Hazardous Asteroids (PHAs) defined as (1) NEAs of approximately 150 m in diameter and (2) characterized by a Minimum Orbit Intersection Distance (MOID) of 0.05 au, i.e., approximately 7.5 million kilometers or less, which stands for the miss distance between the PHA and Earth at any point in time - past or future [8].

The Asteroid Impact and Deflection Assessment mission (AIDA), which started in late 2021 with the launch of the Double Asteroid Redirection Test (DART) spacecraft, is composed of two segments: NASA's DART spacecraft, which on September 26th, 2022 has impacted the lesser of the two bodies of the 65803 Didymos binary asteroid system (an overview of the kinetic impact test is given in Figure 1.2a), and ESA's Hera probe, which will arrive to the binary system four years after the impact and study its effects *in situ* [3, 21] (more details on the mission's itinerary are given in Figure 1.2b). The Didymos binary system is classified as a PHA (the heliocentric orbit of Didymos is shown in Figure 1.3). The system is composed of two asteroids: Didymos of approximately 800 m in diameter [17] and the significantly smaller Dimorphos of about 160 m in diameter [1]. Based on information available for other binary systems, it is believed that the Didymos system secondary body is in a 1:1 spin-orbit ratio, i.e., in tidal lock. A detailed shape model of Didymos is derived from radar measurements [2, 9]; however, due to the small size of Dimorphos, the radar-derived model of the lesser body bears much larger uncertainties and the shape of the moonlet is approximated by an ellipsoid [2, 9].

There is a 0.01% chance every year of a surface impact of a 100 m NEA, which could most likely result in a tsunami travelling thousands of kilometers from the impact spot, and a 0.000001% change of a collision with a body greater than 10 km in size, potentially leading to massive extinction [8]. The presented probabilities are small in the context of the absolute magnitude of these numbers, but given that they signify massive destruction of whole regions or even a doomsday scenario - the danger should not be ignored. Therefore, AIDA is a highly awaited mission by the planetary defense community, since it aims at demonstrating the technology of kinetic deflection of a hazardous object from its Earth-endangering trajectory [10]. The impact should result in an observable change in the orbital state of the system, enabling evaluation of the outcome through Earth-based observations [21].

The objectives of the European segment of AIDA are to investigate the effects of DART's impact, study the binary system in terms of the physical properties of both bodies, and support side experiments, i.e., several CubeSats ridesharing on Hera will be deployed in the Didymos system to autonomously perform their missions [10]. However, planning the trajectories and operations that the probes will follow within the binary is a complex task due to large uncertainties associated with the currently known properties of the binary. One of the main hazards is caused by the large probability of existence of loose dust particles in the binary system. Loose regolith may be levitated from the surface of the large body; Yu et al. [28, 30, 31] discuss the reaccretion of particles ejected by the DART's impact and investigate necessary conditions for shedding of particles from the surface of Didymos. Upon potential levitation, such particles may follow four different fates: (1) redeposit on the surface of the larger body, (2) leave the system, (3) transfer and deposit on the surface of the lesser body, or (4) experience temporary capture in an orbit in the system. Since particles trapped in orbits in the binary may result in accumulation of unquantified clouds of loose regolith, the latter fate of the ejecta is of the largest concern from the perspective of mission risk analysis. Zhang et al. [32] discuss the interaction between the particles composing internal layers of Didymos and their impact on the potential existence and properties of the levitated regolith particles. Several studies focus on orbital motion in Didymos; Capannolo et al. [5], Lasagni Manghi et al. [14], Oliveira and Prado [20], Jean et al. [12], Silva Neto et al. [23], and Dell'Elce et al. [7] identify periodic orbits in the Didymos binary system using various dynamical models. Successful identification of temporary capture around other small bodies have been demonstrated. Scheeres et al. [22] demonstrate an approach to analyze the capturing of particles following the Deep Impact experiment on the comet Tempel 1. Villegas Pinto et al. [26] present a methodology to identify temporary capture of particles ejected from asteroid Ryugu by the Small Carry-on Impactor (SCI) operation as part of JAXA's Hayabusa2 mission. Soldini et al. [24] discuss the survivability of SCI ejecta particles in 1:1 resonance orbits around Ryugu. However, to the best knowledge of the author, a study of temporary capture of naturally-levitated regolith particles in the Didymos system has not been conducted. Thus, a knowledge gap is identified and this research is devoted to address it.

1.1. Research objective

The objective of the research is

> *to investigate the risk to the Hera spacecraft from the regolith particle collisions by studying the orbital evolution and fates of loose, naturally-levitated regolith particles in the Didymos binary system with particular attention devoted to temporary capture in orbits in the binary system.*

1.2. Research questions

Among recent studies of the Didymos binary by Oliveira and Prado [20], Capannolo et al. [5], Dell'Elce et al. [7], Lasagni Manghi et al. [14], and Silva Neto et al. [23], none of the mentioned studies performs a broader search for regions of bounded motion using a higher-fidelity model and a possibility of temporary capture therein. As Damme et al. [6] and Yu et al. [29] demonstrate, the irregularity in the gravity fields of the primaries, the solar radiation pressure (SRP), and the third-body effect due to Sun's gravity have significant impact on the dynamics within the Didymos system.

The main research question reflects the knowledge gaps identified in this chapter as well as the primary research objective formulated in section 1.1:

> *"What are the conditions for the levitated particles to evolve into trajectories posing risk to a spacecraft in the Didymos binary system and what is the topology of the orbital evolution thereof?"*

The main research question is further divided into sub-questions, which aim to specify several aspects of the main question, on which the focus will be put in the research.

> *Q*1 *"What are the regions of Didymos' mass loss?"*

---

[1] `https://planetary.s3.amazonaws.com/assets/images/spacecraft/2018/20180215_hayabusa-at-itokawa.jpg (access: 27.11.2022)`

[2] `https://www.mdscc.nasa.gov/wp-content/uploads/2019/08/206499main_DI_Rawlings_lgweb.jpg (access: 27.11.2022)`

[3] `https://blogs.esa.int/rosetta/files/2014/05/Rosetta_Philae_Artist_Impression_Close_2k.jpg (access: 27.11.2022)`

[4] `https://www.nasa.gov/images/content/639978main_OsirisRex-Printstill1.jpg (access: 27.11.2022)`

[5] `https://wp.technologyreview.com/wp-content/uploads/2020/12/Hayabusa2.jpg (access: 27.11.2022)`

[6] `https://dart.jhuapl.edu/Mission/index.php (access: 27.11.2022)`

[7] `https://www.heramission.space/scenario (access: 27.11.2022)`

[8] `www.esa.int/var/esa/storage/images/esa_multimedia/images/2019/02/didymos_orbit/19243540-1-eng-GB/Didymos_orbit_large.jpg (access: 27.11.2022)`

Q2 "Under which conditions can ejecta be temporarily captured in periodic or bounded orbits?"

Q3 "What trajectories do the dust particles follow and, as result of that, what are the regions of higher collision risk in the context of AIDA?"

It is reckoned that addressing the research questions specified in this section may significantly contribute to the mission concept of ESA's segment of AIDA and will constitute a substantial added value to the field of astrodynamical research of binary asteroid systems.

1.3. Report structure

The essential part of this thesis report is written in the format of a journal paper manuscript following the guidelines of the American Institute of Aeronautics and Astronautics (AIAA)[9]. The manuscript titled "Orbital evolution of regolith ejecta in binary asteroid systems applied to 65803 Didymos" constitutes chapter 2 of this report. As a stand-alone research work, the paper contains its own abstract and introduction sections, followed by the discussion of methods used throughout the research, analysis of the results, and conclusions. Chapter 3 discusses the conclusions, reflects on the conducted analysis in light of the posed research questions, and presents the recommendations for future work. In appendix A, methods of verification and validation of the dynamical models (section A.1) and numerical integration (appendix A.2) are discussed. Appendix B presents the methodology and results of the selection of the numerical integration scheme used in the research.

---

[9] `https://www.overleaf.com/latex/templates/tagged/aiaa-official` (access: 03.02.2021)

(a) Hayabusa mission [1]

(b) DIXI/EPOXI mission [2]

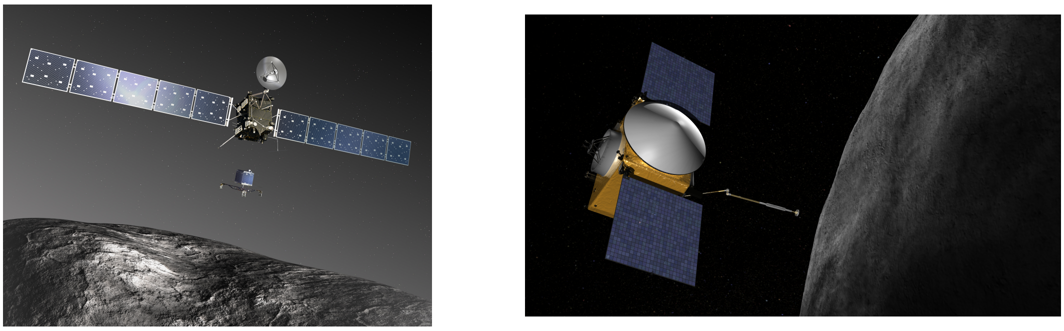

(c) Rosetta mission [3]

(d) OSIRIS-REx mission [4]

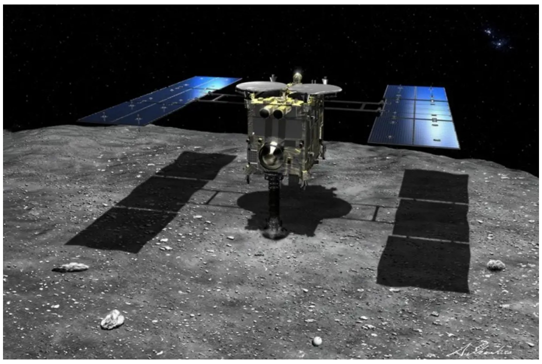

(e) Hayabusa2 mission [5]

Figure 1.1 Historical missions to asteroids

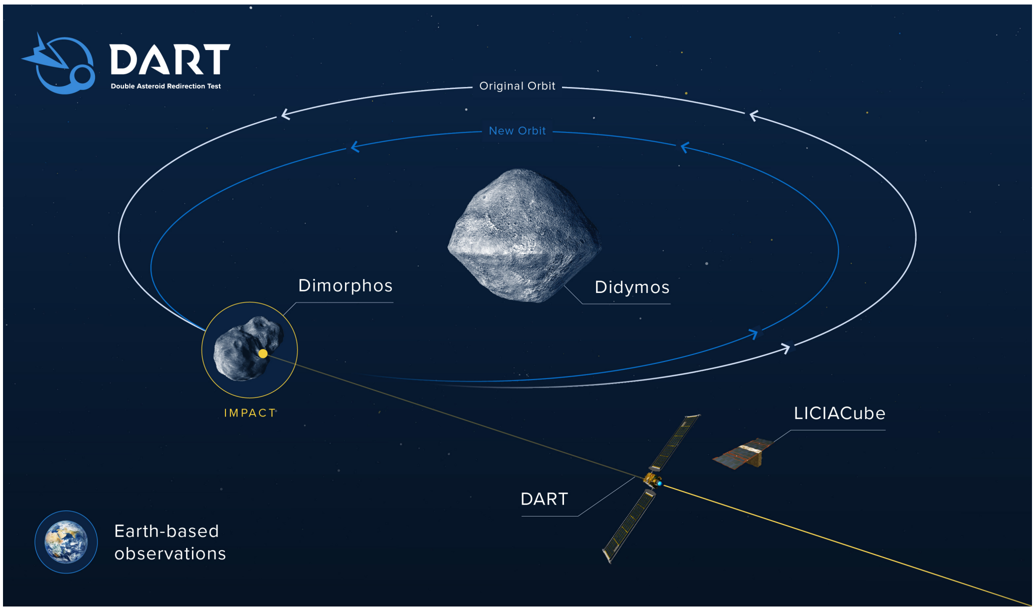

(a) DART mission - an overview infographic [6]

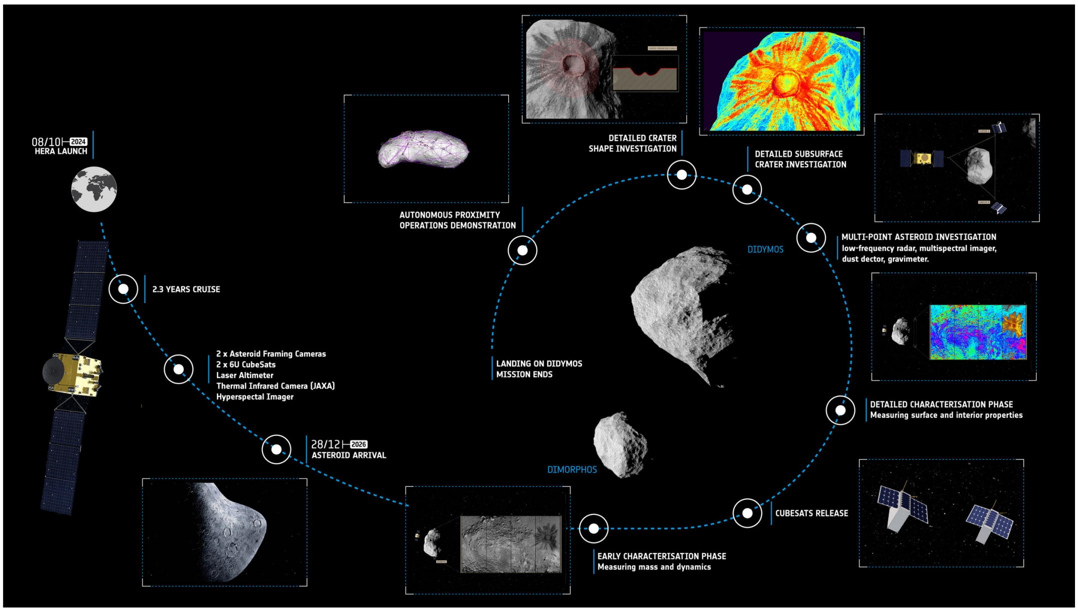

(b) Hera mission - an overview infographic [7]

Figure 1.2 Overview of the two segments of the AIDA mission

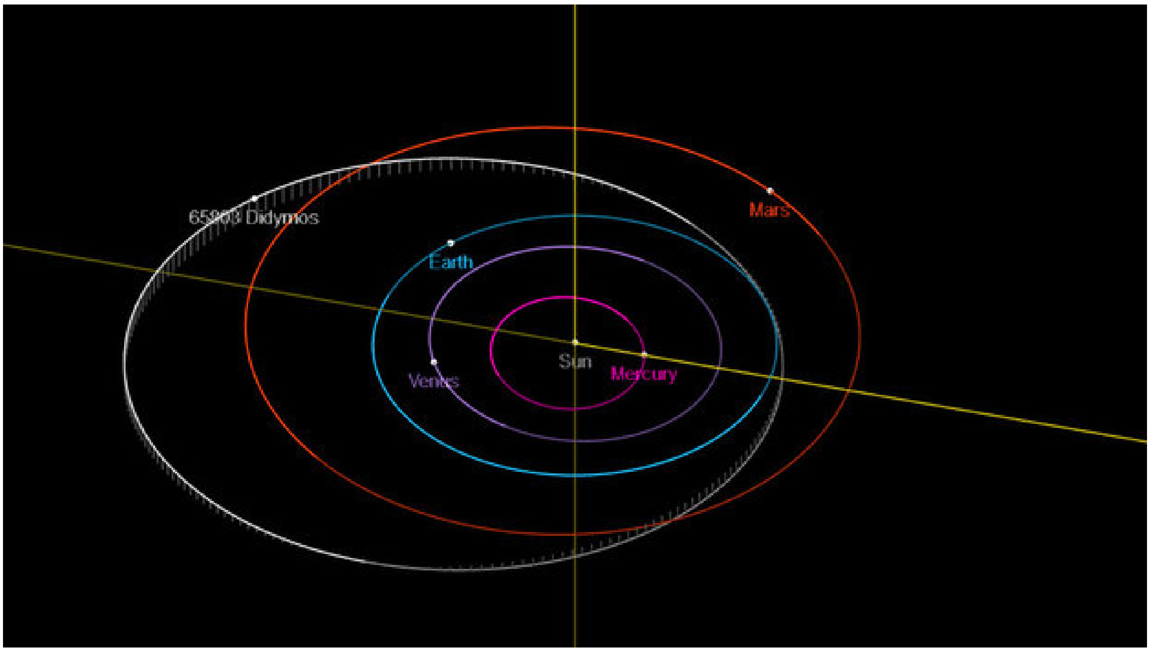

Figure 1.3 Heliocentric orbit of Didymos [8]

2

Journal article

This chapter is the main part of this thesis report. The self-contained journal paper manuscript starts on the following page.

Orbital evolution of levitated regolith particles in the 65803 Didymos binary system

Aleksander Fiuk *
Delft University of Technology, Delft, the Netherlands

Operating a spacecraft in a strongly perturbed environment of a binary asteroid system is a challenging task. In this context, risk of collision with free-floating regolith grains is one of the least studied problems. In light of the near-future exploration of the 65803 Didymos binary system by the Hera probe and the lack of study of orbital evolution of naturally-levitated regolith particles in the Didymos system, a method is here proposed to identify such regions of high collision risk. The assessment method comprises (1) determination of regions of regolith levitation from the asteroidal surface, (2) identification of regions of stable motion, i.e., orbital neighborhoods in which particles may survive for extended periods of time, and (3) exploration of the trajectories connecting the initial states upon levitation and the final states in the stable-motion trajectories. Periodic orbits and regions of stable motion are computed through a grid search method applied in the augmented bicircular problem, i.e., a dynamical model that constitutes an expansion of the bicircular four-body problem by substituting the point-mass gravity fields with spherical-harmonics models of ellipsoidal primaries, applying solar-radiation pressure and third-body perturbances. The investigation of the regions of regolith levitation is conducted using a proximity dynamical model - a modification of the augmented bicircular problem, in which the spherical-harmonics gravity field of Didymos is substituted by a mass-concentration model in order to assure convergence at the surface of the primary body. The distance between trajectories leading from the off-surface levitation of the grains from the primary body and the trajectories of bounded motion is then assessed. The methodology presented in this work does not render conclusive results with regards to the existence or absence of temporary-capture trajectories in the adopted model. A qualitative evaluation of the expected patterns of motion of regolith particles is here presented together with a discussion of the key conclusions in the context of *in situ* operations planning for the Hera probe. The primary region of hazard to the spacecraft is identified to be the vicinity of the ecliptic plane of the system. As a result of the study, the Hera spacecraft is found to be under hazard of collision with regolith particles (1) in trajectories escaping from the binary

---

*A.Fiuk@student.tudelft.nl

system and (2) in long-term chaotic motion after levitation from Didymos. Existence of two dust disks is suggested, where the inner disk spans up to 20 km from the center of the binary system and the outer disk is formed by the particles slowly spiraling out of the binary system. The inner disk is identified as the larger risk to the spacecraft than the outer one due to its chaotic character and significantly larger expected density.

Nomenclature

a, b, c = ellipsoid semi-axes [m]

A = orbital semi-major axis [m]

$\underline{A}, \underline{B}, \underline{C}$ = factors of a polynomial expression [-]

$C_{k,l}$ = Stokes coefficient of k-th degree and l-th order [-]

c_l = speed of light [$\mathrm{m\,s^{-1}}$]

C_p = pressure coefficient [-]

$C_{\mathbf{X}/\mathbf{x}}$ = state history matrix of augmented state vector $\mathbf{X}$/state vector $\mathbf{x}$

$\tilde{C}_{\mathbf{X}}$ = interpolated state history matrix of augmented state vector $\mathbf{X}$

d = distance [-]

D = semiaxis extent [m]

D^* = semiaxis extent of a Dynamically Equivalent Equal Volume Ellipsoid [m]

$\mathbf{D}$ = augmented state space [-]

e = orbital eccentricity [-]

f = mean orbital motion [$\mathrm{rad\,h^{-1}}$]

F, F_S = Cartesian and spherical functions describing an ellisoid [-]

$\mathcal{F}$ = reference frame [-]

G = universal gravitational constant [$\mathrm{m^3\,s^{-1}\,kg^{-2}}$]

i = orbital inclination [deg]

m = mass [kg]

M^* = characteristic mass [kg]

n = fraction of a total number of particles N [-]

$\hat{\mathbf{n}}$ = normal vector [-]

N = number of particles [-]

R = distance to the Sun [m]

R^* = characteristic distance [m]

r = normalized distance or radius [-]

$\ddot{r}^*$ = characteristic acceleration [$\mathrm{m\,s^{-2}}$]

(r, λ, δ) = normalized spherical coordinates: radius, inclination, azimuth [(-,deg,deg)]

$\mathbf{r}$ = position vector [-]

$\mathbb{R}$ = rotation matrix [-]

s = sigmoid contrast factor [-]

$\hat{\mathbf{S}}$ = third body-pointing unit vector [-]

t = time [-]

t^* = characteristic time [s]

T = period [-]

$\mathbf{T}$ = translation vector [-]

U = normalized gravity potential [-]

v = speed/magnitude of velocity [-]

V^* = characteristic velocity [$\mathrm{m\,s^{-1}}$]

W_E = solar constant [$\mathrm{W\,m^{-2}}$]

(x, y, z) = Cartesian coordinates [-]

$\mathbf{x}, \mathbf{X}$ = state vector and augmented state vector in $\mathcal{F}$

α = experienced slope [deg]

α_e = angle of rotation of an ellipse [deg]

β = SRP effective coefficient [-]

ϵ = relative error [-]

(λ, δ) = longitude, latitude [(deg,deg)]

(Λ_b, B_b) = orbital pole coordinates [(deg,deg)]

Λ = orientation of the primary body [rad]

μ = mass parameter [-]

$\mu_{D/d}$ = normalized mass of Didymos/Dimorphos [-]

$\tilde{\mu}_{D/d}$ = finite-density distribution of normalized mass of Didymos/Dimorphos [-]

ϕ = third-body azimuthal position in the synodic frame [rad]

φ = arbitrary real number [-]

ψ = orbital obliquity [deg]

ρ = density [$\mathrm{kg\,m^{-1}}$]

σ = area-to-mass ratio [$\mathrm{m\,kg^{-2}}$]

$\tilde{\sigma}$ = sigmoid function [-]

τ = normalized time [-]

$\boldsymbol{\Omega}$ = angular velocity vector of the synodic frame $[\mathrm{rad}/-]$

Ω = angular rate of the synodic frame $[\mathrm{rad}/-]$

Ω_s = revolution rate of a third body $[\mathrm{rad}/-]$

Subscripts

b = related to the binary system

D = Didymos

d = Dimorphos

E = Earth

e = eclipse

ell = ellipsoid

ext = extremum

h = related to the heliocentric orbit

i = generic notation for quantities referring to one of the primaries

l = levitation trajectory-related quantity

min, max = minimum, maximum value

M_D, M_d = related to the non-spherical mass distribution of Didymos/Dimorphos

o = periodic orbit-related quantity

p = related to the test particle

$proj$ = projected value

ref = reference value

Superscripts

$*$ = characteristic quantity

Other notation

$\dot{\square}$, $\ddot{\square}$, $\ddot{\square}$ = first and second time derivatives, respectively

$\tilde{\square}$ = quantity interpolated as a t-function

$\underline{\square}$ = dimensional value of a normalized variable $\square$

I. Introduction

Over recent decades, the scientific community has become ever-more aware of dangers lurking in the depths of outer space. Due to the popularization of the concept of deadly space-born encounters, such as the close-approach event of asteroid Apophis in 2029 [1], the attention of governmental bodies is drawn to Near Earth Asteroids (NEAs), i.e., asteroids with an orbital perihelion within 1.3 AU from the barycenter of the Solar System [2], as their potential encounter with our planet poses a risk to the global population and economy. One of the NEAs subclasses, Potentially Hazardous Asteroids (PHAs), are defined as NEAs (1) of approximately or larger than 150 m in diameter and (2) characterized by a Minimum Orbit Intersection Distance (MOID), i.e., the minimum distance between the trajectories of Earth and the NEA, of less than or equal to 0.05 AU [3]. To prevent the undesirable event of a NEA impact, risk mitigation techniques are investigated and may be divided into deflection and disruption of PHAs. Deflection might be executed by means of (1) abrupt modifications to the NEA's trajectory, e.g., by means of a kinetic impactor or nuclear explosive deflection or (2) slow operation using a gravity tractor, laser ablation of asteroidal material, a rocket engine attached to the asteroid surface, or focused solar energy to exert radiation pressure [3, 4].

To date, only one impact mitigation technique has been demonstrated in a large-scale experiment of the Asteroid Impact and Deflection Assessment (AIDA) - a mission composed of the Double Asteroid Redirection Test (DART) impactor and the European Space Agency's Hera reconnaissance probe. AIDA's goal is to test the kinetic impactor technique as a deflection scenario on the smaller body of the binary asteroid (65803) Didymos, i.e., Dimorphos, and provide insight into the internal structure of the asteroids by studying the post-impact properties of the system [5–7]. Since both the binary system and its more massive body are named 'Didymos', we refer to them as 'the Didymos system' (or 'the Didymos binary system') and 'Didymos', respectively. The Didymos system was selected for this technology demonstration mission due to its binary nature - the mass of the lesser body of the system is sufficiently small to allow observation of the change in momentum from the impact [5]. DART has performed the impact into the smaller body of the Didymos binary system on September 26th, 2022 [8], during the binary asteroid's close approach to Earth. Hera will arrive at the system in January 2027 [9].

Planning of Hera's trajectory within the binary system requires knowledge of potential hazards and a structured approach to the mitigation thereof. Limited information available on the system introduces large uncertainties in the anticipated state of the system upon the arrival of the spacecraft. One of the potential hazards to the probe may be posed by regolith grains floating in the binary system. To comprehend the risk that the levitated dust poses to the spacecraft, the following phenomena must be considered: (1) trajectories of potential mass transfer between the bodies, (2) temporary capture of levitated regolith grains in periodic orbits or other types of bounded stable motion.

Assuming the presence of loose regolith on the surface of the primaries in the Didymos system - like for other similar small bodies in the Solar System - Cheng et al. [10], Zhang et al. [11], Yu et al. [12], Yu et al. [13] and Yu et al. [14] study the expansion of particles levitated from spinning-top asteroids. Cheng et al. [10] model the observations of ejecta plume as a result of DART's impact, whereas Zhang et al. [11] model interactions between the particles composing internal layers of Didymos. Works by Yu et al. [12–14] are of particular interest; the authors investigate the Roche lobe properties in the Didymos binary and determine the regions where levitation of non-microscopic particles (particularly of interest in the context of trajectory planning) might occur. The dynamical models used in the studies employ high-accuracy spherical-harmonic expansions of the gravitational field fitted to the radar-derived shapes of the asteroids under the assumption of uniform density distribution, inertial (Coriolis and centrifugal) accelerations, and contact forces. In [13], Yu et al. investigate the re-accretion by Dimorphos of the regolith particles originating from DART's impact into Dimorphos, i.e., the mechanism of the forced primary-to-secondary mass transfer. Yu et al. [14] derive shedding-off conditions for loose debris from the surface of Didymos and elaborate on the dynamical analysis indicating a strong size-sorting effect present in the system. The dynamical model introduced in the work accounts for the gravitational fields of both primaries, solar radiation pressure (SRP), tidal effects due to the gravity of the Sun, and contact forces present in the regolith layer. In [14], the authors trace back the dust particles in orbital motion and conclude that most of them originate from the equatorial bulge of Didymos. Similar conclusions are reached by Sánchez et al. [15] in the study of the top-spin asteroid model introduced by Scheeres [16]. Sánchez et al. [15] derived a scaling law determining the conditions necessary for an asteroid to retain regolith particles on its surface.

Temporary capture of levitated regolith particles in the Didymos system has not been studied to date. However, the existence of periodic orbits or regions of bounded motion (which we collectively refer to as 'bounded trajectories') has been investigated. Dynamical frameworks used in these studies are the circular-restricted three-body problem (CR3BP) and the shape-based three-body problem (SB3BP) with possible augmentations of third-body effects and solar radiation pressure. The SB3BP, also named the 'shape-based circular-restricted three-body problem', augments the CR3BP by substituting the point masses with finite-volume masses of arbitrary shapes [17]. Oliveira and Prado [18] perform a grid search for periodic orbits in the Didymos system within the SRP-augmented CR3BP framework. Capannolo et al. [19] identify several families of Direct Orbits (DO's) and orbits around Equilibrium Points (EP's) using the SB3BP representation of the binary. Jean et al. [20] conduct a search for SRP-compatible orbits in the SRP-augmented SB3BP, whereas Dell'Elce et al. [21] and Lasagni Manghi et al. [22] perform analogous analyses in the SB3BP augmented by introducing third-body effects as well as the SRP perturbation. Silva Neto et al. [23] use a high-fidelity model, incorporating the SRP effect and third-body accelerations of all the planets in the Solar System into the SB3BP framework. In conclusion, the dynamical neighborhood of the binary has been extensively studied; however, no comprehensive search for bounded trajectories and temporary capture of the levitated regolith particles therein have been conducted in a high-fidelity model of the Didymos system to date. We deem it a knowledge gap in light of the significant contributions of perturbative accelerations of SRP, nonspherical mass distribution of both bodies, and third-body effects, as shown by Yu et al. [24].

This work thus focuses on determining the conditions leading to temporary capture of naturally-levitated regolith particles within the system using a high-fidelity model. Since natural levitation of regolith particles is expected from Didymos [12, 14], only the primary body of the binary system is considered as the source of regolith shedding. The first investigated aspect is the regions of levitation, which can also serve as validation of the results by Yu et al. [12, 14], who used a detailed shape model of Didymos, accounted for the inertial effects due to the primary's rotation, and surface friction. As a second input to the analysis, we conduct a search of the state space for bounded trajectories by means of a grid search method. In the grid search exploration, we aim to identify regions of bounded motion, which we further investigate as potential initial conditions of periodic orbits. We conclude by performing an intersection of the two results, i.e., the set of initial conditions on the surface leading to levitation and the set of initial conditions leading to the temporary capture in bounded trajectories. As a result of the latter, we obtain a set of initial conditions originating on the surface of the asteroid that lead to temporary capture of dust particles. Since the characteristics of the superficial regolith in the Didymos system are derived from literature-based data under assumption of similarity to other asteroidal regolith layers, we perform the study for only one particle size, as a matter of demonstration of the adopted methodology. In particular, for comparison with the work by Wiegert [25], we perform the study for a diameter of the regolith boulders of 5 cm, which falls within the spectrum of dust properties on similar bodies, as in [26–28] but does not cover the lesser sizes. We anticipate that the results of this study will make a contribution to the knowledge of the Didymos system and provide valuable input to the planning of Hera's trajectory in the system by determining unsafe-to-fly regions.

II. Properties of the Didymos system

From the discovery in 1996 by Joe Montani at the Kitt Peak National Observatory, Didymos was considered a single asteroid until the observation of a lesser body, Dimorphos, in a mutual orbit with the main body in 2003 by Petr Prevc of the Ondřejov Observatory [29, 30]. The Didymos system has been studied by means of photometric lightcurve analysis [31] and planetary radars [32]. The large size of Didymos allowed for precisely describing its physical properties (see table 1), including a radar-derived shape model of the asteroid [33]. However, the physical features of Dimorphos determined by the aforementioned analyses bear larger uncertainties (see table 2) due to a small signal-to-noise ratio in the radar imaging [34]. Based on previous knowledge of other binary asteroids, Agrusa et al. [33] conclude that the Didymos system secondary body is in a 1:1 spin-orbit ratio, i.e., in tidal lock. Simulations conducted by the authors of [33] indicate that - depending on DART's impact scenario - Dimorphos might break out of its resonance or enter libration.

Table 3 lists the physical properties of the Didymos system - from its mass, size ratio, and characteristics of the binary system orbit to its orbital data in the the heliocentric ecliptic J2000 reference frame [29]. Table 1 presents a collection of Didymos' physical properties: its bulk density, shape, and rotation period. Note that the Dynamically Equivalent Equal Volume Ellipsoid (DEEVE) in table 1 is "an ellipsoid with uniform density with the same volume and moments of inertia as the shape model" [32] and will be used for dynamical modelling. Damme et al. [35] computed the $C_{2,0}$ and $C_{2,2}$ Stokes coefficients of the spherical harmonic expansion of the gravitational field from the radar-derived shape model of Didymos and assuming it to be a tri-axial ellipsoid (see fig. 1) of constant density. The principal axes of Dimorphos' tri-axial ellipsoid $a_d > b_d > c_d$ are defined through mutual ratios (see table 2). The semi-axes of

Table 1 Properties of Didymos

Physical quantity	Symbol	Value	Unit	Comments and references
Bulk density	ρ_D	2170 ± 350	kg m^{-3}	Based on D_D and m_b [6, 36, 37]
Extents along principal axes	D_{D,x_D} D_{D,y_D} D_{D,z_D}	832 ± 6% 838 ± 6% 786 ± 10%	m	[32]
DEEVE extents	D^*_{D,x_D} D^*_{D,y_D} D^*_{D,z_D}	797 ± 6% 783 ± 6% 761 ± 10%	m	[32]
$C_{2,0}$ coeff. unnormalized	$C_{2,0}$	−0.023	-	Assuming constant density and tri-axial ellipsoid shape [35]
$C_{2,2}$ coeff. unnormalized	$C_{2,2}$	−0.0013	-	Assuming constant density and tri-axial ellipsoid shape [35]
Sidereal spin period	$\underline{T}_D$	2.2600 ± 0.0001	h	[32]

Dimorphos' DEEVE were calculated from the assumption that D_d is the radius of a uniform-density ball, whose mass is equal to the mass of an ellipsoid characterized by the axes ratios a_d/b_d and b_d/c_d. The density of the regolith grain on the surface of Didymos is assumed to be equal to the bulk density of this asteroid, as given in table 1.

Table 2 Properties of Dimorphos

Physical quantity	Symbol	Value	Unit	Comments and references
Ellipsoidal axes ratios	a_d/b_d b_d/c_d	1.3 ± 0.2 1.2 ± 0.2	-	Based on other binary systems [6, 36, 38]
Equivalent diameter	D_d	164 ± 11%	m	From D_D and D_d/D_D [36]
DEEVE extents	D^*_{d,x_d} D^*_{d,y_d} D^*_{d,z_d}	106.75 82.11 68.43	m	Calculated assuming equal mass to a sphere of radius equal to D_d and uniform ellipsoidal density distribution

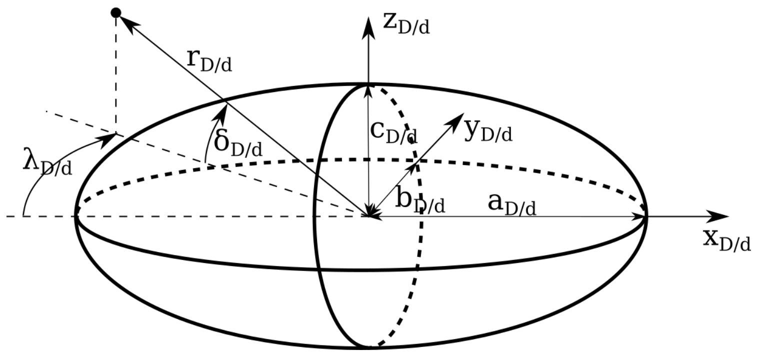

Fig. 1 Ellipsoid

Table 3 Properties of the Didymos system

Physical quantity	Symbol	Value	Unit	Comments and references
Size ratio	D_d/D_D	0.21 ± 0.01	-	[6, 38]
Total system mass	m_b	$(5.28 \pm 0.54) \times 10^{11}$	kg	[6]
Binary orbit				
Semi-major axis	A_b	1.19 ± 0.03	km	[32]
Orbital eccentricity	e_b	< 0.03	-	[6, 38]
Orbital pole	(Λ_b, B_b)	$(310, -84) \pm (0, 9)$	°	[6, 32]
Orbital period	$\underline{T}_b$	$11.920\,^{+0.004}_{-0.006}$	h	[6]
Orbital obliquity	ψ_b	171 ± 9	°	[6]
Heliocentric orbit				
Semi-major axis	A_h	1.644576707340323	au	1σ: 5.6956×10^{-9} [29]
Orbital eccentricity	e_h	0.3836383357953901	-	1σ: 9.7517×10^{-9} [29]
Orbital inclination	i_h	3.407819057354463	°	1σ: 3.0891×10^{-6} [29]
Orbital period	$\underline{T}_h$	770.3349979813357	d	1σ: 4.0018×10^{-6} [29]

III. Dynamical model

Damme et al. [35] presented a quantitative comparison of the magnitudes of various accelerations in the vicinity of the Didymos system. In view of the small mass of the system, the third-body (also referred to as 'tidal') effects due to the Sun's mass and the SRP perturbation have a large contribution to the total acceleration experienced by the particle. Therefore, the augmented bicircular problem (ABP) is used for the dynamics of levitated particles in this work. The ABP is the combination of the SB3BP and the SRP-augmented bicircular problem (BP). The dynamical model introduces ellipsoidal primaries - a rotating primary and a tidally locked secondary as in Ferrari et al. [17] - as well as gravitational third-body and SRP perturbations, as given by Heiligers and Scheeres [39].

The model is based on the following assumptions: (1) two of the bodies (here, the primaries) have significantly larger mass than the third one (from here on referred to as a 'particle'), (2) gravitation of the particle does not cause observable effects in the motion of the primaries, and (3) the orbits of the primaries are circular. Applying such simplifications in our work is justified by the small individual masses of the regolith particles compared to the scale of the binary and the observed small eccentricity of the binary orbit (see table 3). The reference frame is barycentric, i.e., the origin coincides with the center of mass of the primaries. We introduce the mass parameter [40, 41] $\mu = m_d/(m_D + m_d)$, where m_D and m_d are the masses of the primary and secondary, i.e., the more and the less massive bodies, respectively. Normalization of relevant physical quantities is performed using the characteristic dimensions presented in table 4 (where G stands for the universal gravitational constant), as in $\zeta = (\zeta^*)^{-1}\underline{\zeta}$, where $\underline{\zeta}$ and ζ^* are a dimensional arbitrary quantity and its characteristic value, respectively. Normalized masses of the primaries are given by [40, 41] $\mu_D = 1 - \mu$ and $\mu_d = \mu$, where $\mu_D \geq \mu_d$. Adopting a synodic reference frame $\mathcal{F}(x, y, z)$ rotating uniformly at a normalized angular rate $\Omega = 1$, where the origin coincides with the center of mass of the binary, the x-axis pierces the centers of mass of both bodies of the binary system, the z-axis is parallel to the system's angular momentum vector, and the y-axis completes the right-hand reference frame, allows for fixing the primary at $\mathbf{r}_D = [-\mu, 0, 0]^T$ and the secondary at $\mathbf{r}_d = [1 - \mu, 0, 0]^T$ (see fig. 2).

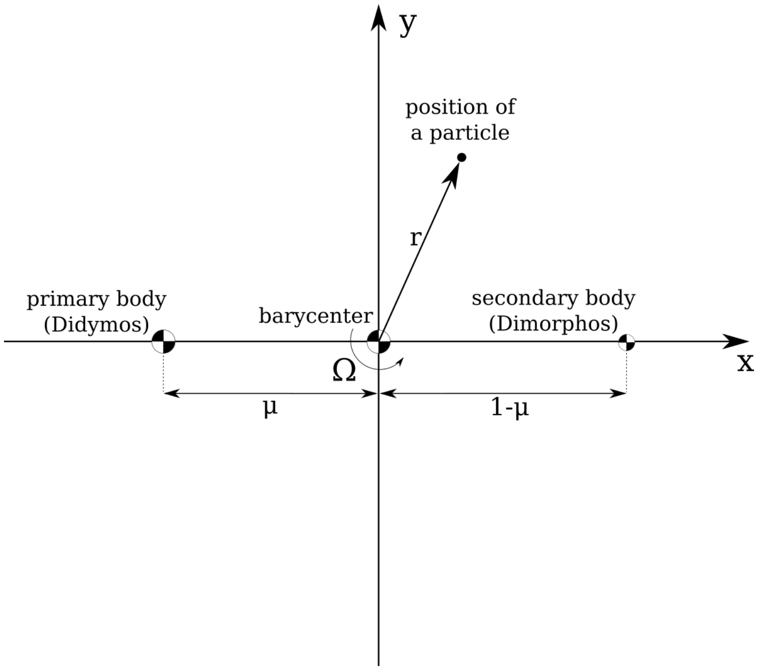

Fig. 2 Inertial and synodic reference frames

Table 4 Normalization of physical quantities [41]

	Mass [kg]	Distance [m]	Time [s]	Speed [m s^{-1}]	Acceleration [m s^{-2}]
Characteristic value	$M^* = m_b$	$R^* = A_b$	$t^* = 2\pi \left(\frac{(R^*)^3}{(m_b\, G)} \right)^{1/2}$	$V^* = \frac{R^*}{t^*}$	$\ddot{r}^* = \frac{R^*}{(t^*)^2}$

A. Equations of motion

The equations of motion are defined as

$$\ddot{\mathbf{r}} = -2\,\mathbf{\Omega} \times \dot{\mathbf{r}} + \nabla U = -2\,\mathbf{\Omega} \times \dot{\mathbf{r}} + \nabla U_{SB3BP} + \nabla U_{3rd} + \nabla U_{SRP} \ , \tag{1}$$

where

$$\nabla = \left[\frac{\partial}{\partial x}, \frac{\partial}{\partial y}, \frac{\partial}{\partial z}\right]^T \tag{2}$$

and U, U_{SB3BP}, U_{3rd}, and U_{SRP} are the effective potentials of the ABP, of the shape-based three-body problem, of the third-body perturbation, and of the solar-radiation pressure perturbation, respectively; the effective potentials are discussed in detail in the following section.

B. Effective potential

The effective potential of the augmented bicircular problem (ABP) is composed of three terms: the effective potential of the shape-based three-body problem (SB3BP) U_{SB3BP}, the third-body augmentation term U_{3rd}, and the SRP augmentation term U_{SRP},

$$U = U_{SB3BP} + U_{3rd} + U_{SRP} \ . \tag{3}$$

The effective potential of the SB3BP is given by

$$U_{SB3BP} = \frac{1}{2}\left(x^2 + y^2\right) + U_{M_D} + U_{M_d} \ , \tag{4}$$

where U_{M_D} and U_{M_d} are the gravitational potentials of Didymos' and Dimorphos' ellipsoids, respectively.

1. Gravitational potential

The Didymos-fixed Cartesian reference frame $\mathcal{F}_D(x_D, y_D, z_D)$ is defined by the origin coinciding with the center of mass of the body, the x_D-axis points along the longest semi-axis of the ellipsoid a_D, the z_D-axis points along the shortest semi-axis c_D of the ellipsoid and in the direction of the z-axis, whereas the y_D-axis completed the right-handed reference frame (see fig. 1). The Dimorphos-fixed reference frame is defined in an analogous manner using the subscripts 'd' - all the body-fixed definitions given below also follow the same analogy between Didymos ('D') and Dimorphos ('d'). All position vector transformations between the synodic and body-fixed reference frames are given in section VII.A. The gravitational potentials of the primaries are given in the body-fixed spherical reference frames - for Didymos it reads $\mathcal{F}_{s_D}(r_D, \lambda_D, \delta_D)$, where r_D is the distance to the center of mass of Didymos, λ_D is the azimuth angle, and δ_D is the elevation angle (see fig. 1) given by

$$\lambda_D = \arctan\left(\frac{y_D}{x_D}\right) \tag{5}$$

$$\delta_D = \arcsin\left(\frac{z_D}{r_D}\right) \ , \tag{6}$$

The gravitational potential of Didymos is given by a second-degree, second-order expansion of the spherical harmonics gravity model [42]

$$U_{M_D}(r_D,\delta_D,\lambda_D)=\frac{\mu_D}{r_D}\left[1+\left(\frac{r_{ref,D}}{r_D}\right)^2\left\{C_{2,0}\left(1-\frac{3}{2}\cos^2(\delta_D)\right)+3C_{2,2}\cos^2(\delta_D)\cos(2\lambda_D)\right\}\right]\ , \tag{7}$$

where $r_{ref,D}$ is the reference radius of Didymos' expansion - in this case $r_{ref,D}=a_D$ due to the coincidence of the expansion origin with the center of mass lying at the center of the ellipsoid.

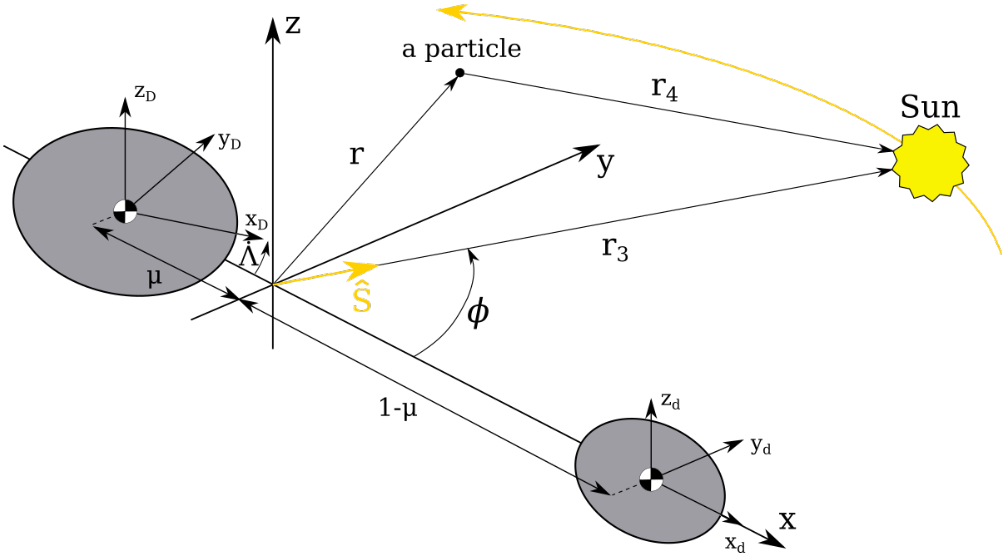

Fig. 3 Augmented bicircular problem

2. Perturbative potential of the third-body effect

The relative motion of the Sun in the synodic frame is approximated by a circular orbit at the normalized distance $r_3=\underline{r}_3\ L^{-1}$ (see fig. 3 and table 4) and revolves around the frame's origin at the rate

$$\Omega_s=\frac{f_b+f_h}{f_b}=\left(T_b^{-1}+T_h^{-1}\right)T_b\ , \tag{8}$$

where T_b and T_h are given in table 3 f_b and f_h are the mean motion of the binary and heliocentric orbits, respectively. Therefore, the third-body and SRP accelerations act parallel to the Sun-pointing vector $\hat{\mathbf{S}}$, i.e., a unit vector originating at the origin of $\mathcal{F}_s$ and pointing towards the current position of the Sun, which in $\mathcal{F}_s$ takes the form

$$\hat{\mathbf{S}}=\begin{bmatrix}\cos(\phi)\\ \sin(\phi)\\ 0\end{bmatrix}=\begin{bmatrix}\cos(\Omega_s t+\phi_0)\\ \sin(\Omega_s t+\phi_0)\\ 0\end{bmatrix} \tag{9}$$

where $\phi_0 = \phi(t = 0)$, i.e., the angular position of the Sun ϕ in $\mathcal{F}$ at $t = 0$. As shown by the coordinates of the orbital pole of the binary (Λ_b, B_b) in table 3, the angular momentum vector of the Didymos binary is opposite to the angular momentum vector of the heliocentric orbit. Therefore, the Sun revolves around the binary in a counter-clockwise fashion in the synodic frame $\mathcal{F}$.

The third-body perturbation produces the difference in the gravitational accelerations experienced by the center of mass of the Didymos binary and the particle due to the difference in distance to the Sun [39, 41]

$$U_{3rd} = \frac{1}{\|\mathbf{r}_4\|} - \frac{\mathbf{r} \cdot \mathbf{r}_3}{r_3^3}\mu_3 \ , \tag{10}$$

where μ_3 is the mass parameter of the perturbing fourth body and the vectors $\mathbf{r}$, $\mathbf{r}_3$, and $\mathbf{r}_4$ are the position vector of the particle in $\mathcal{F}$, the position vector of the Sun in $\mathcal{F}$, and the particle-Sun vector in $\mathcal{F}$, respectively,

$$\mu_3 = \frac{m_3}{m_D + m_d} \tag{11}$$

$$\mathbf{r}_3 = r_3 \hat{\mathbf{S}} \tag{12}$$

$$\mathbf{r}_4 = \mathbf{r}_3 - \mathbf{r} \tag{13}$$

where m_3 is the Sun's mass (see fig. 3).

3. Perturbative potential of the solar radiation pressure

The solar radiation pressure (SRP) perturbation is caused by the exchange of momentum between the particle's surface and photons. Effects caused by radiation pressure of sources other than direct illumination by the Sun are neglected. Due to the use of the shape-based approach, eclipses occur in the model. Therefore, we introduce an eclipse model which serves to calculate the fraction of the SRP acceleration exerted on the particle. The eclipse model follows the cylindrical model as defined by Li et al. [43], where penumbra conditions are not considered (see fig. 4). We define the potential of the SRP perturbation as

$$U_{SRP} = -\ddot{r}_{SRP} (\hat{\mathbf{S}} \cdot \mathbf{r}) \ . \tag{14}$$

The total experienced SRP acceleration is given by

$$\ddot{r}_{SRP} = \ddot{r}_{SRP,BP} \ \beta_D \beta_d \ , \tag{15}$$

where $\ddot{r}_{SRP,BP}$ is the magnitude of unshaded SRP acceleration, β_D and β_d are the effective coefficients due to the shadow cast by the Didymos and Dimorphos, respectively. The shading effective coefficient β is discussed in the following paragraph. The dimensional value of the unshaded SRP perturbation $\underline{\ddot{r}}_{SRP,BP}$ is assumed to be constant over the time scale of the dynamical problem, but varies depending on the exact location of the binary system in its heliocentric orbit, therefore the importance of the eccentricity of the heliocentric orbit ($e_h \approx 0.38$, see table 3) cannot be neglected. The normalized magnitude of the SRP acceleration reads [44]

$$\ddot{r}_{SRP} = \left((t^*)^2 \, (R^*)^{-1}\right) \underline{\ddot{r}}_{SRP,BP} = \left((t^*)^2 \, (R^*)^{-1}\right) \frac{W_E C_p \sigma}{c_l} \left(\frac{R_E}{R_b}\right)^2 \tag{16}$$

where $\left((t^*)^2 \, (R^*)^{-1}\right)$ is the normalizing factor and W_E, C_p, σ, c_l, R_E, R_b are the solar constant, scaling coefficient, mass-to-area ratio of the particle, speed of light, reference Sun-Earth distance, and Sun-Didymos system distance, respectively. The particles are assumed to be of spherical shape and the scaling coefficient is taken as $C_p = 1.5$, whereas for the mass-to-area ratio we use [45]

$$\sigma = \frac{2}{3}\rho\pi r_p \ , \tag{17}$$

where ρ is the density of the regolith particle ($\rho = \rho_D$, see table 1) and r_p is the particle's radius.

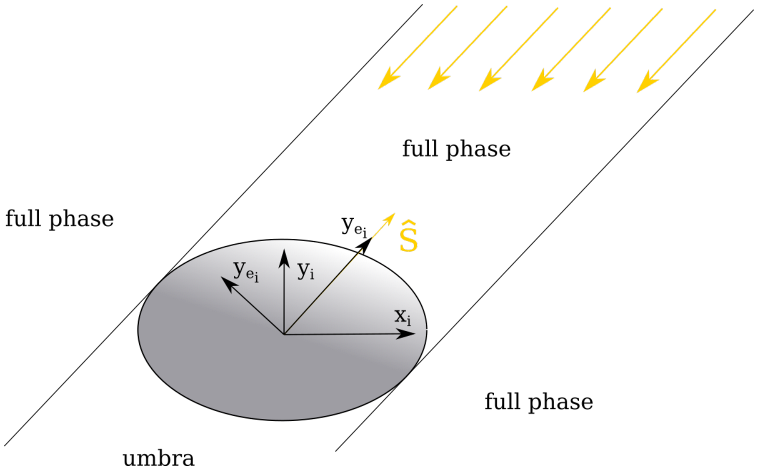

Fig. 4 Cylindrical eclipse model

The effective coefficient for Didymos is found from

$$\beta_D = 1 - \tilde{\sigma}\left(5, \frac{r_{ell}(\lambda_D, \delta_D) - r_{proj}}{r_p}\right) \texttt{int}\left((\mathbf{r} - \mathbf{r}_D) \cdot \hat{\mathbf{S}} < 0\right) \tag{18}$$

where $r_{ell}(\lambda_D, \delta_D)$, r_{proj}, r_p, and $\mathbf{r}_D$ are the radius of the ellipsoid in the direction specified by a pair of spherical coordinates (λ_D, δ_D), the radius projected on the x_D-y_D plane, the radius of the particle, and the position vector in $\mathcal{F}_D$, respectively (for details refer to section VII.B). The term $\texttt{int}\left((\mathbf{r} - \mathbf{r}_D) \cdot \hat{\mathbf{S}} < 0\right)$ is a conditional switch, which ensures that the subtrahend of the equation is null if the particle is placed between the luminous body and the (potentially) obscuring body. The modified sigmoid function $\tilde{\sigma}(s, \varphi)$ is defined as [46, 47]

$$\tilde{\sigma}(s, \varphi) = \frac{1}{1 - e^{-s\varphi}} \tag{19}$$

where s is the sigmoid contrast factor and φ is an arbitrary real number. The role of the contrast factor is to allow tailoring the topology of the sigmoid function to the characteristics of the problem. To obtain $\beta_D \approx 1$ for unobscured particles and $\beta_D \approx 0$ for particles in eclipse, we select $s = 5$, and as a result the topology of the modified sigmoid takes the form presented in fig. 5. The larger and smaller dips visible in fig. 5 around $x = 0$ and $x = 1100$ are shades of Didymos and Dimorphos, respectively (the graphical representation of the verification case is given in fig. 6). The use of a smooth function emulates partial shading of the particles when in the transition between full phase and umbra conditions and avoids abrupt changes offered by the Heaviside function [47], often used in the cylindrical model.

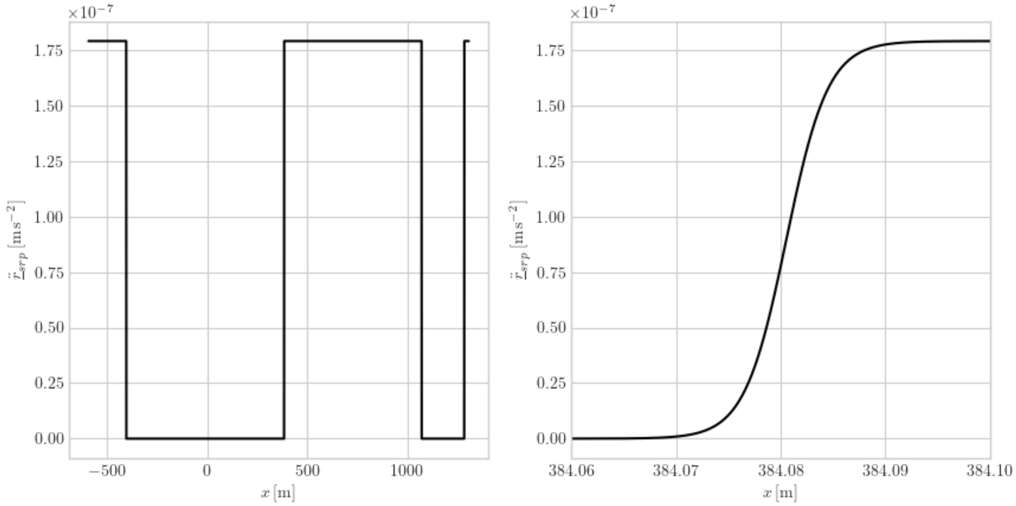

Fig. 5 Dimensional values of the SRP acceleration acting on a test particle of radius 1 cm for $\mathbf{r} = [x, -1, 0]^T$, $\phi_0 = \pi/2$, $\Lambda_0 = 0$

IV. Regions of levitation

We determine the regions of levitation by discretizing the ellipsoidal surface and projecting the acceleration vector experienced by a particle on the unit vector normal to the asteroid's surface. This enables us to calculate the slope experienced by the particle. The use of the spherical harmonic expansion of the gravity field is, however, limited to the outside of the Brillouin sphere (BS) [48] - in this study, the BS radius is equal to the largest semi-axis of the DEEVE for both primaries (given in table 1 and table 2). Therefore, to perform a valid analysis of the dynamics at the surfaces of the ellipsoids, we use a mass-concentration (abbreviated as 'mascon') gravity model (MC) within the BS, which asserts convergence of the gravity field model and has successfully been used to model asteroidal gravity fields [49]. Next, we

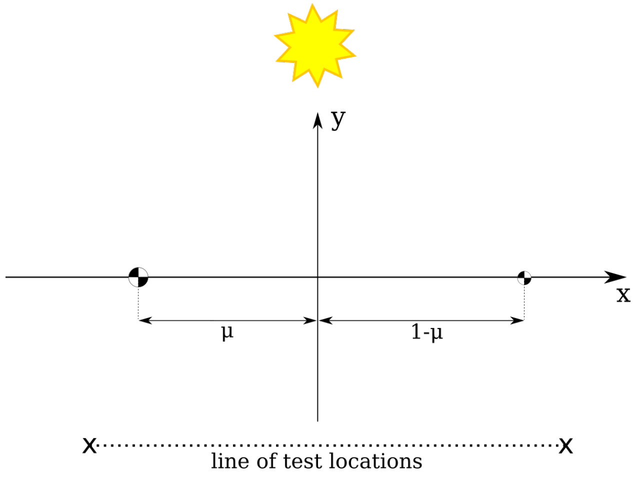

Fig. 6 Depiction of the verification case analyzed in fig. 5

assess the discontinuity at the BS due to the transition between the newly introduced dynamical model and the ABP. We conclude the analysis by propagating the motion of levitated particles from the surface of an asteroid to the BS or until redeposition on the surface. Further, we study the fates of the particles that cross the BS upon levitation.

A. Proximity dynamical model

We define the dynamical model (further referred to as the 'proximity dynamical model' or 'PDM') on the surface of the ellipsoidal model of Didymos using a modified effective potential

$$U_{PDM} = U_{MCD} + U_{3rd} + U_{SRP} \ , \tag{20}$$

where the term U_{MCD} describes the effective potential for the particles in the proximity to Didymos's surface, i.e.,

$$U_{MCD} = \frac{1}{2}\left(x^2 + y^2\right) + \sum_{j=1}^{N_{sph}} \left(\frac{\mu_j}{\|\mathbf{r} - \mathbf{r}_j\|}\right) + \frac{1}{2}\dot{\Lambda}^2 (x_D^2 + y_D^2) + U_{M_d} \ . \tag{21}$$

The terms of eq. (21) are the centrifugal potential of the synodic frame $\frac{1}{2}\left(x^2 + y^2\right)$, the MC potential for Didymos $\sum_{j=1}^{N_{sph}} \left(\mu_j / \|\mathbf{r} - \mathbf{r}_j\|\right)$, the centrifugal potential on the surface of Didymos $\frac{1}{2}\dot{\Lambda}^2 (x_D^2 + y_D^2)$, and the SH gravity potential of Dimorphos U_{M_d}. N_{sph} is the number of mass concentrations in the model of Didymos and μ_j is the gravitational parameter of the j-th mass concentration, following the constraint $\mu_D = \sum_{j=1}^{N_{sph}} \mu_j$. We investigate only the levitation from rest; therefore, motion on the surface and, as a consequence, the Coriolis acceleration due to the rotation of the body-fixed frames are neglected.

B. Mechanism of levitation from rest

Levitation of a particle located at (δ_D, λ_D) on the surface of an asteroid is determined by calculating the angle between the acceleration vector $\ddot{\mathbf{r}}_D = \nabla U_{PDM}$ and the inward normal vector $\hat{\mathbf{n}}$, following the approach presented in [14]. The inward normal vector is defined as

$$\hat{\mathbf{n}}(\delta_D(x_D, y_D, z_D), \lambda_D(x_D, y_D, z_D)) = -\frac{\nabla F}{\|\nabla F\|}\,, \tag{22}$$

where F is a function describing the ellipsoidal model of Didymos in the Didymos-fixed reference frame's Cartesian coordinate system and F_S is an equivalent function using spherical coordinate system in the same reference frame

$$F(x_D, y_D, z_D) = F_S\left(\delta_D(x_D, y_D, z_D), \lambda_D(x_D, y_D, z_D)\right) = \frac{x_D^2}{a_D^2} + \frac{y_D^2}{b_D^2} + \frac{z_D^2}{c_D^2} - 1 = 0\,, \tag{23}$$

using a_D, b_D, and c_D, which are the semiaxes of an ellipsoid, whose center of mass coincides with the frame origin and the semiaxes are aligned with the axes of the coordinate frame. The experienced slope of the particle is defined as $\alpha(\delta_D, \lambda_D) = \arccos(\nabla U_{PDM} \cdot \hat{\mathbf{n}}(\delta_D, \lambda_D))$. If $\alpha(\delta_D, \lambda_D) > 90°$, the particle at (δ_D, λ_D) experiences levitation.

C. Computational model

Didymos is represented by $N_D \approx 12.2 \times 10^6$ uniformly distributed mass concentrations of equal dimensionless elementary gravitational parameters $\mu_j = 8.1073 \times 10^{-8}$. The study of levitation conditions is conducted for all possible combinations of equally spaced four initial azimuthal positions of the Sun ϕ_0 and four initial angular positions of Didymos Λ_0 in the synodic frame of the ABP, i.e., $\phi_0, \Lambda_0 \in \{0,\ \pi/2,\ \pi,\ 3\pi/2\}$. A specific combination of the initial conditions of the system is named a 'case' (for the glossary of all studied cases, see table 5). The discretizations yield relative errors of the PDM acceleration (excluding the centrifugal term arising from the rotation of Didymos) with respect to the ABP acceleration on the BS smaller than 1%. The relative error on the BS is defined as $\epsilon_{BSi} = \|\nabla U - \nabla U_{PDM}\|\,\|\nabla U\|^{-1}$ and an example of the resulting error map is presented in fig. 7; we observe the largest relative error in the polar regions, which are the least distanced from the center of mass, and around the most-distanced areas, i.e., surrounding the points on the ellipsoidal surface of Didymos that are pierced by the largest semiaxes a_D.

Table 5 Glossary of cases

	$\phi_0 = 0$	$\phi_0 = \pi/2$	$\phi_0 = \pi$	$\phi_0 = 3\pi/2$
$\Lambda_0 = 0$	case 1	case 5	case 9	case 13
$\Lambda_0 = \pi/2$	case 2	case 6	case 10	case 14
$\Lambda_0 = \pi$	case 3	case 7	case 11	case 15
$\Lambda_0 = 3\pi/2$	case 4	case 8	case 12	case 16

As found by Yu et al. [14], dust particles located in the equatorial regions of Didymos likely experience levitation.

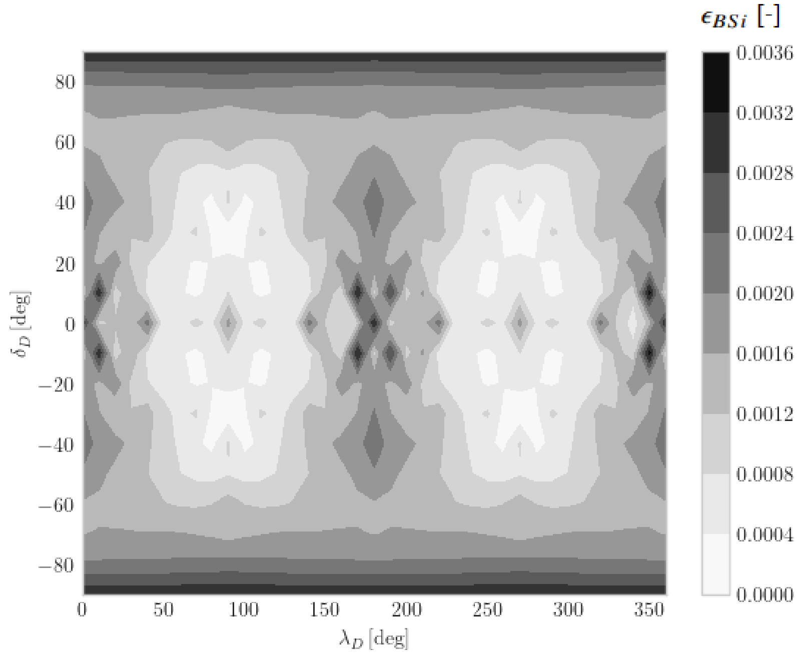

Fig. 7 Relative error of MC acceleration with respect to the ABP acceleration on the Brillouin sphere in equirectangular projection on the example of Didymos

Therefore, we examine only the primary body using a grid size of 1° in either latitude and longitude at latitudes of $\delta_i \in \langle -20°; 20° \rangle$ and 5° for latitudes of $\delta_i \in \langle -90°; -20° \rangle \cup \langle 20°; 90° \rangle$. The initial conditions on the surface that lead to levitation from rest are subjected to numerical propagation of the PDM equations of motion, which is then terminated upon crossing the BS or redeposition on the surface.

D. Numerical integration and termination conditions

All analyses of the dust particles' motion are conducted by means of numerical propagation of either the PDM or ABP equations of motion in the respective system. We use the Dormand-Prince integration scheme implemented in `SciPy` [50, 51] with the relative and absolute tolerances set to 10^{-13}. Alternative termination conditions of the propagation included crossing of the BS of Didymos, crossing of the BS of Dimorphos, and crossing of the Hill sphere of the binary system. All numerical propagations of the dust particle motion in this work follow the termination settings outlined in this section.

E. Results

In this section, results of the levitation analysis are presented. On the grid of 24840 nodes on the ellipsoid's surface, the number of nodes at which particles experience levitation is 7592 ± 4, depending between the initial conditions of the system. In addition, initial state vectors at the points of levitation (defined in the spherical body-fixed frame) differ negligibly between different starting conditions of the system, i.e., cases. Analogously, negligible differences were

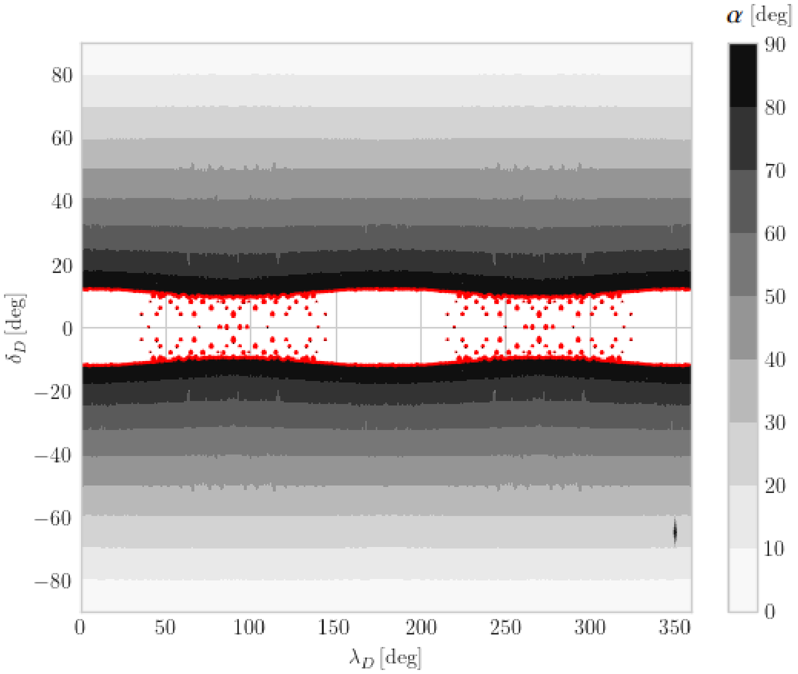

Fig. 8 Experienced slope by particles resting on the surface of Didymos in equirectangular projection (example plot for $t = 0$, $\phi_0 = \pi$, $\Lambda_0 = 3\pi/2$); levitation regions are marked with white in red contour

found for the results at the BS. This indicates that the centrifugal effect due to the rotation of Didymos is the primary factor determining levitation and all other effects may be treated as perturbations in the context of levitation. Taking into account significant similarities between the 16 cases, the results of the analysis are presented only for one of them, i.e., $\phi_0 = \pi$, $\Lambda_0 = 3\pi/2$.

1. Levitation from the surface of Didymos

Levitation from the primary takes place on a patterned region (see fig. 8). This is due to its regular shape in the dynamical model used in this paper, that the shape of the levitation region is closely related to the ellipsoidal shape model of Didymos. The red contour marks the boundaries of the levitation region. The bubble-shaped residual features of the red contour concentrated around certain longitudes are caused by smaller distance from the center of mass in these areas, since the y_D-axis-radius of the ellipsoid is smaller than any other on the equator plane, i.e., $a_D > b_D$. Therefore, the small red dots in fig. 8 constitute merely a visualization of an interpolation error and are neglected in the analysis.

2. Conditions at the Brillouin sphere

The propagation of initial state vectors at the points of levitation rendered 16 sets of position and velocity coordinates at the Brillouin sphere, one set for each case. None of the propagated trajectories resulted in redeposition on the surface of Didymos. Figure 9 presents a map of particles in spherical coordinates in the Didymos-fixed frame, where the

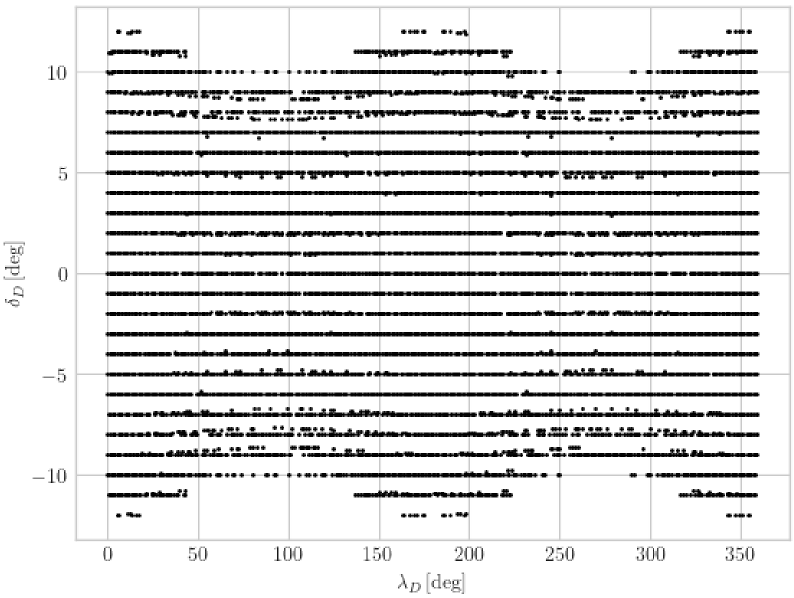

Fig. 9 Location of propagated trajectories after levitation at the BS of Didymos in equirectangular projection (example plot for $t = t_{BS}$**,** $\phi_0 = \pi$**,** $\Lambda_0 = 3\pi/2$**)**

levitated particles were found to cross the BS. A comparison between fig. 8 and fig. 9 demonstrates that levitated particles insignificantly change their spherical coordinates in the Didymos-fixed frame (disregarding the radius r_D for obvious reasons) before reaching the BS. This observation may be explained by the short distance between the surface and the BS in the regions of levitation and large initial velocities at levitation, i.e., typically $v \approx 0.05\ \mathrm{m\,s^{-1}}$. As indicated in fig. 10, the longitudinal distribution of levitated particles at the BS is approximately constant, with minor increments in vicinity of the largest semi-axis of the ellipsoid, i.e., at $\lambda \in \{0, \pi\}$. In addition, the tangential velocity component (defined in the spherical body-fixed frame) dominates over the radial component at all longitudes (see fig. 11, which presents the interpolated magnitudes of normal and tangential components of the particles' velocity vector at the instant of levitation).

The result of this analysis is 16 sets of approximately 7600 state vectors at the BS of Didymos. The results display significant consistency along the equator and negligible difference in distribution or direction of the velocity vector at the BS between the cases of the system's initial conditions.

3. Fates of levitated particles

To determine the fates of the levitated particles that cross the BS of Didymos, we propagate in ABP the conditions at the BS for the duration of $3T$. The fates of the levitated particles (see fig. 12, summarized in table 6) indicate small deviation of the numbers of survived particles n_s, particles collided with Didymos n_D, and particles collided with Dimorphos n_d. A strong sorting effect is seen in fig. 12, where a clear demarcation in regions is observed; particles levitated from a given region of the primary's surface meet a similar fate as the particles in its neighborhood.

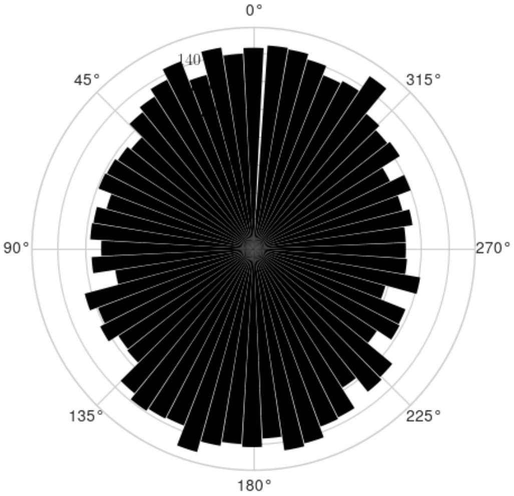

Fig. 10 Longitudinal histogram distribution of the location of piercing the BS of Didymos after levitation (example plot for $t = t_{BS}$, $\phi_0 = \pi$, $\Lambda_0 = 3\pi/2$)

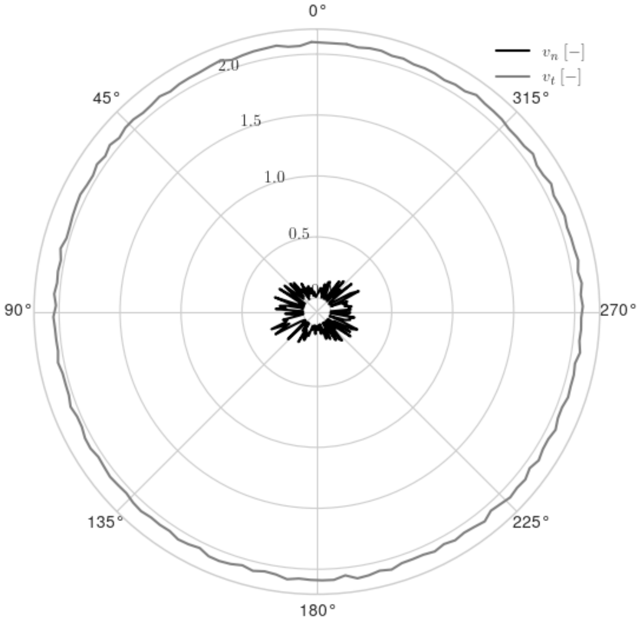

Fig. 11 Longitudinal magnitudes of the normal (v_n) and tangential (v_t) velocities at the BS of Didymos after levitation (example plot for $t = t_{BS}$, $\phi_0 = \pi$, $\Lambda_0 = 3\pi/2$)

Approximately 60% levitated particles are subject to reaccretion in the equatorial regions of Didymos. About 30% of levitated particles survive for the propagation time of 15 days, which suggests an existence of a regolith dust cloud around the binary. Approximately 7% of levitated particles are subject to mass transfer to Dimorphos; however, only half of them are deposited on the Didymos-facing hemisphere of Dimorphos. We observe a strong dependence between the orientation of the primary Λ and the fraction of levitated particles that escape the binary system within the 15 days of propagation; for $\Lambda_0 \in \{\pi/2; 3\pi/2\}$, the fraction of escaping particles amounts about 1.5% of all levitated grains, whereas this figure is approximately 2-3 times smaller in other studied cases (i.e., $\Lambda_0 \in \{0; \pi\}$).

We observe strong sorting effect in the fates of levitating particles when the largest semi-axis of Didymos is parallel to the y-axis (even-numbered cases of fig. 12). To better understand the nature of the sorting phenomenon on the example of case 2, we study the fates of particles levitated from around longitudes of 180-200 degrees by tracing the trajectories after levitation for particles on a refined grid. As shown in fig. 13, which studies the fates of particles levitated on a refined grid on the surface of Didymos ($\lambda \in \{175°, 175.1°, \dots, 214.9°, 215°\}$, $\delta = 0°$), and in fig. 14, which presents a close-up view of the trajectories given in fig. 13 that pass in the vicinity of Dimorphos's BS, a 'gravitational slingshot' phenomenon is observed. We deem that the gravitational slingshot is a specific example of a gravity assist that redirects a stream of levitated particles on trajectories escaping from the binary system upon a close pass to the surface of Dimorphos. As seen in table 6, the occurrence of the sorting effect (resulting from the gravitational slingshot escape) is correlated to the 2- to 3-fold increase in the percentage of the levitated particles escaping the binary. The levitated regolith particles from the refined-grid region that are re-deposited on Didymos are found to collide with the primary at all longitudes along the equator (see fig. 15). This observation, in the context of the numbers given in column n_D of table 6, strongly suggests a complex mechanism of approximately uniform (see fig. 19) regolith relocation in the equatorial regions, which effectively slows down the depletion of the regolith material of Didymos.

A similar observation can be made with regards to the dust particles transferred to Dimorphos; however, in this case the majority of transfer trajectories leads to deposition in the Didymos-facing hemisphere of Dimorphos, i.e., in the equatorial region between longitudes of 90° and 270° (see fig. 16). A similar flow of particles leading to mass transfer between the asteroids is observed in all studied cases, which implies a high probability of the occurrence of continuous, quasi-steady flow of dust, as observed in binary-star systems [52]. The topology of the trajectories presented in fig. 16 also indicate a mechanism of deposition of the regolith material levitated from Didymos on the non-Didymos-facing regions of Dimorphos. The percentages of the transferred particles per case that deposit on the outward-facing half of Dimorphos given in the n_d^* column of table 6 suggest that approximately 50-60% of the Didymos-Dimorphos transferred particles deposit on the outward-facing facet of Dimorphos.

One trajectory of each fate of levitated particles is plotted in fig. 17 to present examples of the trajectory topologies. As observed in fig. 17 in the demonstrated 'survived' case, some levitated particles follow intricate trajectories, as further demonstrated in fig. 18.

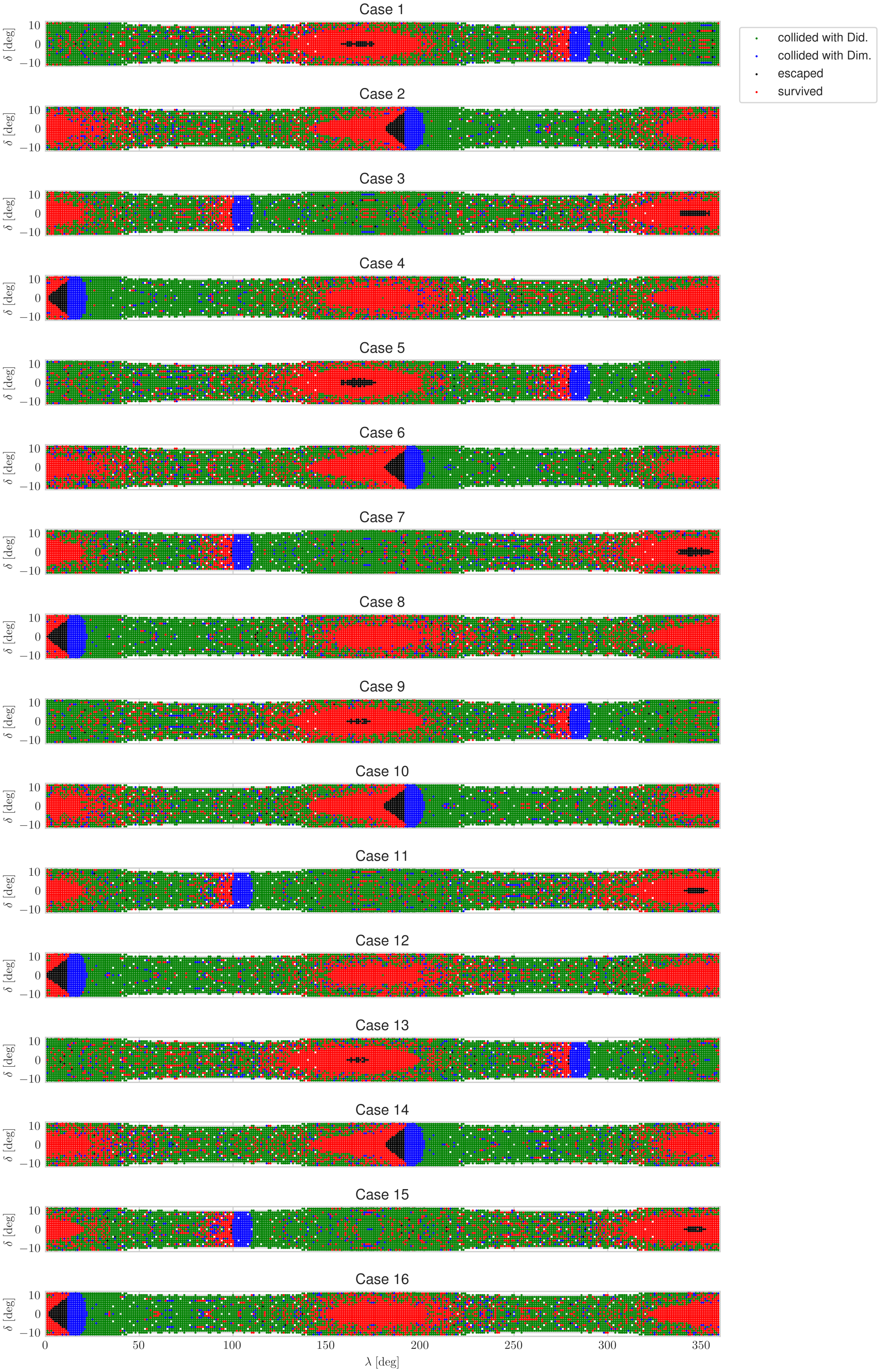

Fig. 12 **Fates of the levitated particles after a propagation for $3T$ after crossing the BS of Didymos**

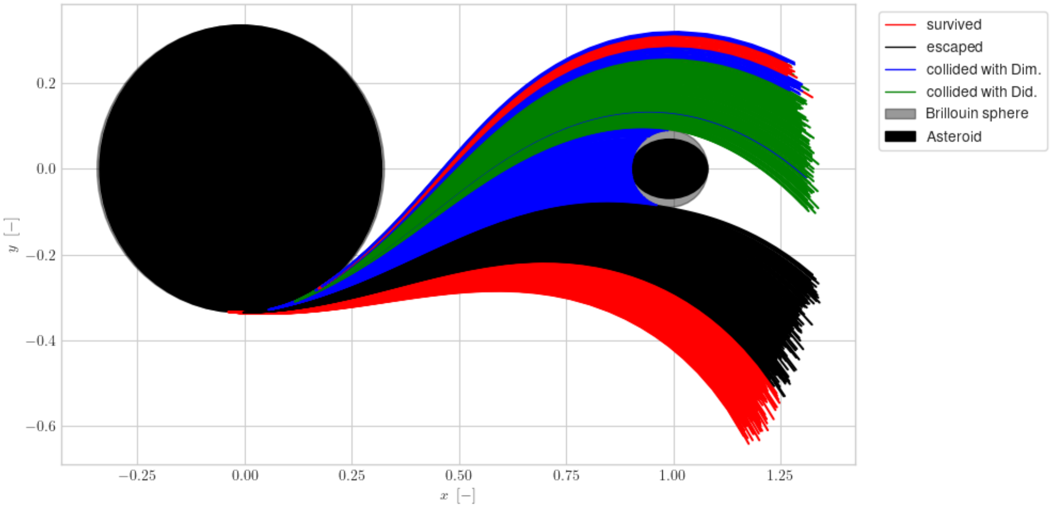

Fig. 13 Trajectories of the levitated particles on the refined sub-grid in the region of the strong sorting occurrence

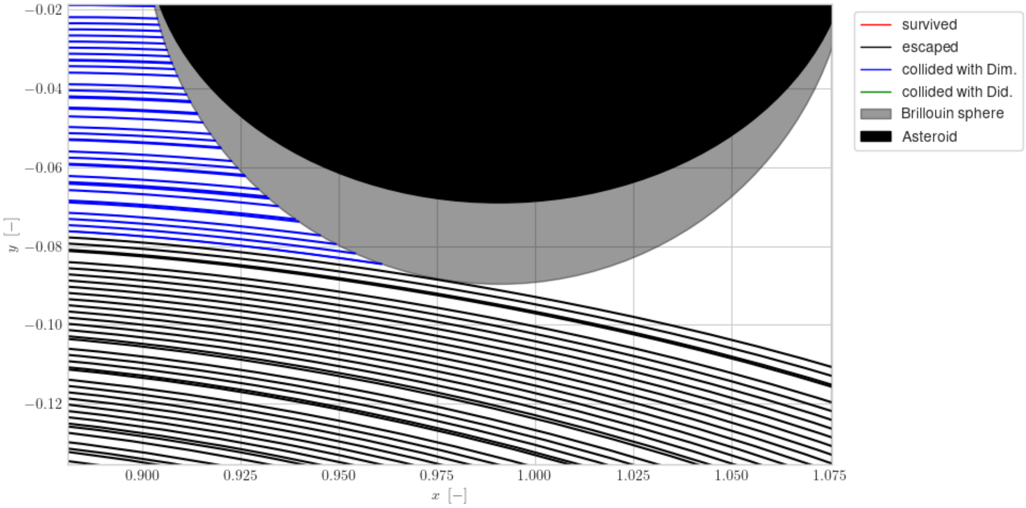

Fig. 14 Trajectories closely missing Dimorphos leading to escape from the binary

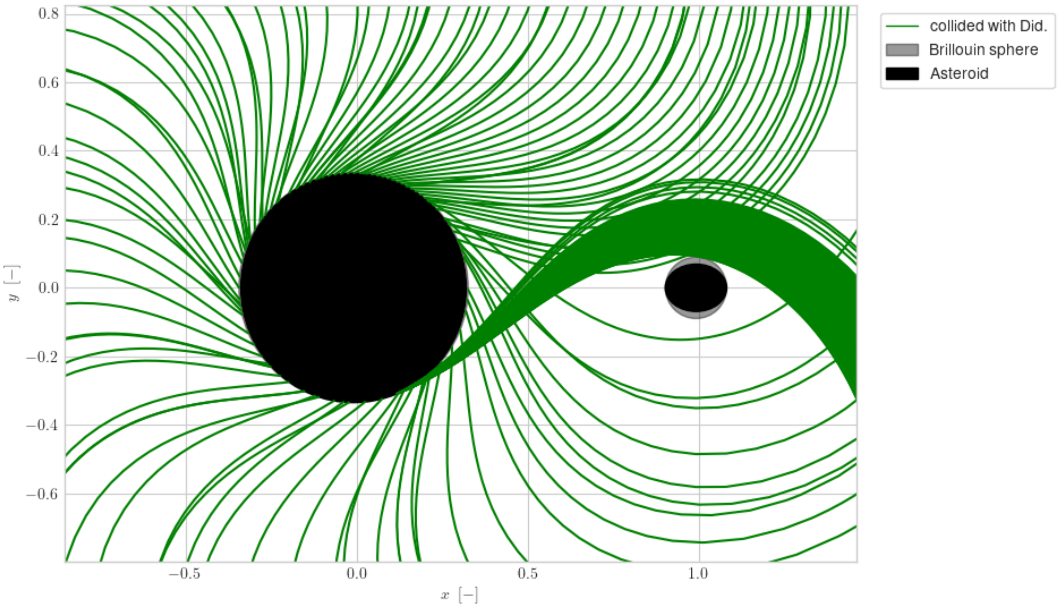

Fig. 15 **Trajectories leading to dust reaccretion on the surface of Didymos (in the refined grid analysis)**

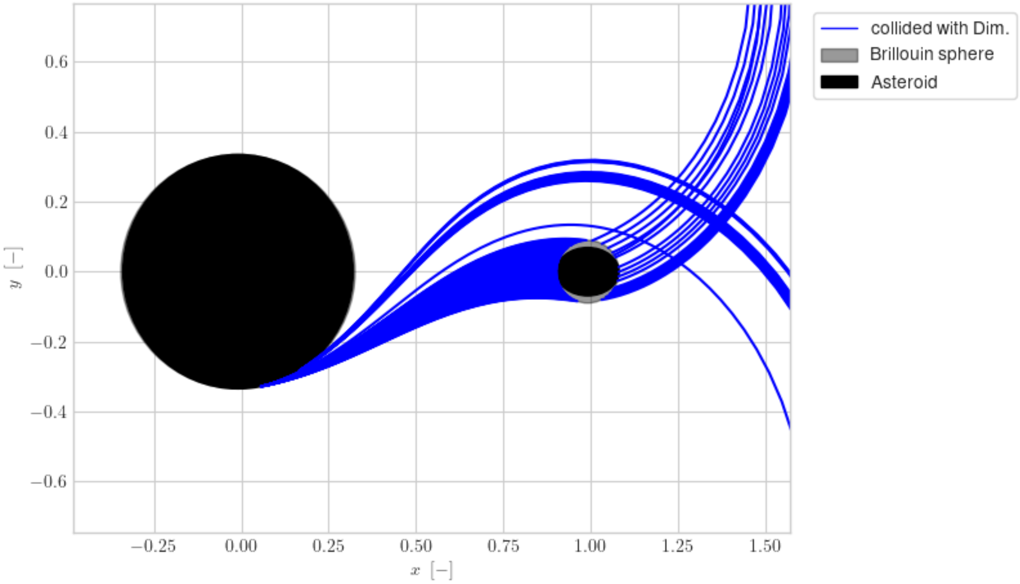

Fig. 16 **Trajectories leading to dust re-deposition on the surface of Dimorphos (in the refined grid analysis)**

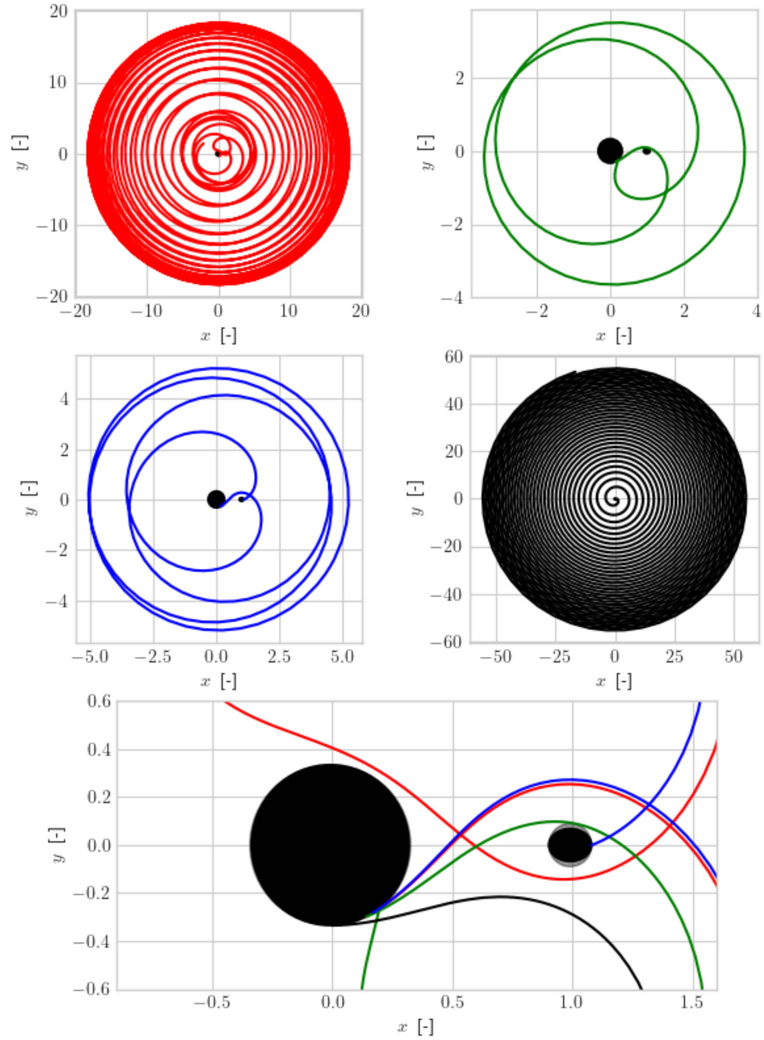

Fig. 17 Examples of topology of trajectories for each of the four fates of the levitated particles (labelling analogous to the one found in fig. 12 and fig. 13)

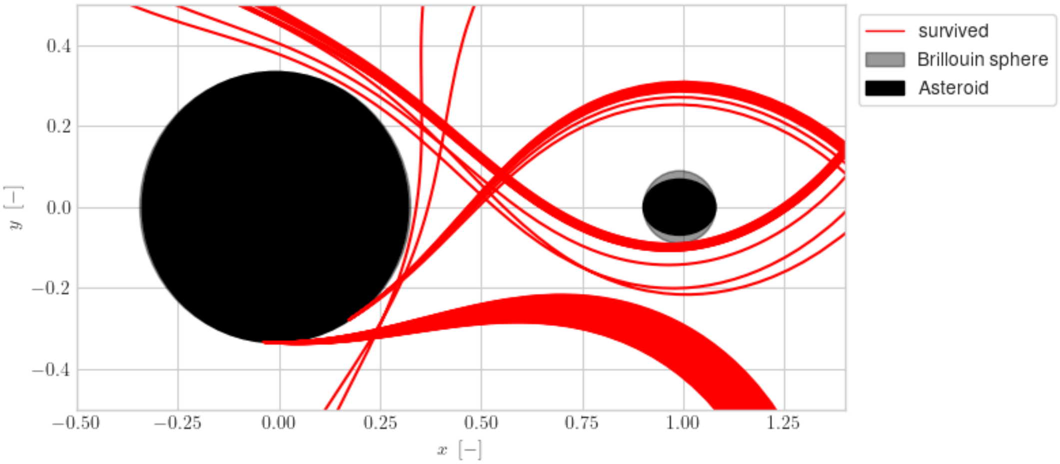

Fig. 18 Trajectories of 'survived' levitated particles from the refined analysis in the vicinity of the primaries

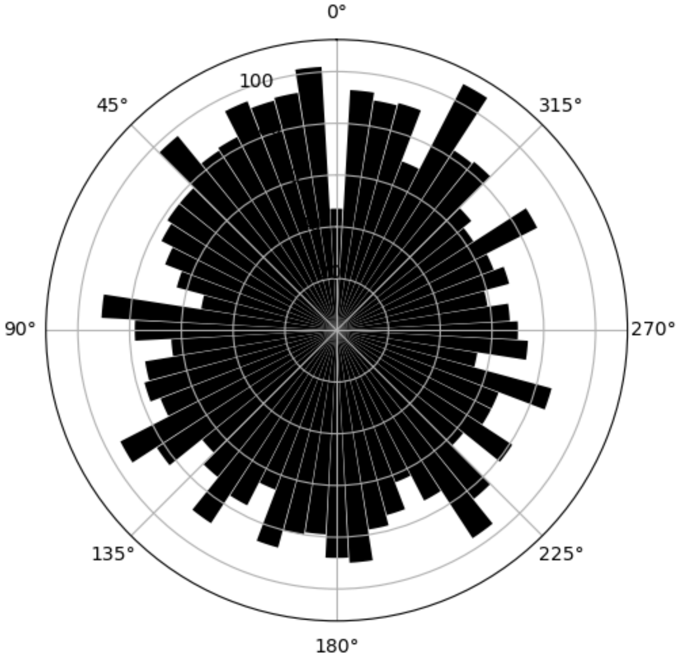

Fig. 19 Longitudinal histogram distribution of piercing the BS of Didymos at redeposition (example plot for $t = t_{BS}$, $\phi_0 = \pi$, $\Lambda_0 = 3\pi/2$)

Table 6 Statistics of the fates of levitated particles
(N_{total} - total number levitated particles, n_s - fraction of particles that survived, n_D - fraction of particles that collided with Didymos, n_d - fraction of particles that collided with Dimorphos, n_d^* - fraction of particles that collided with Dimorphos' non-Didymos-facing hemisphere)

Case number	ϕ_0	Λ_0	N_{total}	n_s	n_D	n_d	n_d^*	n_e
1	0	0	7592	28.09%	63.99%	7.17%	3.54%	0.75%
2	0	$\pi/2$	7588	31.51%	59.83%	7.26%	3.61%	1.40%
3	0	π	7592	28.54%	63.51%	7.09%	3.65%	0.85%
4	0	$3\pi/2$	7588	31.80%	59.70%	7.05%	3.44%	1.45%
5	$\pi/2$	0	7596	27.07%	64.65%	7.37%	3.78%	0.91%
6	$\pi/2$	$\pi/2$	7590	30.84%	60.50%	7.11%	3.49%	1.54%
7	$\pi/2$	π	7596	26.95%	64.47%	7.56%	3.98%	1.01%
8	$\pi/2$	$3\pi/2$	7590	30.95%	60.43%	7.06%	3.43%	1.55%
9	π	0	7596	26.90%	65.46%	7.28%	3.44%	0.47%
10	π	$\pi/2$	7588	29.65%	61.66%	7.09%	3.41%	1.59%
11	π	π	7596	25.99%	66.13%	7.29%	3.55%	0.59%
12	π	$3\pi/2$	7588	29.78%	61.54%	7.04%	3.26%	1.63%
13	$3\pi/2$	0	7596	26.97%	64.81%	7.70%	4.25%	0.51%
14	$3\pi/2$	$\pi/2$	7590	30.79%	60.30%	7.39%	3.83%	1.51%
15	$3\pi/2$	π	7596	26.80%	65.03%	7.58%	4.05%	0.58%
16	$3\pi/2$	$3\pi/2$	7590	30.88%	60.34%	7.29%	3.61%	1.49%

V. Regions of stable motion

This section discusses the methodology adopted to identify regions of stable motion in the Didymos system. First, the problem of periodicity in a non-autonomous dynamical system is analyzed. Then, the grid search approach is discussed along with the results thereof.

A. Periodicity

The ABP describes a non-autonomous system due to the time-dependency (in $\mathcal{F}$) of the primary's gravity field, the SRP acceleration and the third-body effect. Therefore, orbital motion in the system under analysis can only be periodic when it is aligned with the synodic periods (in $\mathcal{F}$) of the motion of the Sun and the rotation of Didymos. The synodic rotation rate of the primary is given, analogous to Equation (8), as

$$\Omega_D = \left(T_b^{-1} + T_D^{-1}\right) T_b \,, \tag{24}$$

whereas the synodic period of the Sun's motion and Didymos' rotation is defined, respectively, as

$$(T_s)_{\mathcal{F}} = T_s \ Q_s \tag{25}$$

$$(T_D)_{\mathcal{F}} = T_D \ Q_D \ . \tag{26}$$

Table 7 lists the smallest common multiples of the two synodic periods. The periods were assumed to be within the tolerances specified in Table 3 and Table 1. Since the period of the heliocentric orbit of the binary $\underline{T}_h$ is approximately 770 days, we consider only the smallest value presented in Table 7 for the analysis; if larger periods were analyzed, the assumed constant magnitude of the SRP perturbation in the ABP would introduce large errors in the results due to the large eccentricity of the binary's heliocentric orbit.

Table 7 Periods asserting true periodicity in the Didymos system

Period T ($\underline{T}$)	Multiple of $(T_D)_{\mathcal{F}}$	Multiple of $(T_s)_{\mathcal{F}}$
69.07 (5 d 11.00 h)	47	11
301.46 (23 d 19.75 h)	205	48
370.57 (29 d 6.83 h)	252	59
672.03 (53 d 2.57 h)	457	107
741.14 (58 d 13.66 h)	504	118

B. Grid search

Due to the time-dependent nature of the problem at hand and the clearly defined targeted period of the sought solution, a period-constrained differential correction scheme given by Heiligers et al. [53] was analyzed for its performance when applied to the problem of this work. However, due to the multiple-revolution topology of all of the candidate trajectories to be optimized using said correction scheme, this single-shooting method was incapable of reaching convergence. We selected the conventional grid search technique to ensure non-diverging behavior of the optimization algorithm; however, we recommend investigating the performance of multiple-shooting methods to attempt an improvement in the computational efficiency of the periodic-orbit search.

We use a classical grid search technique to identify initial conditions that lead to quasi-periodic solutions [54]. The search is divided into two stages: coarse and refined. The coarse search studies the entirety of the discretized search domain (see Table C1) via propagating the initial conditions over a time span T in the ABP model. Around the nodes in the grid search where $\|\mathbf{x}(t = 0) - \mathbf{x}(t = T)\| \leq 0.1$ (see Table 8), a refined grid search is performed (the discretization around these nodes is outlined in Table C2). By lowering the constraint on the Euclidean norm of the distance between the initial and final conditions in the refined search to 0.01, only two sets of initial conditions for quasi-satellite orbits (QSO) and two for distant retrograde orbits (DRO) trajectories were found to satisfy the condition (see Table 9 and their visual representation respectively in fig. 20). The presented refinement of the domain resulted in an improvement of the solutions by a factor of 2 and 5 (Table 8), respectively to the DO and QSO, and may be performed iteratively to further improve the precision of the solutions. The search has been performed for $\phi_0 = \Lambda_0 = 0$.

Table 8 Overview of the coarse and refined grid search results

Stage	No. of nodes	Threshold value of $\|\mathbf{x}(t=0) - \mathbf{x}(t=T)\|$	No. of solutions	Smallest value of $\|\mathbf{x}(t=0) - \mathbf{x}(t=T)\|$
DO				
Coarse	16335	0.1	15	0.0145
Fine	17760	0.01	2	0.0073
QSO				
Coarse	20700	0.1	23	0.0271
Fine	54450	0.01	2	0.0054

Table 9 Solutions of the grid search

ID	$\mathbf{x}(t=0)$ [−]	$\|\mathbf{x}(T) - \mathbf{x}(0)\|$ [−]	$\|\underline{\mathbf{r}}(T) - \underline{\mathbf{r}}(0)\|$ [m]	$\|\underline{\dot{\mathbf{r}}}(T) - \underline{\dot{\mathbf{r}}}(0)\|$ [cm/s]
DO1	$[-1.68417602,\ 0,\ 0.024,\ 0.02,\ 2.56152879,\ 0]^T$	0.00731	5.435	0.016
DO2	$[-1.68417602,\ 0,\ 0.03,\ -0.1,\ 2.55597323,\ 0]^T$	0.00769	4.638	0.018
QSO1	$[-0.52096283,\ 0,\ 0,\ 0,\ 1.91061955,\ 0]^T$	0.00537	2.380	0.014
QSO2	$[-0.52096283,\ 0,\ 0,\ 0.005,\ 1.91061955,\ 0]^T$	0.00947	5.071	0.023

VI. Temporary capture

This section introduces the approach adopted to identify trajectories of the levitated regolith particles leading to temporary capture in the discovered bounded-motion trajectories. The results are discussed in the context of a mission risk analysis for the Hera spacecraft.

A. Methodology

Temporary capture of levitated particles may occur if the escape trajectory (in the state space sense) passes close to a trajectory identified as a periodic orbit [55]. The flow of the state space is not stationary due to the non-autonomous character of the problem; hence, the conventional 6-element state space does not represent all degrees of freedom of the problem. We expand the state space by two additional dimensions: the orientation of the primary Λ and the angular position of the third body in the bicircular problem ϕ. Hence, we effectively freeze the flow and may treat it as stationary in the eight-dimensional state space, which will be referred to as the 'augmented state space' $\mathbf{D}$ and a point in that space as an 'augmented state vector' $\mathbf{X}$.

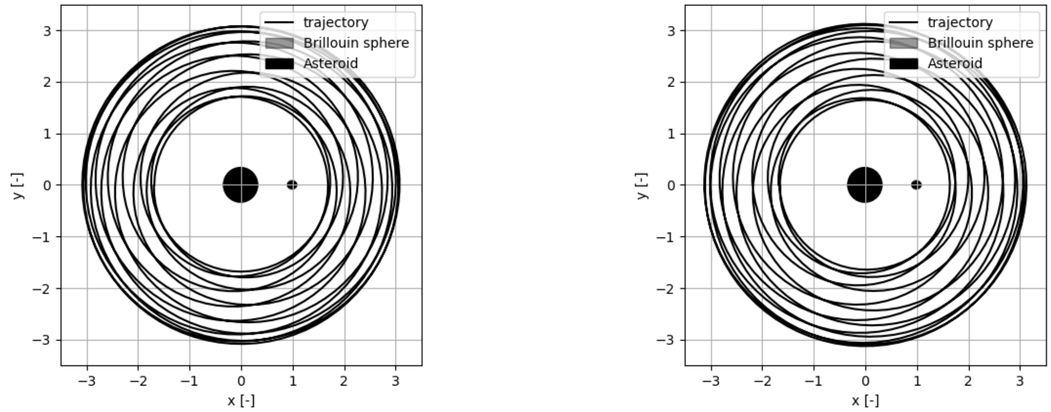

(a) DO1

(b) DO2

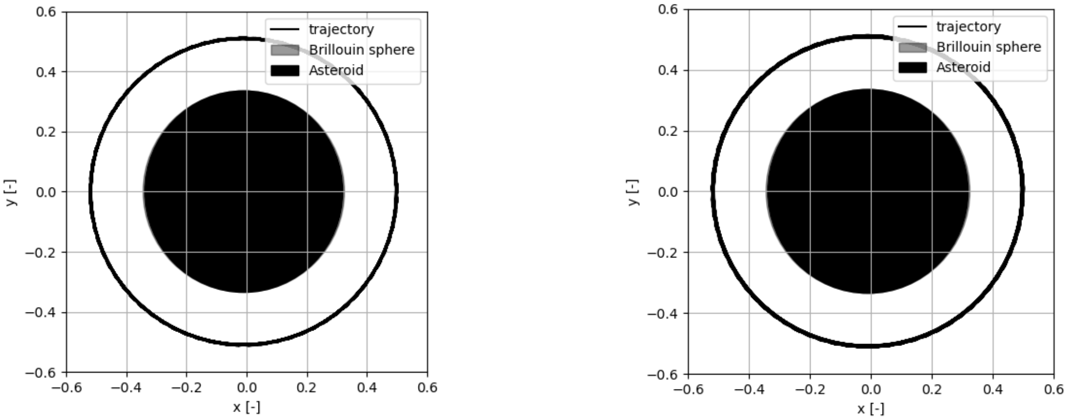

(c) QSO1

(d) QSO2

Fig. 20 Trajectories of DO1, DO2, QSO1, and QSO2 in the x-y plane of $\mathcal{F}$

Since virtually all temporary capture trajectories are anticipated to be composed of two segments of non-zero length, i.e., a propagated levitation trajectory originating at the surface and a trajectory constituting part of the periodic orbit, they are referred to as the levitation and orbital segments of the temporary capture trajectory. These trajectories are denoted as $C_{\mathbf{x}_l}$ and $C_{\mathbf{x}_o}$, respectively (see Equation (27)). The occurrence of temporary capture is determined by finding the capture error, i.e., the minimum distance d^* between the levitation and orbital trajectories in $\mathbf{D}$. Effectively, this procedure consists in calculating the sum of three Euclidean distance matrices using the distance operator d [56], of which the minimum off-diagonal element is the result of the operation

$$d^*(C_{\mathbf{X}_l}, C_{\mathbf{X}_o}) = \min_{\mathbf{X}_l \in C_{\mathbf{X}_l}, \mathbf{X}_o \in C_{\mathbf{X}_o}} \left(d(\mathbf{x}_l, \mathbf{x}_o) + d(\boldsymbol{\Lambda}_l, \boldsymbol{\Lambda}_o) + d(\boldsymbol{\phi}_l, \boldsymbol{\phi}_o) \right) \tag{27}$$

where $\boldsymbol{\phi}$ and $\boldsymbol{\Lambda}$ are the corresponding state history vectors of ϕ and Λ.

B. Discussion of results

Table 10 gives an overview of the minimum temporary capture errors for the selected orbits. The results obtained for QSO1 and QSO2 indicate the smallest capture error at $t = 0$, i.e., at piercing the BS upon levitation, which is not the case for DO1 and DO2. The capture errors found in the analysis are large, where the largest contributing factor is the error in the state vector. The smallest capture error was found for the DO1 orbit, which amounts for 0.3276 error in position (equivalent to 389.84 m) and 0.3858 in velocity (corresponding to 1.056 cm/s). We anticipate two possible reasons for such magnitudes of capture errors. First, the distance calculated using Equation (27) does not account for different weights given to various components of the augmented state vector. Another factor that might result in reduced accuracy of the identified temporary capture trajectories is the discretization of the trajectory. Equation (27) identifies the closest pair-wise distance between individual (augmented) state vectors but does not account for the fact that the studied trajectories are continuous.

Since the smallest capture error for the QSOs is significantly larger than those for the DO case and corresponds to the instant of levitation of the particles, we consider only the DO temporary capture cases for further discussion. The distribution of capture errors on the surface of Didymos (see Figure 22) does not render any trivial correlation between the levitation coordinates, the system state variables, and the capture error magnitude. As shown in the trajectory plot of the best solution (characterized by the smallest $d(C_{\mathbf{X}_l}, C_{\mathbf{X}_o})$) given in Figure 21, the two trajectories do not appear to be close to intersecting. Therefore, the results are not sufficient to formulate conclusions with regards to the feasibility or infeasibility of temporary capture of off-Didymos-levitated regolith particles into periodic orbits in the binary system.

In light of the large capture errors, in particular in the case of QSOs, for further research we recommend restricting the set of orbits considered for possible temporary capture by studying only orbits of similar orbital energy amplitudes as the levitated particles. The analysis could be further improved by interpolation of the trajectory (or, to preserve computational resources, only selected segments where trajectories pass in close vicinity to one another). Then, the distance could be found analytically, i.e., through solving a system of eight differential equations derived from the squared difference of the two interpolated trajectory segments $\left(\tilde{C}_{\mathbf{X}_l} - \tilde{C}_{\mathbf{X}_o}\right)^2$, or numerically, e.g., by refining the discretization of the trajectories used in Equation (27).

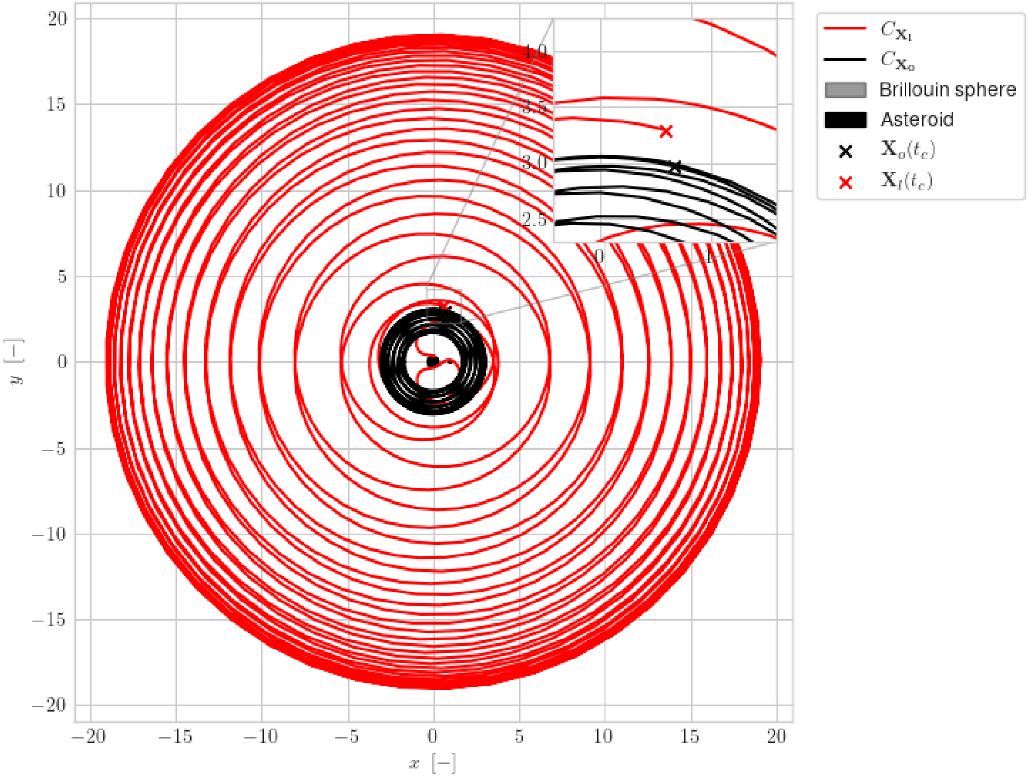

Fig. 21 Plot of the levitation and periodic orbit trajectories of the smallest capture error case (DO1)

Table 10 Temporary capture results

Orbit ID	Lev. case	$d^*(C_{\mathbf{X}_l}, C_{\mathbf{X}_o})$ [-]*	$d(\Lambda_l(t_c), \Lambda_o(t_c))$ [rad]	$d(\phi_l(t_c), \phi_o(t_c))$ [rad]	$d(\mathbf{x}_l(t_c), \mathbf{x}_o(t_c))$ [-]
QSO1	1	0.85421	0	0	0.85421
QSO2	1	0.85436	0	0	0.85436
DO1	8	0.52864	0.00087	0.02160	0.50617
DO1	6	0.58766	0.01207	0.03886	0.53673

* - the units for $d(\Lambda_l(t_c), \Lambda_o(t_c))$ and $d(\phi_l(t_c), \phi_o(t_c))$ are dropped in Equation (27)

C. Regions of increased Hera-regolith collision risk

Assessment of the threat posed by the regolith particles to a spacecraft visiting the binary system is conducted by first analyzing all findings of this work to identify trends in long-timescale motion of the dust grains and, subsequently, quantitatively investigating these phenomena. First, the primary region of hazard to the spacecraft would be the vicinity of the invariable plane of the system due to the small latitudes of levitated conditions and given the symmetry in the z-axis of the ABP and PDM. The discussions given in Section IV and Section VI.B suggest three types of regolith particle trajectories that might be of significant hazard to a spacecraft performing *in situ* observations in the Didymos system, such as Hera: (1) levitated trajectories destined to escape the binary (in short, "escaping" trajectories), as their slow motion toward the Hill Sphere would create a disk of regolith orderly moving outwards of the binary system in an orderly manner, (2) chaotic, non-periodic survived trajectories of particles levitated from Didymos ("chaotic" trajectories), as they tend to remain within the binary for extended periods of time ($3T$ corresponds to a time span longer than 15 days), and (3) levitated particles captured into periodic orbits ("captured" trajectories) due to their inherently very extended times of deposition in orbit (in theory, such particles should be in their orbits for infinite time periods).

The escaping trajectories are included in the glossary of risk-posing trajectories due to their extended travel time from levitation to crossing the Hill Sphere. Escape trajectories of travel time beyond 15 days have been identified in the analysis given in Section IV. This observation, in light of the uncertain levitation rate from Didymos due to a lack of *in situ* studies, renders a possible scenario of a deadly dust disk surrounding the binary system which slowly spirals outwards and ultimately escapes its sphere of influence. The chaotic trajectories, similar as in the case of escaping trajectories, pose significant threat to a probe in the binary system due to the large uncertainty in their orbital lifetime. The captured trajectories, i.e., levitation trajectories that smoothly transition into perfect periodic orbits, (in theory) have a infinite orbital lifetime; however, given all dynamical perturbances not accounted for in this study, such solutions are inherently unstable and existence of such trajectories must be proven by *in situ* studies. Trajectories found in this research (such as in Figure 21) constitute a solid stepping stone for further refinement of the results, although we do not yet deem them of satisfactory precision to draw conclusions for high-fidelity mission planning of the Hera spacecraft.

As given in Table 6, the levitation analysis showed that the survival rate after a time $3T$ of the levitated particles is 16-68 times larger than the escape rate. Accounting for the regions of motion of the two types of fates of the levitated particles (for an example refer to Figure 17), we anticipate two dust disks to exist around the binary system: (1) the outer disk is composed of regolith particles that follow escaping trajectories; the dust grains can be found as far as the Hill Sphere, their motion is highly ordered, and an approximately uniform density in the disk is expected, whereas (2) the inner disk spans as far as 20 km from the barycenter of the binary, motion of particles is chaotic, which suggests an existence of both time- and spatial fluctuations of the disk density. The ultimate fate of the inner-disk trajectories is likely a collision with one of the asteroids; however given the small escape rates of the dust from the system after levitation, the regolith relocation mechanism proposed in Section IV.E.3, and the long orbital lifetimes of the inner-disk trajectories, we anticipate that the inner disk is an ever-changing, dynamic, and self-exciting dust cloud spanning 20 km from the barycenter of the system in the invariable plane and up to 80 m in the normal-to-invariable-plane direction. Nevertheless, due to the uncertainties related to the properties of the asteroids of the Didymos binary, it is impossible to assess the densities of the two dust disks without the *in situ*-collected information about the levitation mass flow off Didymos, which the DART-accompanying probes might soon deliver [7].

VII. Conclusions

In this paper, motion of superficial regolith particles levitated from Didymos, the primary body of the Didymos binary asteroid system, has been studied in order to identify regions of elevated risks for the Hera spacecraft. The work has been divided into three major stages: (1) analysis of levitation of the superficial boulders of 5 cm in diameter, which also included numerical propagation of the trajectories to determine their fates, (2) grid searches for periodic orbits in the vicinity of the invariable plane of the system, and (3) based on the results of the former stages to determine whether the levitation of dust particles may lead to temporary capture in a periodic orbit.

The employed high-fidelity dynamical model enabled exposing numerous intricacies of the behavior of levitated regolith grains. Iterative grid searches allowed to identify four periodic orbits under the imposed tolerance: two distant retrograde orbits, i.e., revolving around the binary system, and two quasi-satellite orbits, i.e., revolving around the primary body, Didymos. Analysis of the orbital evolution of trajectories originating upon levitation from the primary body, Didymos, resulted in a comprehensive overview of the behavior of the loose regolith from the equatorial regions of Didymos. Approximately 60% of the levitated particles were found to redeposit on Didymos within 15 days of levitation, whereas 7% of the levitated particles collide with the secondary body, Dimorphos. The rate of collision with Dimorphos is approximately equal between the Didymos- and outer space-facing hemispheres of the tidally-locked moonlet. One of the most important takeaways of the study is the discovery of escape of a relatively large portion of the levitated particles (about 1%) through a gravitational slingshot mechanism, i.e., ejection of the particles outside the Hill Sphere of the binary system after close encounter with Dimorphos. Almost 30% of the levitated trajectories remain in the binary system (do not escape and do not deposit on any of the asteroids) after the propagation period slightly exceeding 15 days; prominent existence of dust ejecta clouds in the Didymos system months after the DART spacecraft's impact indicate that the survival periods might be much longer than the 15 days which constituted the propagation limit in the study. The phenomena of extended survival in the binary system and slow, spiraling escape from the system suggest existence of a very polluted (in the sense of the regolith) regions throughout the binary system, in the vicinity of its invariable plane. Existence of two dust disks has been suggested as potential region of elevated hazard for the visiting spacecraft. Temporary capture of particles in periodic orbits in the binary system has not been demonstrated due to large capture errors (the smallest approach between two trajectories - one levitation and one periodic trajectory - was found to be characterized by a position error of approximately 400 m and a velocity error of above 1 cm/s).

The findings are anticipated to render important contributions to planning of the Hera spacecraft's operations in the Didymos system and to provide a valuable starting point for further investigation of the dust dynamics in said system. We deem the demonstrated methodology applicable for studying the dynamics of particles larger than 0.1 µm, as below this threshold the motion of regolith particles is dominated by the effects of electrostatic forces [57]. The study was based on several assumptions, such as the assumption of planar motion of the Sun around the binary, constant distance to the Sun, and simplified shapes of the primaries. Moreover, a range of diameters of particles under consideration could be expanded and applying multiple-shooting methods for identifying periodic orbit could be investigated. Furthermore, the recent arrival of the DART probe to the binary is expected to deliver much more detailed data on the binary and remove numerous uncertainties pointed out in this work.

Appendix

A. Frame transformations

Transformation of position vectors is explained using the example of the Didymos-fixed frame ('D' index); however, the same relations hold for the Dimorphos-fixed one ('d' index). The transformation of the position vector between the Didymos-fixed ($\mathcal{F}_D$) and the synodic ($\mathcal{F}$) frame is given by

$$\mathbf{r} = \mathbb{R}_{D,s}(\Lambda_D)\mathbf{r}_D + \mathbf{T}_{D,s} \tag{28}$$

where $\mathbb{R}_{D,s}(\Lambda_D)$ and $\mathbf{T}_{D,s}$ are the Didymos-fixed-to-synodic rotation matrix by the Didymos's angle of rotation Λ_D (since the system is semi-asynchronous, $\Lambda_d = 0$) and the Didymos-fixed-to-synodic translation vector, respectively given by

$$\mathbb{R}_{D,s}(\Lambda_D) = \begin{bmatrix} \cos(\Lambda_D) & -\sin(\Lambda_D) & 0 \\ \sin(\Lambda_D) & \cos(\Lambda_D) & 0 \\ 0 & 0 & 0 \end{bmatrix} \tag{29}$$

$$\mathbf{T}_{D,s} = \mathbf{r}_D \tag{30}$$

The opposite transformation is defined as

$$\mathbf{r}_D = \mathbb{R}_{s,D}(\Lambda_D)\left[\mathbf{r} + \mathbf{T}_{s,D}\right] = \mathbb{R}^{-1}_{D,s}(\Lambda_D)\left[\mathbf{r} - \mathbf{T}_{D,s}\right] = \mathbb{R}^{T}_{D,s}(\Lambda_D)\left[\mathbf{r} - \mathbf{r}_D\right] \tag{31}$$

B. Eclipse model

To determine the lighting condition at a specific point, we derive the radius of the ellipsoid as seen from the perspective of the third body, i.e., projected on a plane normal to $\hat{\mathbf{S}}$. We define the eclipse reference frame of Didymos (however, the same approach is used for Dimorphos) $\mathcal{F}_{e_D}$ with the origin at the center of mass of Didymos, the x_{e_D}-axis points in the direction of $\hat{\mathbf{S}}$, the z_{e_D}-axis is aligned in the direction of z and the y_{e_D} completes the orthonormal system $\mathcal{F}_{e_D}(x_{e_D}, y_{e_D}, z_{e_D})$. The equation of an ellipse rotated by $\alpha_{e_D} = \Lambda_D - \phi$, i.e., the x_{e_D}-y_{e_D} projection of the ellipsoid's equator ($\delta_D = 0$, $r_D(\lambda_D, \delta_D) = r_{ell_D}(\lambda_D, \delta_D)$) in $\mathcal{F}_{e_D}$ (as in fig. A1) is

$$\frac{[x_D \cos(\alpha_{e_D}) - y_D \sin(\alpha_{e_D})]^2}{a_D^2} + \frac{[x_D \sin(\alpha_{e_D}) + y_D \cos(\alpha_{e_D})]^2}{b_D^2} - 1 = 0 \tag{32}$$

which in polynomial form yields

$$\underline{A}_D\, x_D^2 + \underline{B}_D\, x_D\, y_D + \underline{C}_D\, y_D^2 - 1 = 0 \tag{33}$$

where

$$\underline{A}_D = \left(\frac{\cos^2(\alpha_{e_D})}{a_D^2} + \frac{\sin^2(\alpha_{e_D})}{b_D^2}\right) \tag{34}$$

$$\underline{B}_D = 2\cos(\alpha_{e_D})\sin(\alpha_{e_D})\left(\frac{1}{a_D^2} - \frac{1}{b_D^2}\right) \tag{35}$$

$$\underline{C}_D = \left(\frac{\sin^2(\alpha_{e_D})}{a_D^2} + \frac{\cos^2(\alpha_{e_D})}{b_D^2}\right) \tag{36}$$

The equation of an ellipse might be interpreted as $y_D(x_D)$; therefore, we differentiate eq. (33) as a function of x_D to arrive at

$$\frac{\mathrm{d}y_D}{\mathrm{d}x_D} = \frac{-2\underline{A}_D x_D - \underline{B}_D y_D}{\underline{B}_D x_D + 2\underline{C}_D y_D}\ . \tag{37}$$

By setting the derivative to zero $\mathrm{d}y_{e_D}/\mathrm{d}x_{e_D} = 0$, we find the local extremum of $y_{e_D}(x_{e_D})|_{ext}$, i.e.,

$$y_D(x_D)|_{ext} = -\frac{2\underline{A}_D}{\underline{B}_D} x_D|_{ext} \tag{38}$$

for

$$x_D|_{ext} = \sqrt{-\frac{1}{\underline{A}_D - 4\underline{C}_D \dfrac{\underline{A}_D^2}{\underline{B}_D^2}}} \tag{39}$$

The projected radius is found from

$$r_{proj_D} = \sqrt{z_D^2 + \sin^2(\alpha_{e_D})\left(x_D^2 + y_D^2\right)} \tag{40}$$

where $\sin(\alpha_{e_D})\sqrt{x_D^2 + y_D^2}$ is the body-frame distance of the x_D-y_D plane projected onto the normal to the Sun-pointing vector $\hat{\mathbf{S}}$, i.e., the y_D-z_D plane.

Since every intersection of an ellipsoid and a plane generates an ellipse, we can conclude that the radius of the ellipsoid projected on the y-z plane is given by

$$r_{ecl} = \sqrt{(y_D(x_D)|_{ext})^2 + z_D^2} \tag{41}$$

C. Grid settings used in the periodic motion search

Table C1 Discretization of the state space in preparation for the coarse grid search

State vector element γ	γ_{min}	γ_{max}	$\Delta\gamma$
Quasi-satellite orbit around the primary - total of 20700 trajectories			
x	$-(-\mu - a_D)$	$-(1 - \mu - a_d)$	0.005
z	-0.06	0.06	0.03
$\dot{x}$	-0.05	0.05	0.025
$\dot{y} = \dot{y}(x)(1 + \delta\dot{y})$	$\delta\dot{y}_{min} = -0.1$	$\delta\dot{y}_{max} = 0.1$	$\Delta\delta\dot{y} = 0.025$
Distant orbits - total of 16335 trajectories			
x	$-(1 + \mu)$	$-(10 + \mu)$	0.075
z	-0.03	0.03	0.03
$\dot{x}$	-0.1	0.1	0.05
$\dot{y} = \dot{y}(x)(1 + \delta\dot{y})$	$\delta\dot{y}_{min} = -0.1$	$\delta\dot{y}_{max} = 0.1$	$\Delta\delta\dot{y} = 0.025$

Table C2 Discretization of the state space in preparation for the refined grid search around $[x_{ref} \ \ 0 \ \ z_{ref} \ \ \dot{x}_{ref} \ \ \dot{y}_{ref} \ \ 0]^T$

State vector element γ	γ_{min}	γ_{max}	$\Delta\gamma$
Quasi-satellite orbit around the primary			
x	$x_{ref} - 0.005$	$x_{ref} + 0.005$	0.001
z	$0.8z_{ref}$	$1.2z_{ref}$	$0.2z_{ref}$
$\dot{x}$	$\dot{x}_{ref} - 0.025$	$\dot{x}_{ref} + 0.025$	0.005
$\dot{y}$	$\dot{y}_{ref} - 0.025$	$\dot{y}_{ref} + 0.025$	0.005
Distant orbits			
x	$x_{ref} - 0.075$	$x_{ref} + 0.075$	0.015
z	$0.8z_{ref}$	$1.2z_{ref}$	$0.2z_{ref}$
$\dot{x}$	$\dot{x}_{ref} - 0.05$	$\dot{x}_{ref} + 0.05$	0.02
$\dot{y}$	$\dot{y}_{ref} - 0.025$	$\dot{y}_{ref} + 0.025$	0.005

References

[1] Planetary Science Communications, Jet Propulsion Laboratory, NASA, “Apophis,” , 2022. URL `https://solarsystem.nasa.gov/asteroids-comets-and-meteors/asteroids/apophis/in-depth/`, accessed on: 27-11-2022.

[2] McFadden, L. A., and Binzel, R. P., *Near-Earth Objects*, Gale virtual reference library, Elsevier Science, 2006.

[3] Dymock, R., *Asteroids and Dwarf Planets and How to Observe Them*, Astronomers’ Observing Guides, Springer New York, 2010. https://doi.org/10.1007/978-1-4419-6439-7.

[4] Dearborn, D. P. S., and Miller, P. L., *Defending Against Asteroids and Comets*, Handbook of Cosmic Hazards and Planetary Defense, Springer International Publishing, 2015. https://doi.org/10.1007/978-3-319-03952-7.

[5] Cheng, A. F., Rivkin, A. S., Michel, P., Atchison, J., Barnouin, O., Benner, L., Chabot, N. L., Ernst, C., Fahnestock, E. G., Kueppers, M., Pravec, P., Rainey, E., Richardson, D. C., Stickle, A. M., and Thomas, C., “AIDA DART asteroid deflection test: Planetary defense and science objectives,” *Planetary and Space Science*, Vol. 157, No. November 2017, 2018, pp. 104–115. https://doi.org/10.1016/j.pss.2018.02.015.

[6] Michel, P., Cheng, A., Küppers, M., Pravec, P., Blum, J., Delbo, M., Green, S. F., Rosenblatt, P., Tsiganis, K., Vincent, J. B., Biele, J., Ciarletti, V., Hérique, A., Ulamec, S., Carnelli, I., Galvez, A., Benner, L., Naidu, S. P., Barnouin, O. S., Richardson, D. C., Rivkin, A., Scheirich, P., Moskovitz, N., Thirouin, A., Schwartz, S. R., Campo Bagatin, A., and Yu, Y., “Science case for the Asteroid Impact Mission (AIM): A component of the Asteroid Impact & Deflection Assessment (AIDA) mission,” *Advances in Space Research*, Vol. 57, No. 12, 2016, pp. 2529–2547. https://doi.org/10.1016/j.asr.2016.03.031.

[7] Michel, P., Kueppers, M., Sierks, H., Carnelli, I., Cheng, A. F., Mellab, K., Granvik, M., Kestilä, A., Kohout, T., Muinonen, K., Näsilä, A., Penttila, A., Tikka, T., Tortora, P., Ciarletti, V., Hérique, A., Murdoch, N., Asphaug, E., Rivkin, A., Barnouin, O., Bagatin, A. C., Pravec, P., Richardson, D. C., Schwartz, S. R., Tsiganis, K., Ulamec, S., and Karatekin, O., “European component of the AIDA mission to a binary asteroid: Characterization and interpretation of the impact of the DART mission,” *Advances in Space Research*, Vol. 62, No. 8, 2018, pp. 2261–2272. https://doi.org/10.1016/j.asr.2017.12.020.

[8] Planetary Science Communications, Jet Propulsion Laboratory, NASA, “Didymos & Dimorphos,” , 2022. URL https://solarsystem.nasa.gov/asteroids-comets-and-meteors/asteroids/didymos/in-depth/, accessed on: 27-11-2022.

[9] Safety & Security, European Space Agency, “Hera, Bonus Science,” , 2020. URL https://www.esa.int/Safety_Security/Hera/Bonus_science, accessed on: 20-11-2020.

[10] Cheng, A. F., Stickle, A. M., Fahnestock, E. G., Dotto, E., Della Corte, V., Chabot, N. L., and Rivkin, A. S., “DART mission determination of momentum transfer: Model of ejecta plume observations,” *Icarus*, Vol. 352, No. November 2019, 2020, p. 113989. https://doi.org/10.1016/j.icarus.2020.113989.

[11] Zhang, Y., Richardson, D. C., Barnouin, O. S., Maurel, C., Michel, P., Schwartz, S. R., Ballouz, R. L., Benner, L. A., Naidu, S. P., and Li, J., “Creep stability of the proposed AIDA mission target 65803 Didymos: I. Discrete cohesionless granular physics model,” *Icarus*, Vol. 294, 2017, pp. 98–123. https://doi.org/10.1016/j.icarus.2017.04.027.

[12] Yu, Y., Michel, P., Hirabayashi, M., Schwartz, S. R., Zhang, Y., Richardson, D. C., and Liu, X., "The Dynamical Complexity of Surface Mass Shedding from a Top-shaped Asteroid Near the Critical Spin Limit," *The Astronomical Journal*, Vol. 156, No. 2, 2018, p. 59. https://doi.org/10.3847/1538-3881/aaccf7.

[13] Yu, Y., and Michel, P., "Ejecta cloud from the AIDA space project kinetic impact on the secondary of a binary asteroid: II. Fates and evolutionary dependencies," *Icarus*, Vol. 312, 2018, pp. 128–144. https://doi.org/10.1016/j.icarus.2018.04.017.

[14] Yu, Y., Michel, P., Hirabayashi, M., and Richardson, D. C., "The expansion of debris flow shed from the primary of 65803 Didymos," *Monthly Notices of the Royal Astronomical Society*, Vol. 484, No. 1, 2019, pp. 1057–1071. https://doi.org/10.1093/mnras/sty3515.

[15] Sánchez, P., and Scheeres, D. J., "Cohesive regolith on fast rotating asteroids," *Icarus*, Vol. 338, No. September, 2019. https://doi.org/10.1016/j.icarus.2019.113443.

[16] Scheeres, D. J., "Landslides and mass shedding on spinning spheroidal asteroids," *Icarus*, Vol. 247, 2015, pp. 1–17.

[17] Ferrari, F., and Lavagna, M., "Ballistic landing design on binary asteroids: The AIM case study," *Advances in Space Research*, Vol. 62, No. 8, 2018, pp. 2245–2260.

[18] Oliveira, T. C., and Prado, A. F., "Search for stable orbits around the binary asteroid systems 1999 KW4 and didymos," *Revista Mexicana de Astronomia y Astrofisica*, Vol. 56, No. 1, 2020, pp. 113–128. https://doi.org/10.22201/ia.01851101p.2020.56.01.12.

[19] Capannolo, A., Ferrari, F., and Lavagna, M., "Families of Bounded Orbits near Binary Asteroid 65803 Didymos," *Journal of Guidance, Control, and Dynamics*, Vol. 42, No. 1, 2019, pp. 189–198. https://doi.org/10.2514/1.G003437.

[20] Jean, I., Misra, A. K., and Ng, A., "Solar radiation pressure-compatible trajectories in the vicinity of a binary asteroid," *Journal of Guidance, Control, and Dynamics*, Vol. 42, No. 6, 2019, pp. 1319–1329. https://doi.org/10.2514/1.G004007.

[21] Dell'Elce, L., Baresi, N., Naidu, S., Benner, L., and Scheeres, D., "Numerical investigation of the dynamical environment of 65803 Didymos," *Advances in Space Research*, Vol. 59, No. 5, 2017, pp. 1304–1320.

[22] Lasagni Manghi, R., Modenini, D., Zannoni, M., and Tortora, P., "Preliminary orbital analysis for a CubeSat mission to the Didymos binary asteroid system," *Advances in Space Research*, Vol. 62, No. 8, 2018, pp. 2290–2305. https://doi.org/10.1016/j.asr.2017.12.014.

[23] Silva Neto, J. B., Sanchez, D. M., and Prado, A. F., "Co-orbital orbits around the asteroid 65803 didymos (1996 GT)," *Space Flight Mechanics Meeting, 2018*, , No. 210009, 2018. https://doi.org/10.2514/6.2018-0719.

[24] Yu, Y., Michel, P., Schwartz, S. R., Naidu, S. P., and Benner, L. A., "Ejecta cloud from the AIDA space project kinetic impact on the secondary of a binary asteroid: I. mechanical environment and dynamical model," *Icarus*, Vol. 282, 2017, pp. 313–325. https://doi.org/10.1016/j.icarus.2016.09.008.

[25] Wiegert, P., "On the Delivery of DART-ejected Material from Asteroid (65803) Didymos to Earth," *The Planetary Science Journal*, Vol. 1, No. 1, 2020, p. 3. https://doi.org/10.3847/psj/ab75bf.

[26] Fujiwara, A., Kawaguchi, J., Yeomans, D., Abe, M., Mukai, T., Okada, T., Saito, J., Yano, H., Yoshikawa, M., Scheeres, D., et al., "The rubble-pile asteroid Itokawa as observed by Hayabusa," *Science*, Vol. 312, No. 5778, 2006, pp. 1330–1334.

[27] Lauretta, D., Hergenrother, C., Chesley, S., Leonard, J., Pelgrift, J., Adam, C., Al Asad, M., Antreasian, P., Ballouz, R.-L., Becker, K., et al., "Episodes of particle ejection from the surface of the active asteroid (101955) Bennu," *Science*, Vol. 366, No. 6470, 2019.

[28] Watanabe, S., Hirabayashi, M., Hirata, N., Hirata, N., Noguchi, R., Shimaki, Y., Ikeda, H., Tatsumi, E., Yoshikawa, M., Kikuchi, S., et al., "Hayabusa2 arrives at the carbonaceous asteroid 162173 Ryugu—A spinning top–shaped rubble pile," *Science*, Vol. 364, No. 6437, 2019, pp. 268–272.

[29] Solar System Dynamics, Jet Propulsion Laboratory, NASA, "65803 Didymos (1996 GT)," , 2020. URL https://ssd.jpl.nasa.gov/sbdb.cgi?sstr=65803, accessed on: 23-11-2020.

[30] Pravec, P., Benner, L. A. M., Nolan, M. C., Kusnirak, P., Pray, D., Giorgini, J. D., Jurgens, R. F., Ostro, S. J., Margot, J. L., Magri, C., Grauer, A., and Larson, S., "(65803) 1996 GT," , Vol. 8244, 2003, p. 2.

[31] Pravec, P., Scheirich, P., Kušnirák, P., Šarounová, L., Mottola, S., Hahn, G., Brown, P., Esquerdo, G., Kaiser, N., Krzeminski, Z., et al., "Photometric survey of binary near-Earth asteroids," *Icarus*, Vol. 181, No. 1, 2006, pp. 63–93.

[32] Naidu, S. P., Benner, L. A., Brozovic, M., Nolan, M. C., Ostro, S. J., Margot, J. L., Giorgini, J. D., Hirabayashi, T., Scheeres, D. J., Pravec, P., Scheirich, P., Magri, C., and Jao, J. S., "Radar observations and a physical model of binary near-Earth asteroid 65803 Didymos, target of the DART mission," *Icarus*, Vol. 348, No. March, 2020, p. 113777. https://doi.org/10.1016/j.icarus.2020.113777.

[33] Agrusa, H., Tsiganis, K., Gkolias, I., Richardson, D., Davis, A., Fahnestock, E., and Hirabayashi, M., "On the post-impact spin state of the secondary component of the Didymos-Dimorphos binary asteroid system," *AAS/Division for Planetary Sciences Meeting Abstracts*, Vol. 52, 2020, pp. 217–04.

[34] European Space Research and Technology Centre, "ASTEROID IMPACT MISSION: DIDYMOS REFERENCE MODEL," 2014.

[35] Damme, F., Hussmann, H., and Oberst, J., "Spacecraft orbit lifetime within two binary near-Earth asteroid systems," *Planetary and Space Science*, Vol. 146, 2017, pp. 1–9.

[36] Agrusa, H. F., Richardson, D. C., Davis, A. B., Fahnestock, E., Hirabayashi, M., Chabot, N. L., Cheng, A. F., Rivkin, A. S., and Michel, P., "A benchmarking and sensitivity study of the full two-body gravitational dynamics of the DART mission target, binary asteroid 65803 Didymos," *Icarus*, Vol. 349, No. January, 2020. https://doi.org/10.1016/j.icarus.2020.113849.

[37] Richardson, D., Barnouin, O., Benner, L., Bottke, W., Campo Bagatin, A., Cheng, A., Hirabayashi, M., Maurel, C., McMahon, J., Michel, P., et al., "Dynamical and physical properties of 65803 Didymos," *LPI*, , No. 1903, 2016, p. 1501.

[38] Scheirich, P., and Pravec, P., "Modeling of lightcurves of binary asteroids," *Icarus*, Vol. 200, No. 2, 2009, pp. 531–547.

[39] Heiligers, J., and Scheeres, D. J., "Solar-sail orbital motion about asteroids and binary asteroid systems," *Journal of Guidance, Control, and Dynamics*, Vol. 41, No. 9, 2018, pp. 1947–1962.

[40] Szebehely, V., "Theory of orbits: the restricted three body problem," , 1967.

[41] Koon, W., Lo, M., Marsden, J., and Ross, S., "Dynamical Systems," *The Three-Body Problem, and Space Mission Design (Pasadena, CA, USA: California Institute of Technology)*, 2006.

[42] Scheeres, D. J., "Orbital motion in strongly perturbed environments: applications to asteroid, comet and planetary satellite orbiters," , 2016.

[43] Li, Z., Ziebart, M., Bhattarai, S., and Harrison, D., "A shadow function model based on perspective projection and atmospheric effect for satellites in eclipse," *Advances in Space Research*, Vol. 63, No. 3, 2019, pp. 1347–1359.

[44] McInnes, C. R., *Solar sailing: technology, dynamics and mission applications*, Springer Science & Business Media, 2004, Chap. 2. Solar radiation pressure.

[45] Villegas Pinto, D., Soldini, S., Tsuda, Y., and Heiligers, J., "Temporary capture of asteroid ejecta into periodic orbits: Application to jaxa's hayabusa2 impact event," *AIAA Scitech 2020 Forum*, Vol. 1 PartF, 2020, pp. 1–21. https://doi.org/10.2514/6.2020-0221.

[46] Liew, S. S., Khalil-Hani, M., and Bakhteri, R., "Bounded activation functions for enhanced training stability of deep neural networks on visual pattern recognition problems," *Neurocomputing*, Vol. 216, 2016, pp. 718–734.

[47] Yang, X., Liu, J., Yang, Y., Qing, Q., and Wen, G., "An Efficient Topology Description Function Method Based on Modified Sigmoid Function," *Mathematical Problems in Engineering*, Vol. 2018, 2018.

[48] Scheeres, D. J., "Minimum energy configurations in the N-body problem and the celestial mechanics of granular systems," *Celestial Mechanics and Dynamical Astronomy*, Vol. 113, No. 3, 2012, pp. 291–320. https://doi.org/10.1007/s10569-012-9416-0.

[49] Soldini, S., Takanao, S., Ikeda, H., Wada, K., Yuichi, T., Hirata, N., and Hirata, N., "A generalised methodology for analytic construction of 1:1 resonances around irregular bodies: Application to the asteroid Ryugu's ejecta dynamics," *Planetary and Space Science*, Vol. 180, No. September 2019, 2020, p. 104740. https://doi.org/10.1016/j.pss.2019.104740.

[50] Jones, E., Oliphant, T., Peterson, P., et al., "SciPy: Open source scientific tools for Python," , 2016.

[51] Hairer, E., Nørsett, S., and Wanner, G., "Solving ordinary differential equations, I: Nonstiff problems, Springer Verlag," *Berlin, Germany*, 1993.

[52] Nazarenko, V., Glazunova, L., and Karetnikov, V., "Roche-lobe overflow in the vicinity of the inner Lagrangian point in close binary systems," *Astronomy Reports*, Vol. 45, No. 6, 2001, pp. 452–460.

[53] Heiligers, J., Macdonald, M., and Parker, J. S., "Extension of Earth-Moon libration point orbits with solar sail propulsion," *Astrophysics and Space Science*, Vol. 361, No. 7, 2016, pp. 1–20.

[54] Shi, Y., Wang, Y., and Xu, S., "Global search for periodic orbits in the irregular gravity field of a binary asteroid system," *Acta Astronautica*, Vol. 163, No. July 2018, 2019, pp. 11–23. https://doi.org/10.1016/j.actaastro.2018.10.014.

[55] Scheeres, D. J., and Marzari, F., "Temporary orbital capture of ejecta from comets and asteroids: Application to the Deep Impact experiment," *Astronomy and Astrophysics*, Vol. 356, No. 2, 2000, pp. 747–756.

[56] Weyenberg, G., and Yoshida, R., "Reconstructing the Phylogeny: Computational Methods," *Algebraic and Discrete Mathematical methods for modern Biology*, Elsevier, 2015, pp. 293–319.

[57] Szalay, J. R., Poppe, A. R., Agarwal, J., Britt, D., Belskaya, I., Horányi, M., Nakamura, T., Sachse, M., and Spahn, F., *Dust Phenomena Relating to Airless Bodies*, Vol. 214, Springer Nature B.V., 2018. https://doi.org/10.1007/s11214-018-0527-0.

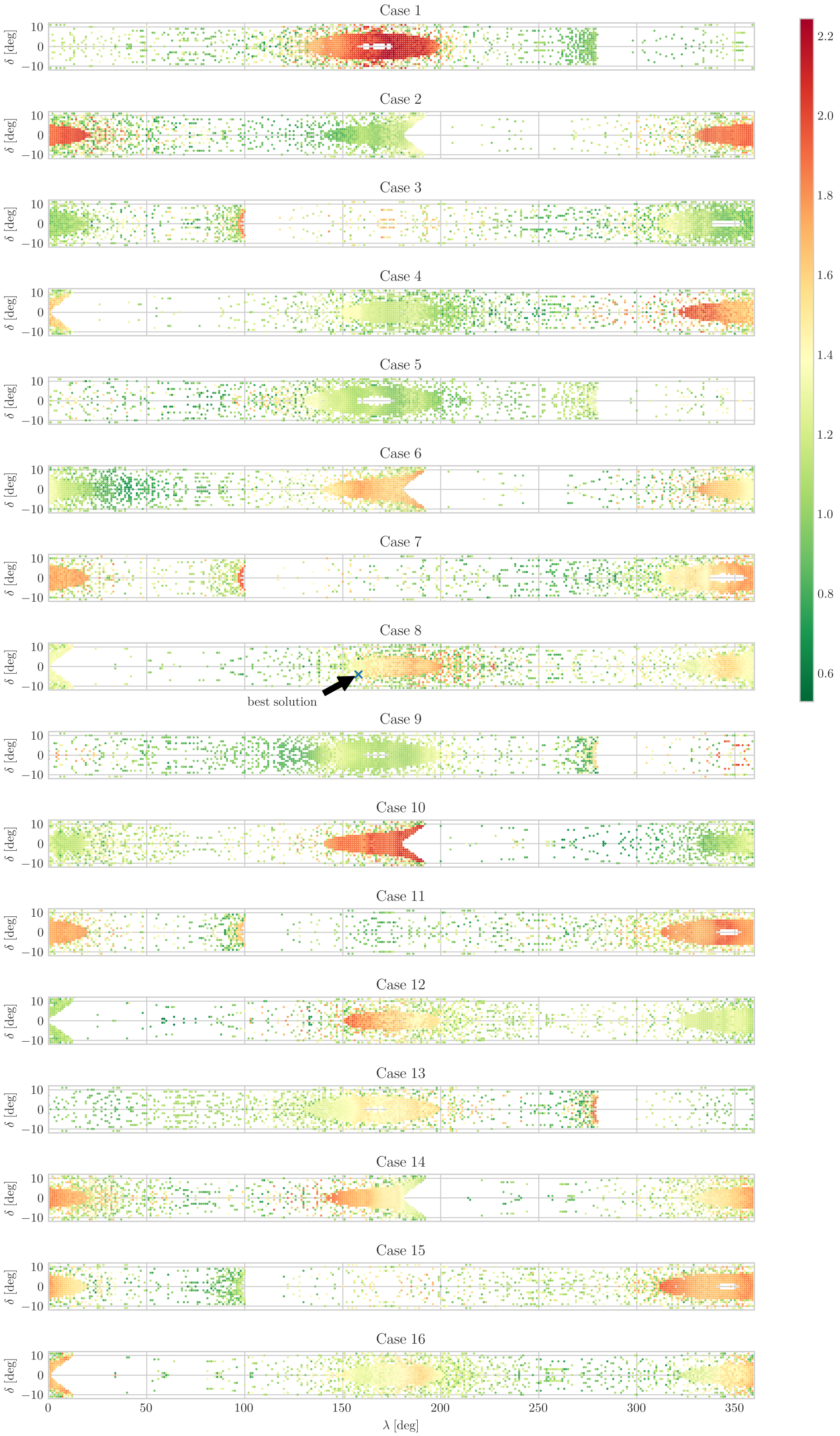

Fig. 22 Distribution of capture error on the surface grid of Didymos for levitated and 'survived' particles (plotted only for the best temporary-capture candidate - DO1)

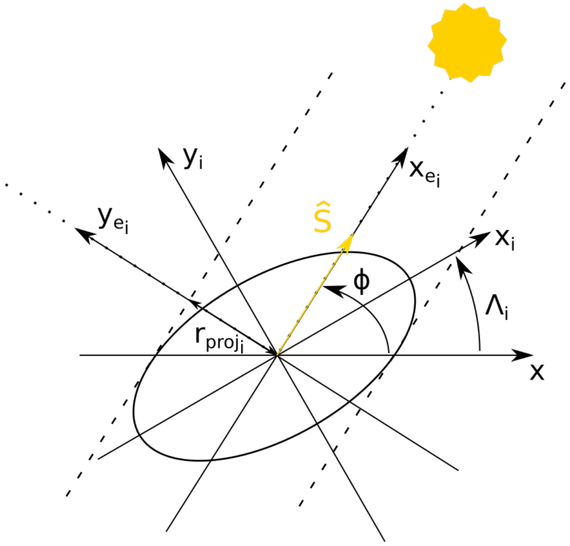

Fig. A1 Quantities used in eclipse determination

3

Conclusions

This chapter presents a review of the research objectives stated in chapter 1 and discusses the recommendations for future work as well as the implications of the conducted research.

3.1. Review of research objectives completion

The research objective to assess the hazard to the Hera spacecraft posed by naturally-levitated regolith particles, which was stated in section 1.1, has been achieved; the research presented in chapter 2 delivered qualitative results concerning the possibility of levitation of the regolith grains from the surface of Didymos and their fates using a dynamical model of higher fidelity than used in previous research on this topic. Regions of increased probability of encountering regolith particles has been identified and classified as two disks of differing densities and radii. Furthermore, the research subquestions were answered:

*Q*1 *"What are the regions of Didymos' mass loss?"*

The results obtained in the section *Regions of levitation* show a large rate of levitation experienced by superficial regolith particles in equatorial regions of Didymos. This finding is in agreement with other literature data cited in the same section. As presented in *Regions of levitation*, the levitation occurs for all the considered initial states of the binary system, i.e., all combinations of the initial orientation of the primary body and the position of the Sun in the Sun-oriented synodic reference frame $\mathscr{F}$, where the orientation of the primary and the position of the Sun were elements of $\{0, \frac{1}{2}\pi, \pi, \frac{3}{2}\pi\}$. The scope of the research was limited to the analysis of regolith levitation from rest. In the case of null initial relative velocity between the (potentially) levitated grain and the primary, location within approximately 12 degrees latitude to the north and south from the equator is frequently a sufficient condition for levitation from rest for particles of 5 cm in diameter. This strongly suggests that further investigation of this effect for various initial states of the augmented bicircular problem (ABP) and various particle sizes is needed.

*Q*2 *"Under which conditions can ejecta be temporarily captured in periodic or bounded orbits?"*

The results presented in the section *Temporary capture* do not deliver conclusive proofs for the existence of such trajectories. The capture errors found in the study are too large to ensure temporary capture (the smallest identified capture error is approximately 400 m and more than 1 cm/s); however, further improvement of the adopted methodology is deemed feasible.

As demonstrated in the section 'Regions of levitation', approximately 30% of the levitated particles survive for at least 15 days in the binary system, whereas an additional 60-65% re-deposit in equatorial regions of Didymos and are anticipated to levitate repetitively. Therefore, despite the fact that temporary capture was not identified in this research, the extended orbital lifetime for levitated particles combined with the repetitive levitation of a major portion thereof indicates a vast equatorial region on Didymos where bounded-motion trajectories originate.

*Q*3 *"What trajectories do the dust particles follow and, as result of that, what are the regions of higher collision risk in the context of AIDA?"*

Due to the symmetric nature of the adopted ABP in the direction normal to the invariable plane of the binary system, motion in the normal direction is purely harmonic; therefore, the motion of levitated regolith particles - under the assumption of a purely planar ABP - will happen close to the equatorial plane of the primary. Since the equatorial and invariable planes of the ABP coincide, due to the assumptions made in the section 'Dynamical model', the motion of levitated regolith particles may occur only in the vicinity of this plane. The results obtained in the study strongly hint at the existence of two dust disks in the invariable plane of the binary; the smaller disk is composed of surviving and redepositing regolith particles, is characterized by chaotic motion of the particles, whereas the outer disk is composed of regolith particles slowly spiraling outwards of the binary in an ordered manner and destined for escape.

The research presented in chapter 2 gives an overview of the dynamics of loose regolith particles in the Didymos binary system. On one hand, it demonstrates the regions of levitation (from rest) of the regolith grains which span along the equator of the larger asteroid in the binary system; on the other hand, the journal paper discusses fates of the levitated trajectories. It is shown that the majority of the levitated particles are subject to reaccretion on Didymos's surface. About a third of the levitated grains survives in orbit for an extended period of time (more than 15 days, which was the maximum propagation time adopted in the study). The remaining several percent of levitated particles are split into a fraction that is transferred and deposited on Dimorphos (approximately 7%) and a fraction that escapes the system (about 1%). Temporary capture of the levitated particles in periodic motion has not been shown - the capture errors found in the analysis were deemed too large to accept them as solutions to the problem. The closest approach between two segments of the potential capture trajectory are characterized by a position error of 400m and a velocity error of approximately 1cm/s.

3.2. Recommendations for future work

The recommendations for future work may be divided into four categories, depending on the reason for future investigation; namely, recommendations stemming from (1) the limitations of the dynamical model, (2) the limitations in coverage of the possible solutions domain, (3) the limitations of the adopted methodology, and (4) the limited exploration of the problem in light of the large uncertainties about the Didymos system.

The limitations of the dynamical model result in the most extensive list of recommendations:

1. *The eccentricity of the heliocentric orbit shall be accounted for in the dynamical model.*

   The model used in the research is derived from the assumption that the variation of the distance between the binary system and the Sun is negligible. This is only the case for very short periods, which played a key role in the determination of the period of the periodic trajectories to be taken into account in the study. The dynamical model shall be augmented by a varying distance from the Sun, which will result in epoch-dependent magnitudes of the SRP and third-body effect perturbations.

2. *The out-of-plane motion of the Sun in the synodic reference frame of the ABP shall be introduced in the dynamical model.*

   The orbit pole of the binary orbit indicates that the plane of the synodic frame $\mathscr{F}$ does not coincide with the plane of the heliocentric orbit; the inclination of the binary orbit is equal to 174 degrees, i.e., . The dynamical model adopted in this research assumes that both planes coincide. Fidelity of the results may increase upon incorporating a varying elevation of the Sun (currently null at all times) in .

3. *Higher-fidelity shape models shall be used for Didymos and Dimorphos in the dynamical model.*

   The assumption of ellipsoidal shapes of both bodies served the purpose of lowering the computational effort in order to facilitate extensive exploration of the domain of potential solutions. However, upon availability of more precise shape models for the primaries, it is recommended to employ those in the dynamical model and, taking the results of this study as an educated initial guess, produce high-fidelity results.

4. *The dynamical model shall be augmented by addition of more third-body effect perturbances.*

   Trajectories of asteroids are highly perturbed due to their relatively low masses. Since the Didymos binary is catalogued as a PHA, the binary system by definition approaches Earth on occasion. It is therefore necessary to investigate the effect of Earth's gravity on the dynamical behavior of the system.

It is recommended to not limit the additional perturbances to only Earth's gravitational effect but also to incorporate other third-body accelerations, e.g., from Venus, Mars, and the two inner gas giants, i.e., Jupiter and Saturn.

The results of the analysis presented in chapter 2 are derived from a highly discretized set of initial conditions. Despite performing a, for the needs of the problem at hand, fine discretization, an effect of such a heuristic approach is the coarseness visible in the results of the study. To increase the fidelity of the study, the following is recommended:

1. *The surface discretization of the primary body (Didymos) shall be performed on a finer grid.*

   The discretization parameters of the primary's surface in the study on the levitation of particles were calibrated by an initial trade-off analysis between the coverage of the levitation regions and computational effort necessary to be performed. However, upon availability of a more powerful computational unit, the discretization of the Didymos' surface shall be refined.

2. *The intersection of the results of the levitation study and the capture trajectory study shall account for the discretized character of the initial conditions leading to the results of both analyses.*

   The final results were obtained through calculation of the Euclidean norm between each possible combination of state vectors at the BS of the primary after levitation and before capture in a bounded motion trajectory. Interpolation of the state vectors on the BS for both cases might result in smooth, continuous sets of data, allowing for higher-fidelity analysis of the intersection of both sets of data. The interpolation scheme used for such a method must impose continuity of the solution and must produce a minimal-error solution with respect to the data points.

3. *The temporary capture analysis shall be conducted on a pair of refined or interpolated trajectory segments.*

   The results of the temporary capture analysis are deemed to bear additional error due to certain levels of discretization, which can be removed by conducting said analysis on interpolated segments of the trajectories.

4. *Further iterative grid search refinement shall be performed to improve the quality of the identified periodic orbits.*

   As presented in the section 'Regions of stable motion', a grid refinement resulted in a significant improvement of the results. This operation is deemed a viable optimization method. Nevertheless, the computational effort associated with it cannot be neglected and the previously suggested applicability of multiple-shooting methods shall be explored in the first place.

The next set of recommendations stems from the limitations of the adopted methodology. Computationally heavy dynamical models, in particular the PDM, effectively hinder the ability to explore the problem using a high-fidelity analysis. It is deemed that:

1. *More families of periodic orbits shall be sought*

   The set of periodic orbits investigated in this research, excluding the grid search studies, focused on closed orbits symmetric with respect to the xz-plane of the synodic frame $\mathscr{F}$ in the CR3BP. There exists a range of families of non-symmetric periodic orbits (around equilibrium points and the asteroids), which shall be continued into ABP solutions as a continuation of this research.

2. *More initial conditions of the Didymos system shall be accounted for in the analysis*

   In this study, only 4 initial conditions for the angular positions of the Sun and Didymos were taken into account, resulting in 16 combinations of initial conditions for the system. This number shall be increased in future studies in order to investigate solutions for the unstudied initial conditions of the system.

3. *Weighing factors shall be applied in the temporary capture analysis.*

   In the presented study, the capture error was calculated as a sum of the errors in state vector $\mathbf{x}$, in Didymos's orientation Λ, and in the Sun's position ϕ. Exploration of the Pareto front of solutions by analyzing the sensitivity of the solutions to the three components to the overall objective function score of individuals (combinations of levitation and orbit trajectories) may provide valuable insights into other optimal solutions to the problem. Nevertheless, given the importance of the periodicity, the large contribution of Λ and ϕ acts in favor of the intended constraints.

4. *Only a tightly restricted set of initial conditions shall be considered for the grid search to limit the computational effort.*

   The grid search analysis was conducted with the objective of exploring a wide range of initial conditions for the two types of orbits. As seen in the work, the grid search analysis (although very heavy computationally) has not provided insights into the topology of solutions - the gradients have not been visible. Therefore, a much more refined, localized, and even targeted study shall be conducted in the regions of motion characterized by similar values of constants of motion as the particles levitating from the primary body to maximize the chances of identifying temporary capture trajectories. The specific metric (preferably, a constant of motion) to be used must be researched due to the non-Hamiltonian nature of the system under analysis, which renders Hamiltonian, Lagrangian, or Jacobi constants inapplicable.

The significant uncertainties associated with the current knowledge on the Didymos system translate to a large uncertainty of the results. Therefore:

1. *The study shall be performed again upon the availability of more precise properties of the Didymos system*

   The properties of the primaries and the system as a whole bear large uncertainties. Therefore, the analysis presented in this report shall be repeated on the system when more precise data is available.

2. *A sensitivity analysis shall be conducted to assess the dependency of the results on the uncertainties in the physical properties of the binary*

   The large uncertainties signify that the physical properties of the system may be well off the nominal values. Therefore, a sensitivity analysis is necessary to evaluate the dependence of the results on the variation of the physical properties of the system within the ranges of uncertainty. The physical properties under analysis shall be at least but not limited to: the semiaxes of the ellipsoids, the densities of the primaries, and the rotation rate of the primary.

3. *A detailed study shall be conducted to investigate the mechanics of the dusk disks of the Didymos system.*

   Further research is suggested to focus on studying the phenomena involved in the mechanisms of depletion and replenishment of the dust disk material as well as the bulk properties of these structures.

3.2.1. Implications

The results obtained in the discussed study may have implications on current and future research in the following areas:

1. *Operations planning for the Hera spacecraft*

   Since the problem at hand considers a general topic of motion of dust particles in binary asteroid systems applied to the example of Didymos, the results of computations presented in the journal paper may be directly applied as input data for planning operations of the Hera spacecraft in the binary system.

2. *Research on dust dynamics*

   The methodology outlined and used in the journal paper combines several approaches used in the literature to conduct research in the field of dust dynamics. However, due to the demonstrated successful application of these methods in a larger framework of the determination of fates of levitated particles, an end-to-end analysis might be performed that in result characterises the dust environment around rapidly rotating bodies in complex dynamical fields. The approach presented in the journal paper is deemed sufficiently generic to be successfully applied to analysis of multi-body systems, e.g., triple or quadruple asteroids.

3. *Single-shooting methods applied to topology analysis of highly-nonlinear dynamical systems*

The failure to apply single-shooting methods for local optimization of solutions in the grid search analysis may be a valuable input to future research planning, as it gives a clear warning regarding the nature of certain methods and their application in the analysis of non-autonomous dynamical systems. The conclusions drawn from the presented study may be useful in planning of other investigations.

4. *Grid search methods applied to topology analysis of highly-nonlinear dynamical systems*

   Although computationally heavy, the grid search method proved to be a viable and safe to use first-order analysis tool in a study of such highly-nonlinear problem as the one at hand. Further use of this method to study problems of similar characteristics may be facilitated by the presented research.

A

Verification and validation

This appendix presents a summary of tests performed to assure validity of the dynamical model and the employed numerical integration scheme.

A.1. Dynamical model

In this thesis research, a hybrid verification-validation approach was adopted. The validity cannot be assessed with respect to the true physical system, i.e., the Didymos system, because the necessary data from observations does not exist. Therefore, the verification and validation processes were performed jointly; the dynamical models are verified using results presented in peer-reviewed publications or tabulated data from well-established books that involve corresponding models, whereas the validity was affirmed by assumed analogy.

The dynamical model can be regarded as a series of augmentations to the fundamental circular-restricted three-body problem. Therefore, the verification tests focused first on confirming soundness of the sub-models (CR3BP, SBCR3BP, BP, ABP without the eclipse model, ABP). Then, the sub-models were combined into the dynamical model's and the sub-model tests were performed on this final implementation.

A.1.1. Circular-Restricted Three-Body Problem

The implementation of the CR3BP was verified by verifying the constant of motion - the Jacobi integral defined as a function of the effective potential of the CR3BP U_{CR3BP} and velocity components $\dot{x}$, $\dot{y}$, and $\dot{z}$ defined in $\mathscr{F}$ (see Section III in Chapter 2) [25]

$$C = 2U_{CR3BP} - (\dot{x}^2 + \dot{y}^2 + \dot{z}^2) \ . \tag{A.1}$$

Verification of the equations of motion was conducted in two steps. First, accelerations given by the equations of motion were verified to be null at the equilibrium points of the CR3BP, as tabulated in [25]. Second, trajectories presented by [11] were reproduced for known initial conditions in high-sensitivity, sub-bifurcation cases of the CR3BP, i.e., for mass parameters of the CR3BP [25] $\mu = 0.499$ and $\mu = 0.501$. Equilibrium points are locations in $\mathscr{F}$ in the CR3BP, in which the net acceleration experienced by a test particle is zero and hence resulting in theoretical infinite rest in said point. Table A.1 shows that the equations of motion are correct for the equilibrium points due to null acceleration in $\mathscr{F}$ (numerical error is neglected). Furthermore, the equations also hold to reproduce results obtained by [11] (see Figure A.1), which verifies the implementation of the equations of motion outside the equilibrium points.

Based on the fact that the Jacobi integral is the CR3BP's constant of motion and the verified equations of motion for this sub-model, a verification case was formulated; the state histories of the trajectories presented in fig. A.1 were analyzed for variation in the Jacobi integral over time. Data presented in fig. A.2 verifies of the Jacobi integral implementation, as the variation from the initial value of the constant of motion is small ($\approx 10^{-9}$).

A.1.2. Shape-based three-body problem

The verification process of the shape-based three-body problem (SB3BP) sub-model comprises verification of three intermediate sub-models leading to verification of the SB3BP: (1) a single uniformly rotating ellip-

Table A.1 Verification of calculated collinear Lagrange points (differences of the x-coordinate in $\mathscr{F}$ (Δx-coord.) were calculated with respect to the data in Appendices I-III of Chapter 4 in [25])

	L_1	L_2	L_3
$\mu = 0.5$			
Calculated (x-coord.)	0.0000000000	1.1984061446	-1.1984061446
Difference (Δx-coord.)	0.0000000000	0.0000000000	0.0000000000
Acceleration in $\mathscr{F}$ ($\|\ddot{\mathbf{r}}\|$)	1.83186799e-13	4.22328838e-13	4.44089209e-16
$\mu = 0.1$			
Calculated (x-coord.)	0.6090351100	1.2596998329	-1.0416089086
Difference (Δx-coord.)	0.0000000000	0.0000000000	0.0000000000
Acceleration in $\mathscr{F}$ ($\|\ddot{\mathbf{r}}\|$)	1.11022302e-15	2.22044604e-16	4.61436444e-16
$\mu = 0.01$			
Calculated (x-coord.)	0.8480787130	1.1467650421	-1.0041666120
Difference (Δx-coord.)	0.0000000000	0.0000000000	0.0000000000
Acceleration in $\mathscr{F}$ ($\|\ddot{\mathbf{r}}\|$)	1.66533453e-16	2.82551759e-14	1.88651178e-16
$\mu = 0.001$			
Calculated (x-coord.)	0.9312869755	1.0699160980	-1.0004166666
Difference (Δx-coord.)	0.0000000000	0.0000000000	0.0000000000
Acceleration in $\mathscr{F}$ ($\|\ddot{\mathbf{r}}\|$)	2.13801198e-13	2.22044604e-16	3.58274607e-16
$\mu = 10^{-4}$			
Calculated (x-coord.)	0.9680652061	1.0324251917	-1.0000416667
Difference (Δx-coord.)	0.0000000000	0.0000000000	0.0000000000
Acceleration in $\mathscr{F}$ ($\|\ddot{\mathbf{r}}\|$)	1.72084568e-15	8.88178419e-16	1.67238185e-17
$\mu = 10^{-5}$			
Calculated (x-coord.)	0.9851267004	1.0150020578	-1.0000041667
Difference (Δx-coord.)	0.0000000000	0.0000000000	0.0000000000
Acceleration in $\mathscr{F}$ ($\|\ddot{\mathbf{r}}\|$)	5.43898259e-13	1.54730395e-13	4.62175057e-17
$\mu = 10^{-6}$			
Calculated (x-coord.)	0.9930814476	1.0069486021	-1.0000004167
Difference (Δx-coord.)	0.0000000000	0.0000000000	0.0000000000
Acceleration in $\mathscr{F}$ ($\|\ddot{\mathbf{r}}\|$)	2.94902990e-16	1.38777878e-17	8.48528489e-17

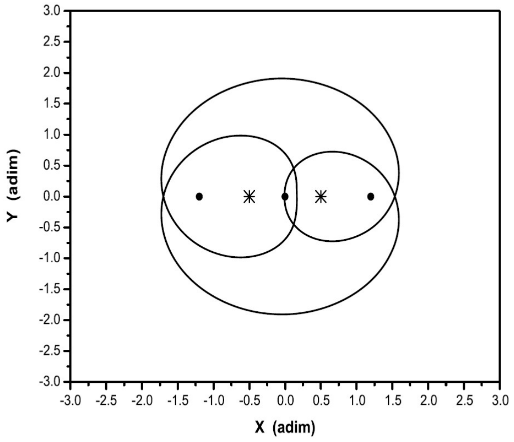

(a) Planar Lyapunov Orbit around L_1 (Fig. 13 in [11])

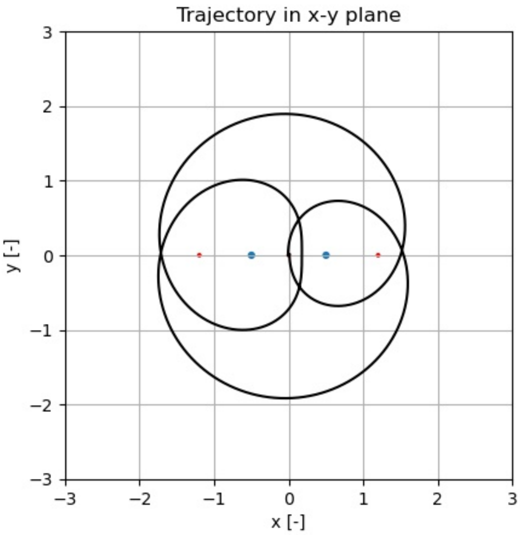

(b) Reproduction of the Planar Lyapunov Orbit from Fig. A.1a

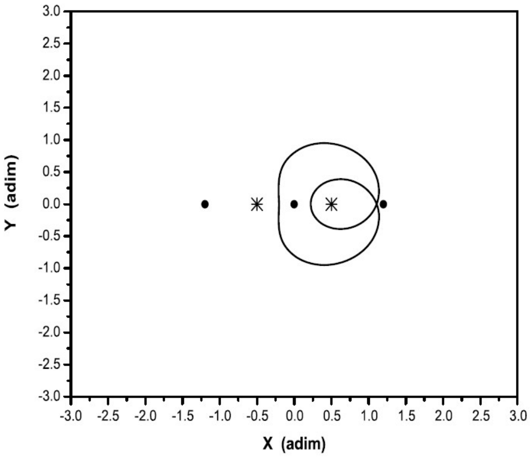

(c) Planar Lyapunov Orbit around L_1 (Fig. 13 in [11])

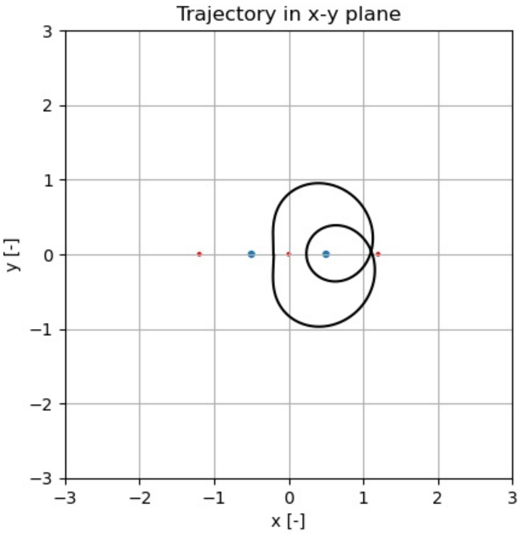

(d) Reproduction of the Planar Lyapunov Orbit from Fig. A.1c

Figure A.1 Reproduction of selected Planar Lyapunov Orbits given in [11]

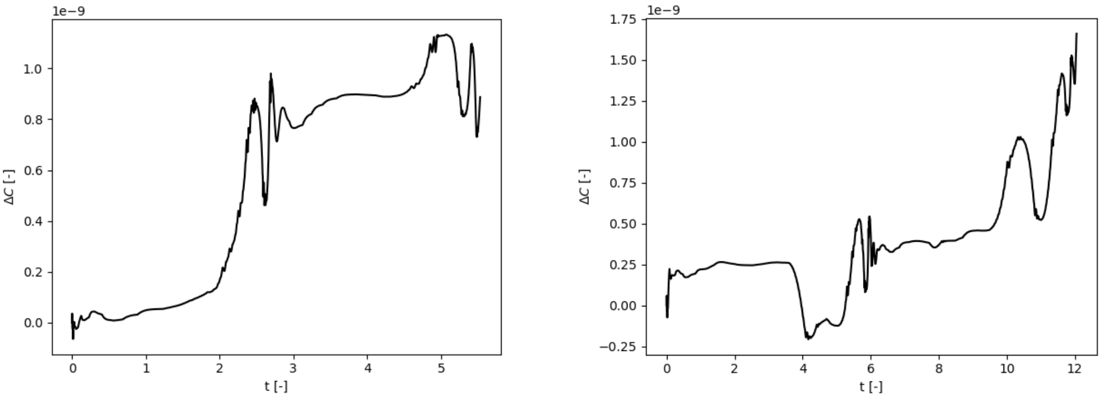

(a) Variation in the Jacobi integral throughout the trajectory presented in fig. A.1b with respect to the initial value

(b) Variation in the Jacobi integral the trajectory presented in fig. A.1d with respect to the initial value

Figure A.2 Variation in the Jacobi integral the trajectories presented in Fig. A.1 with respect to the initial values

Table A.2 Verification of the gravity model of a single, uniformly rotating ellipsoid in the synodic reference frame

$\mathbf{r}$	$\ddot{\mathbf{r}}_{\mathbf{calc}}$	$\lVert\ddot{\mathbf{r}}_{\mathbf{ref}} - \ddot{\mathbf{r}}_{\mathbf{calc}}\rVert$
$[0.5\ 0\ 0]^T$	$[-3.57813008\ 0\ 0]^T$	$8.34584935 \times 10^{-16}$
$[0.5\ 0.5\ 0]^T$	$[-0.92214548\ -0.92684921\ 0.]^T$	$5.05430021 \times 10^{-16}$
$[-0.5\ -0.5\ 0]^T$	$[0.92214548\ 0.92684921\ 0.]^T$	$6.39180238 \times 10^{-16}$
$[0.5\ 0.5\ 0.5]^T$	$[-0.26645899\ -0.26816592\ -0.77477617]^T$	$9.54893011 \times 10^{-16}$
$[-0.5\ 0.5\ -0.5]^T$	$[0.26645899\ -0.26816592\ 0.77477617]^T$	$9.02839821 \times 10^{-16}$
$[5\ -5\ 5]^T$	$[4.99230233\ -4.99230216\ -0.0076985]^T$	$8.43983291 \times 10^{-16}$

soid in a synodic reference frame, (2) two tidally locked ellipsoids in a synodic reference frame $\mathscr{F}$, and (3) semi-asynchronous system of two ellipsoids in a synodic reference frame $\mathscr{F}$. Performing intermediate verification is necessary due to lack of verification data for the full SB3BP sub-model; therefore, this three-step verification process is introduced to gradually verify the additions of complexity to the sub-model. Verification of each intermediate sub-model involves analogous steps as were performed for the implementation of the CR3BP, i.e., verification of the equations of motion and the effective potential. The implementation of the second-order derivatives of the effective potential is verified only for the full SB3BP sub-model, i.e., the semi-asynchronous system of two ellipsoids in a synodic reference frame. The gravitational fields of the ellipsoids are modeled using the spherical harmonics (SH) model of degree and order 2, since the dynamical model used in this work employs only the C_{20} and C_{22} terms of the expansion. Moreover, the SB3BP is verified based on the verification of the CR3BP sub-model.

Single uniformly rotating ellipsoid in a synodic reference frame

The first intermediate model is a single ellipsoid which rotates uniformly along one of its principal axes, i.e., any gyroscopic effects in this angular motion are neglected. The equations of motion are defined in the synodic reference frame fixed to the ellipsoid - the coordinate system axes align with the ellipsoid's semi-axes, where the z-axis is parallel to the rotation vector of the ellipsoid. The inertial effects exerted on the particle are assumed verified, as the implementation of the sub-model was performed through adjustment of the CR3BP implementation by substitution of the primary's point-mass gravity field model with a SH model (Didymos' geometry and uniform mass distribution were assumed) and assuming $\mu = 0$. The implementation was verified against results obtained from the following mathematical formulation given by Wakker [27] (eq. 20.6)

$$\nabla U_{M_D,ref} = -\frac{3}{2}\mu C_{2,0}\frac{R^2}{r^5}\begin{bmatrix} x\left(1-5\dfrac{z^2}{r^2}\right) \\ y\left(1-5\dfrac{z^2}{r^2}\right) \\ z\left(3-5\dfrac{z^2}{r^2}\right) \end{bmatrix}, \tag{A.2}$$

where $U_{M_{D,ref}}$ is the spherical-harmonic gravitational potential of Didymos of order 2 and degree 0, $C_{2,0}$ is the Stokes coefficient of order 2 and degree 0, x, y, z are dimensionless coordinates in $\mathscr{F}$, and $r = \sqrt{x^2+y^2+z^2}$. The implementation was found correct for the set of defined test cases (see Table A.2), where $\ddot{\mathbf{r}}_{\mathbf{ref}}$ and $\ddot{\mathbf{r}}_{\mathbf{calc}}$ stand for the reference (calculated with the primary's acceleration given by Equation A.2, i.e., $\ddot{\mathbf{r}}_{\mathbf{ref}} = \nabla U_{M_D,ref}$) and the calculated (obtained by the relations described in chapter 2) values of acceleration in $\mathscr{F}$ (Equation (5)).

Two tidally locked ellipsoids in a synodic reference frame

This intermediate model is an augmentation of the CR3BP by substituting the primaries with two ellip-

Table A.3 Juxtaposition of the SRP acceleration values obtained from the implemented model and found in the literature

Distance	**Calculated SRP**	**Reference SRP**	**Source**
1.015 AU (Earth-Sun on June 20th)	$4.417807365 \times 10^{-8}$ [Nm^{-2}]	$\approx 4.418 \times 10^{-8}$ [Nm^{-2}]	[15]

soids. The new primaries are tidally locked, therefore their orientation is fixed in $\mathscr{F}$. The axes of rotation coincide with the principal axes for both ellipsoids, which again nullifies all gyroscopic effects. Since the dynamical model is conservative, a constant of motion can be defined for the system as

$$C_{SB3BP,syn}(\mathbf{x}) = 2U_{SB3BP} - V^2\,, \tag{A.3}$$

where the effective potential of the SB3BP in the synodic frame $\mathscr{F}$ is U_{SB3BP} at the angular velocity of the primary body's rotation $\dot{\Lambda}_1 = 0$ and the latter term is the squared magnitude of the velocity vector in $\mathscr{F}$, i.e., $V^2 = \dot{x}^2 + \dot{y}^2 + \dot{z}^2$. Conservation of the Jacobi integral over time was examined for three selected trajectories (see figure A.3). Verification of the sub-model implementation is demonstrated by the negligible variation in the constant of motion throughout the propagated trajectories with respect to the initial value. The trajectories were selected to represent different regimes of motion: Figure A.3b concerns on generic motion in the binary system, Figure A.3d focuses on motion in the proximity to a stable equilibrium point on the example of the L$_4$, and Figure A.3f shows motion around an unstable equilibrium point on the example of L$_1$.

Semi-asynchronous system of two ellipsoids in a synodic reference frame

This step of the SB3BP verification comprises of verifying the implementation of the uniform rotation of the primary body in $\mathscr{F}$. The function of orientation of the primary body Λ in $\mathscr{F}$ over time was verified by plotting it (see $\Lambda(t)$ in Figure A.4). The conversion between the Cartesian and spherical coordinates of the body-fixed frame $\mathscr{F}_{D/d}$ used for calculation of accelerations in the ABP and proximity dynamical model (PDM) models were performed using a well-established Astropy package [4] and are assumed to be valid.

A.1.3. Bicircular problem

The effective potential in the bicircular problem (BP) is a function of time, i.e., the Jacobi integral is no longer a constant of motion. Therefore, a simple test like conservation of a constant quantity cannot be used to verify the BP implementation.

The sub-model was verified by reproducing results presented in [19]. A trajectory originating from the $\mathscr{F}_S$ coordinates of the L$_4$ point in the CR3BP is presented in figure A.5 (of interest is the trajectory marked in blue and labelled as 'Bin', which stands for 'Binary case'), whereas the verification results are given in figure A.6.

A.1.4. Solar radiation pressure

The solar radiation pressure (SRP) implementation was verified only for the dimensional value of the acceleration. This was achieved by performing a unit test of the function calculating the magnitude of the SRP acceleration and compared against a value found in the literature (see Table A.3). The direction of the SRP acceleration vector was verified to be parallel and opposite to the acceleration vector of the third-body effect, which is already verified in the BP (see section A.1.3).

A.1.5. Eclipse model

Verification of the eclipse model was conducted by unit-testing elementary functions (calculation of the ellipsoid radius $R_{ell}(\lambda, \delta)$ for a given set of semi-axes a, b, c, computation of the projected ellipsoid radius $R_\eta(...)$) and visual inspection of the effective coefficient calculated for a number of test cases (several arbitrarily selected examples are presented in figure A.7).

A.1.6. Augmented bicircular problem

The verification of the assembled dynamical model was achieved by performing all the sub-model verification tests once again on the assembled implementation. Hence, the complete dynamical model can be used as any of the sub-models as well as a combination of them. To the best knowledge of the author, the literature does not provide any verification data for such a formulation of the augmented bicircular problem. There-

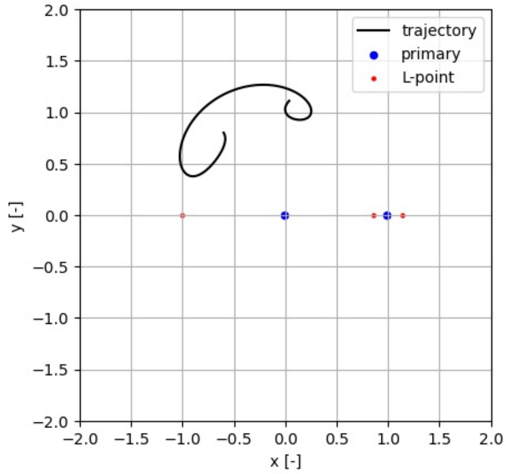

(a) Propagated trajectory from arbitrarily selected initial state vector (x-y plane)

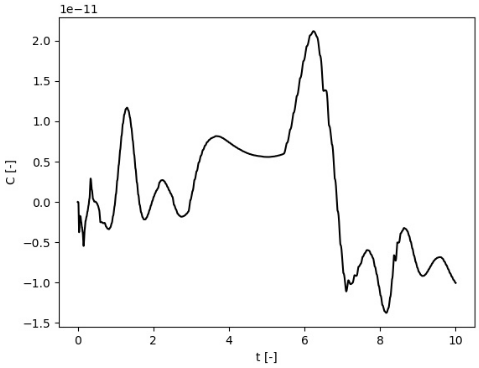

(b) Variation of the Jacobian C throughout the motion depicted in A.3a

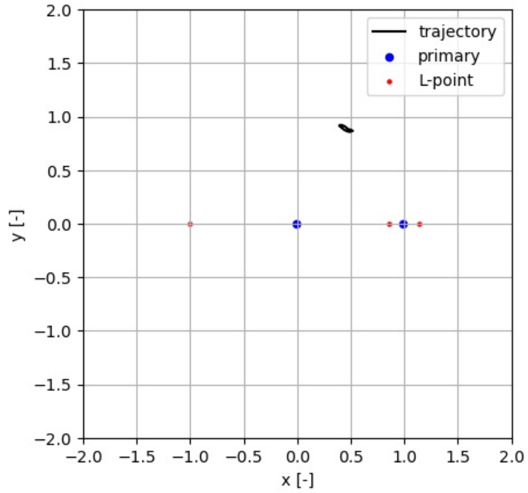

(c) Trajectory in the vicinity of L_4 (x-y plane)

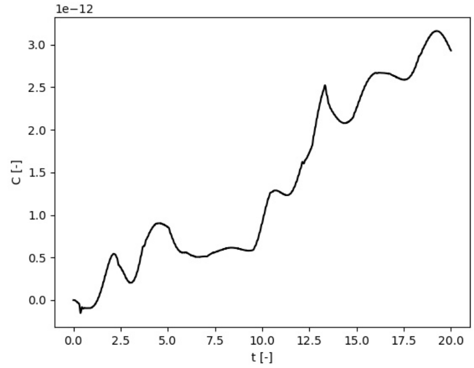

(d) Variation of the Jacobian C throughout the motion depicted in A.3c

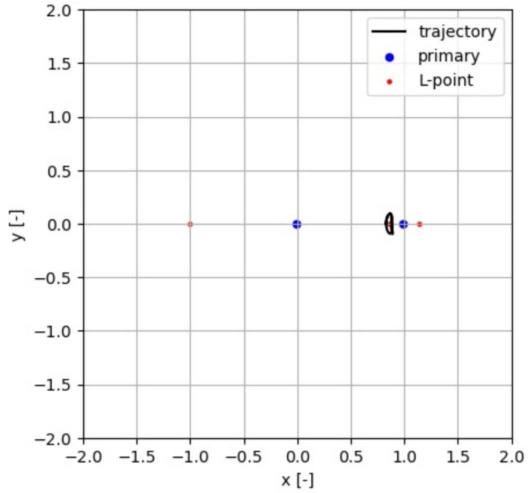

(e) Trajectory in the vicinity of L_1 (x-y plane)

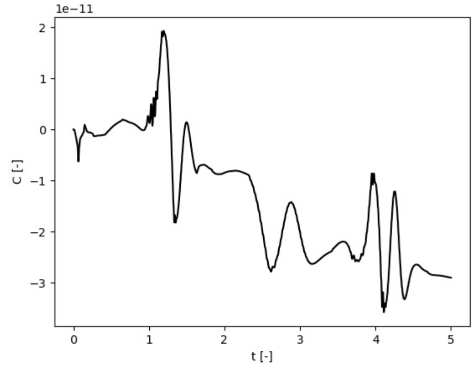

(f) Variation of the Jacobian C throughout the motion depicted in A.3e

Figure A.3 Three trajectory cases propagated using the SB3BP model and analysis of the variation in the Jacobian

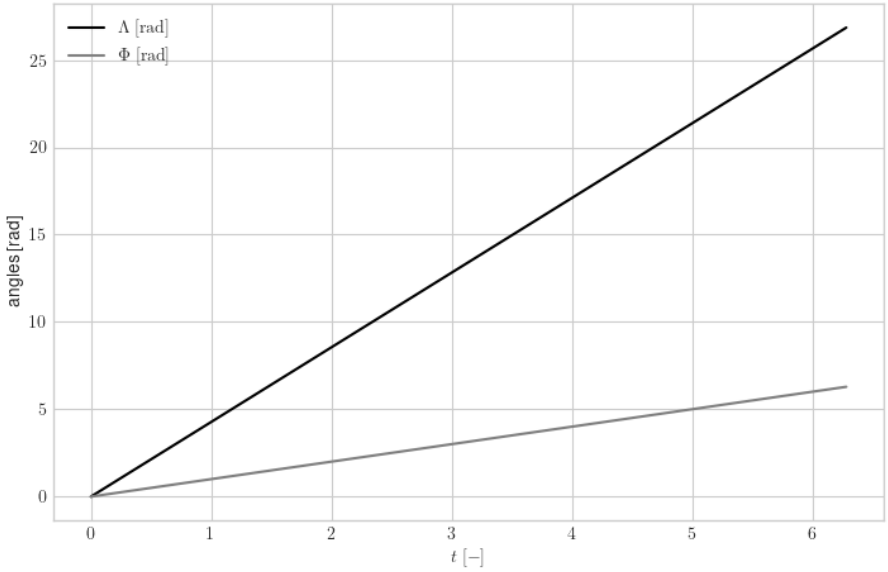

Figure A.4 Position of the Sun ϕ and orientation of the primary Λ over time, when $\phi(t=0) = \Lambda(t=0) = 0$

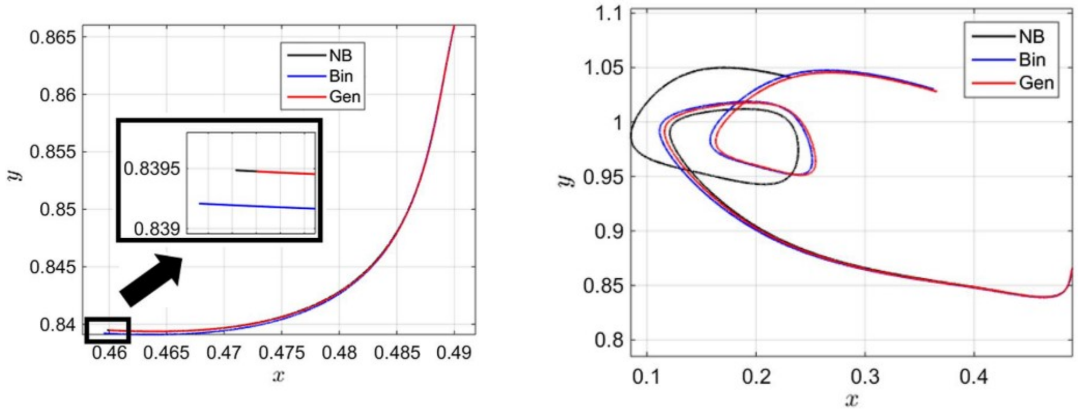

(a) Trajectory for propagation time $t_f = \pi/2$

(b) Trajectory for propagation time $t_f = 4\pi$

Figure A.5 Trajectories of a particle departing from equilibrium in the L$_4$ Lagrangian point corresponding to the CR3BP, $\theta_S(t=0) = 0$, $\mu = 1e-2$, $\mu = 1e-2$, $r_3 = 0.42$ (Fig. 4 in [19])

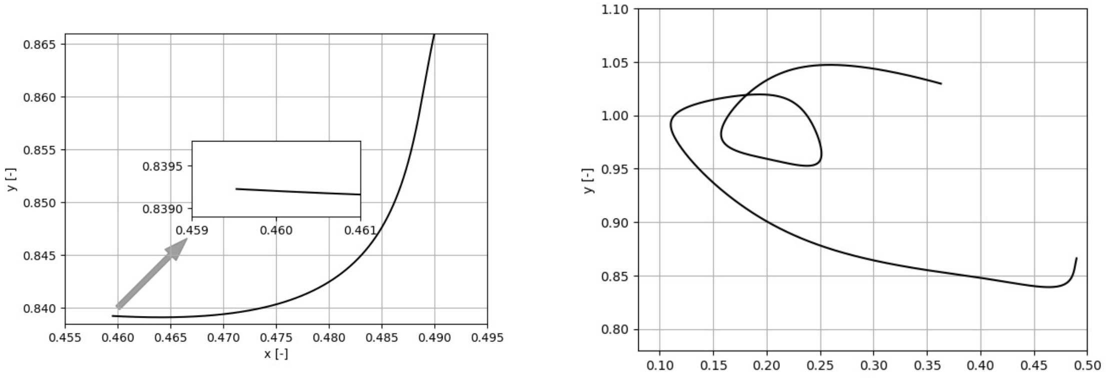

(a) Reproduction of the trajectory from Fig. A.5a

(b) Reproduction of the trajectory from Fig. A.5b

Figure A.6 Reproduction of trajectories from Fig. A.5

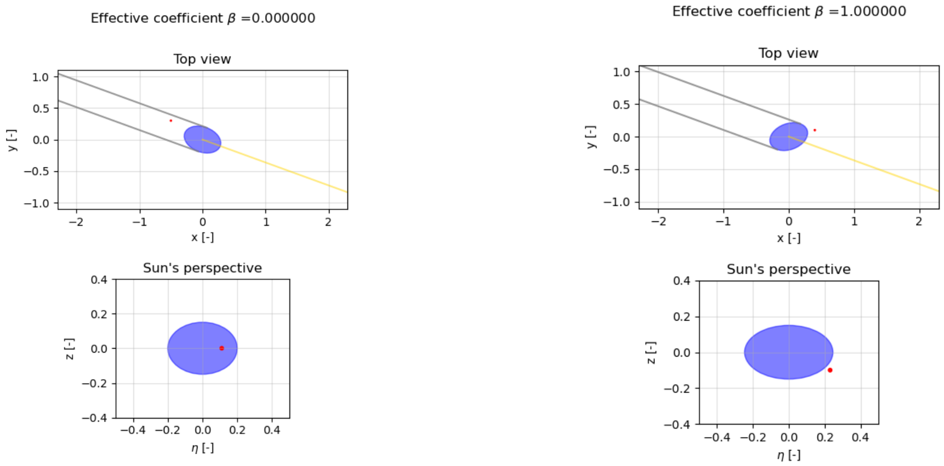

(a) Simple case 1 - no shade

(b) Simple case 2 - full shade

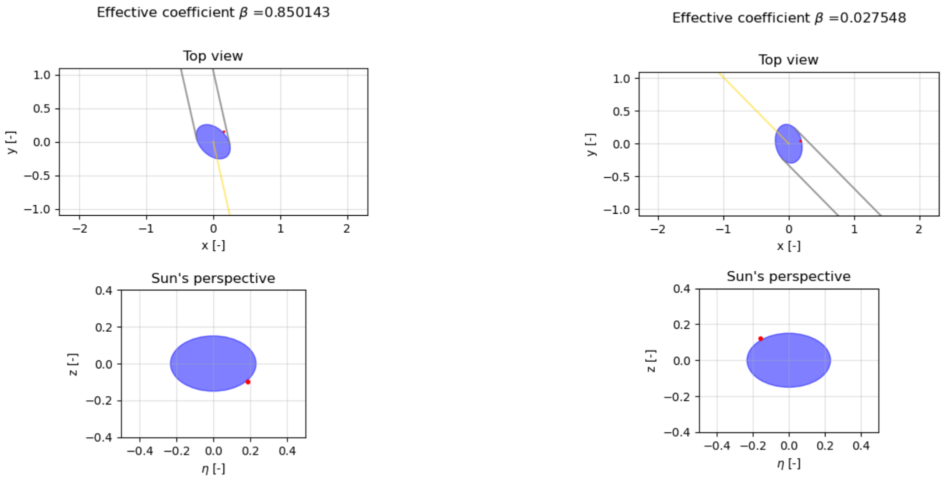

(c) Partial shade 1

(d) Partial shade 2

Figure A.7 Selection of four cases for visual verification of the effective coefficient for a single body; the golden line joins the center of the body and the radiative third body, the grey lines mark boundaries of shaded area in the x-y plane, the red point indicates the test particle's position, and η is one of coordinates of the system defined by rotation of the (x, y, z) coordinate system around z such that η is perpendicular to the Sun-Didymos vector

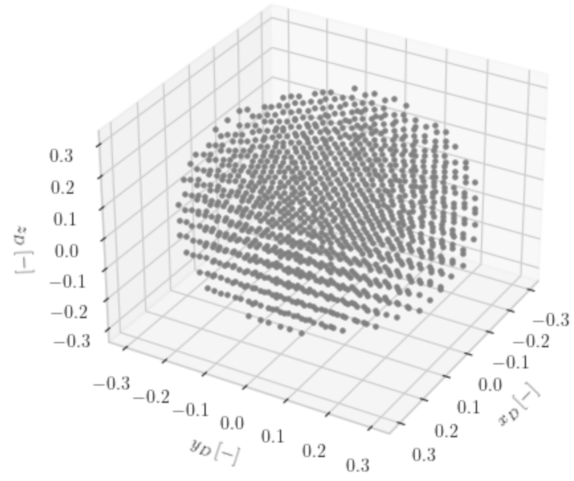

Figure A.8 Simplified graphical representation of the MC model - 1200 selected mass concentrations in the primary-fixed frame

fore, successful completion of the sub-model tests was considered a sufficient condition for confirmation of verification.

A.1.7. Verification and calibration of the mass-concentration model

Verification of the mass-concentration (MC) model of a single body was conducted in an inertial reference frame through a discretization of a uniform-density sphere of radius $R_{test} = 1$ and mass $M_{test} = 1$, whose center of mass coincides with the origin of the frame. A selection of 10 position vectors outside the defined sphere was used to assess the error of the gravity potential and the acceleration of the MC model with respect to the analytical values for the test sphere, i.e.,

$$U_{test} = \frac{M_{test}}{r_D}, \tag{A.4}$$

$$\ddot{\mathbf{r}}_D = \nabla U_{test}, \tag{A.5}$$

where U_{test} and r_D are the gravitational potential of the sphere and the test particle's distance from the geometrical center of the sphere. The results are presented in Table A.4, where the columns give, respectively, the position vector, its norm (i.e., the scalar distance), and the third two is the relative errors of the mascon-derived acceleration vector (the fourth column is discussed below). It was observed that the relative error depends not only on the number of mass concentrations, but also on the position around the body - at certain positions, the errors were orders of magnitude larger than in other locations. This phenomenon is interpreted as a result of the discretization into a finite number of elements N, which renders N singularities. If U_{test} or $\ddot{r}_D$ are calculated close to such singularities (some of them are located on the sphere), absolute values of accelerations are found to be much larger than analytical values for a sphere. This phenomenon was found to be caused by the proximity of the test position $\mathbf{r}_D$ to one of the N singularities. To cope with this shortcoming of the MC model, an offset is introduced. The offset ξ is defined as a relative reduction of an ellipsoid semiaxes a, b, and c to produce the effective ellipsoid of semiaxes $(1-\xi)a$, $(1-\xi)b$, and $(1-\xi)c$, respectively (results presented in the last column of Table A.4 concern a mascon model with an offset of 0.001). The results of the test cases demonstrated significant improvement in accuracy and consistency, as shown in fig. A.9, which presents the dependence of the model error, i.e., the discrepancy between the mascon model-derived acceleration vector with respect to the analytical value for the test sphere, and the settings of the model, i.e., the mesh grid size Π and the offset ξ. The mesh grid size Π is defined as the distance between the two closest mass concentrations in the cuboidal mesh. However, to find an optimal setting for the PDM model, a sensitivity analysis was conducted; by means of iteratively localized grid searches, the combination of grid size

Table A.4 Verification of the mascon model through juxtaposition of calculated acceleration vectors for a selection of test cases and their analytical values or a $N = 4.18 \times 10^6$ model

$\mathbf{r_D}$	$\lVert\mathbf{r_D}\rVert$	$\dfrac{\left\lVert\ddot{\mathbf{r}}_{\mathbf{D,an}} - \ddot{\mathbf{r}}_{\mathbf{D,num}}\right\rVert}{\left\lVert\ddot{\mathbf{r}}_{\mathbf{D,an}}\right\rVert}$	$\dfrac{\left\lVert\ddot{\mathbf{r}}_{\mathbf{D,an}} - \ddot{\mathbf{r}}_{\mathbf{D,num,offset}}\right\rVert}{\left\lVert\ddot{\mathbf{r}}_{\mathbf{D,an,offset}}\right\rVert}$
$[1.0001, 0, 0]^T$	1.0001	23.876	$7.021 \times 10-3$
$[1.001, 0, 0,]^T$	1.001	2.323×10^{-1}	6.946×10^{-3}
$[1.01, 0, 0]^T$	1.01	3.443×10^{-3}	5.879×10^{-3}
$[1.1, 0, 0]^T$	1.1	1.174×10^{-3}	1.202×10^{-3}
$[1, 1, 0]^T$	1.414	3.437×10^{-5}	3.469×10^{-5}
$[1, 1, 1]^T$	1.732	2.273×10^{-6}	2.055×10^{-6}
$[5, 5, 5]^T$	8.660	1.261×10^{-8}	1.310×10^{-8}

and offset were selected to be $\Pi = 3.5 \times 10^{-3}$ and $\xi = 0.001$. The selection was done based on two criteria: (1) allowable error of $\epsilon_{BS} = 1\%$, i.e., the normalized largest discrepancy between the analytically-obtained and the model-derived acceleration values, and (2) the maximum execution time for a single computation of the acceleration $t_{exec} < 5$ s.

A.2. Integration

Validation of numerical integration tools applied to the physical problem at hand was assured by (1) the use of SciPy - a scientific tool package that offers a selection of implemented numerical integration schemes - and (2) the trajectories recreated by means of numerical integration of pre-validated equations of motion (see A.1). In addition, the discussion given in Appendix B, in particular the plots depicting the numerical error accumulated in the numerical integration (see Figure B.2), strongly indicate at validity of the employed numerical integration tools.

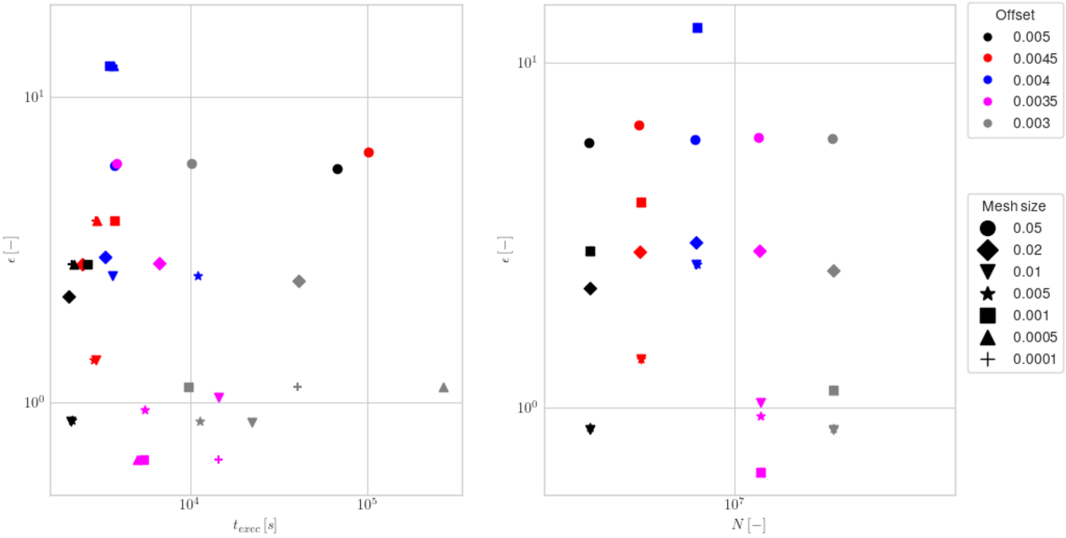

Figure A.9 Calibration of the mascon model

B

Integrator selection

The selection of a numerical integration scheme to be used in this work was done among a selection of pre-validated methods available in the open-source library `SciPy` [13] (see Table B.1).

Table B.1 Selection of methods available in the `SciPy` package [13]

Abbreviation	**Integration method**
RK45	Explicit Runge-Kutta method of order 5(4)
DoPri853	Explicit Runge-Kutta method of order 8
Radau	Implicit Runge-Kutta method of the Radau IIA family of order 5
BDF	Implicit multi-step variable-order Backward-Differentiation Formula
LSODA	Adams/BDF method with automatic stiffness detection and switching

The numerical integration scheme (for short referred to as 'the integrator') was selected through analyzing the behavior of several methods in four test cases (see Table B.2) depicted in fig. B.1. The test cases were designed with the purpose of representing various regimes of motion of the particle within the binary system modeled as two tidally locked ellipsoids in a synodic reference frame and are presented in fig. B.1. In the process of integrator selection, the conservative dynamical model was analyzed to determine the top-performers for each test case among the integrators considered. Next, the most accurate scheme was used to produce a benchmark trajectory for each of the cases, which was then used to assess the relative accuracy of other integrators in the complete (non-conservative) dynamical model of the bicircular problem.

Table B.2 Four cases of motion regime

Case	**Regime of motion**	**Trajectory plot**
1	Motion far from the primaries	Fig. B.1a
2	Motion around L_4	Fig. B.1b
3	Motion in the vicinity to the Brillouin sphere	Fig. B.1c
4	Motion around L_1	Fig. B.1d

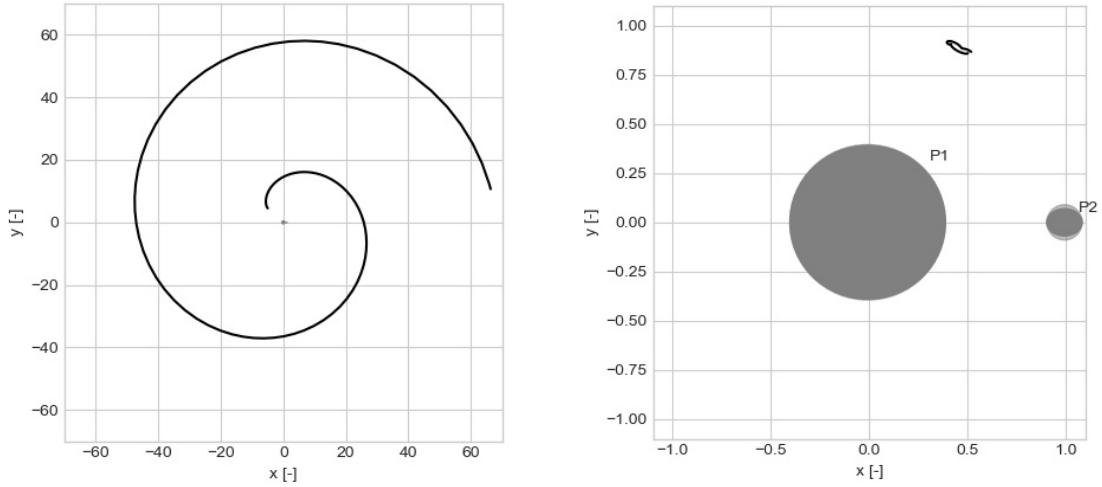

(a) Case 1 - motion far from the primaries

(b) Case 2 - motion around L_4

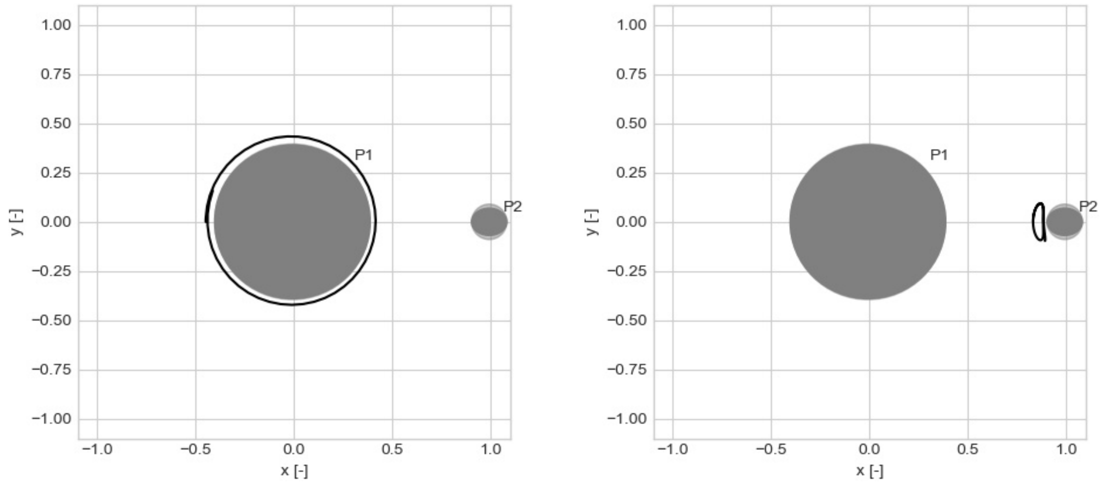

(c) Case 3 - motion in the vicinity to the Brillouin sphere

(d) Case 4 - motion around L_1

Figure B.1 Selection of the integration scheme - four cases of motion regime

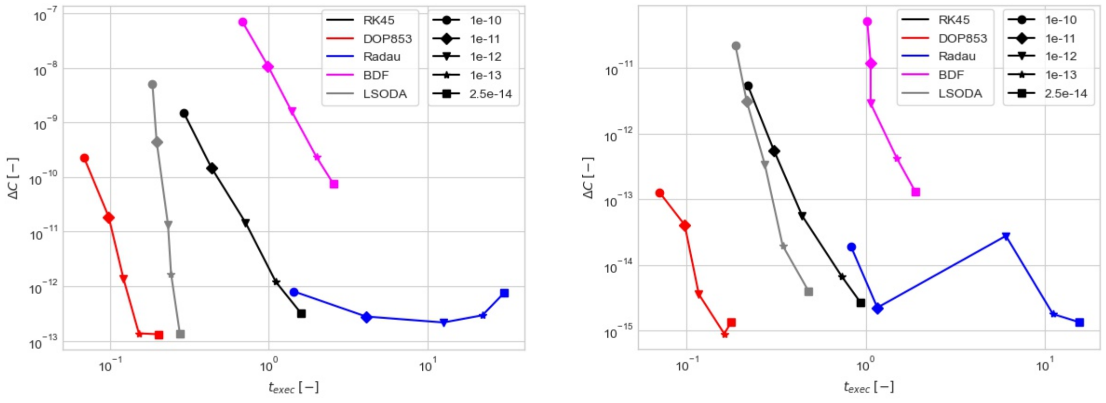

(a) Case 1 - motion far from the primaries

(b) Case 2 - motion around L_4

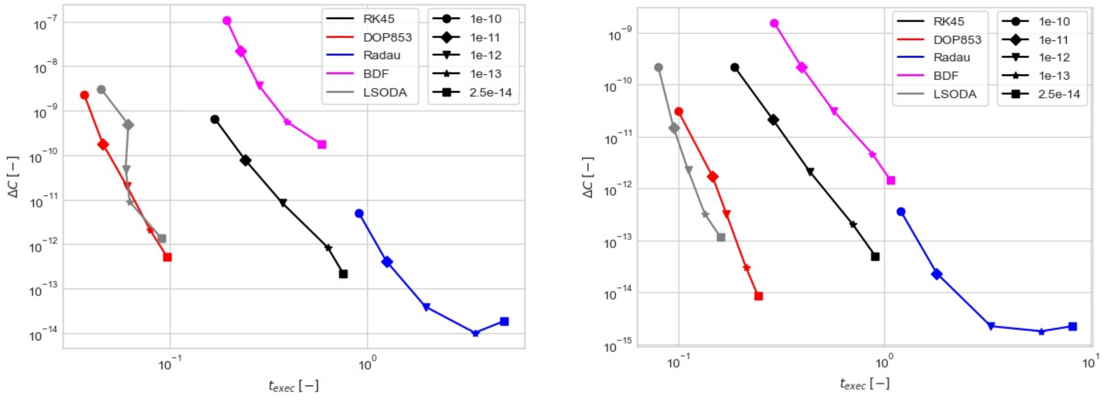

(c) Case 3 - motion in the vicinity to the Brillouin sphere

(d) Case 4 - motion around L_1

Figure B.2 Performance analysis of integration schemes in a Hamiltonian system - four cases of motion regime

B.1. Benchmark integrator selection

The rationale for performing an intermediate analysis of integrator accuracy is the Hamiltonian nature of the model, i.e., existence of a constant of motion. The total numerical error was defined as the largest absolute difference between values of the Jacobi integral at the initial state vector C_0 and at any later state vector C_t

$$\Delta C = \max\left(\|C_0 - C_t\|\right) . \tag{B.1}$$

Performance of each numerical integration scheme was assessed for 5 different tolerance settings: 10^{-10}, 10^{-11}, 10^{-12}, 10^{-13}, and 2.5×10^{14}, where the influence of both relative and absolute tolerances was studied collectively. Hence, each test case of motion was propagated using 25 sets of integrator settings.

Results presented in fig. B.2 indicate that the DOP853 method renders the most accurate solutions for cases 1 and 2 (the smallest values of ΔC in fig. B.2a and B.2b, respectively), whereas the Radau scheme - for cases 3 and 4 (the smallest values of ΔC fig. B.2c and B.2d, respectively). Since the execution times of the DOP853 scheme show significant advantage over the Radau integrator, the DOP853 integration scheme with the tolerance of 2.5×10^{-14} was selected as a benchmark integration scheme.

B.2. Integration methods applied to the augmented bicircular problem

Selection of the integrator used to conduct research presented in chapter 2 was made based on the comparison of execution time and performance, i.e., the maximum euclidean norm of the difference between the state vectors in the state history of a benchmark solution $\mathbf{x}_b$ and the respective state vectors of the propagated trajectory under analysis $\mathbf{x}_t$ at any time t

$$\Delta\|\mathbf{x}\| = \max\left(\|\mathbf{x}_b(t) - \mathbf{x}_t(t)\|\right) . \tag{B.2}$$

The results of the analysis presented in fig. B.3 demonstrate great accuracy of RK45, DOP853, and Radau for all the test cases. Due to the volume of numerical computations in the study, the execution time is a

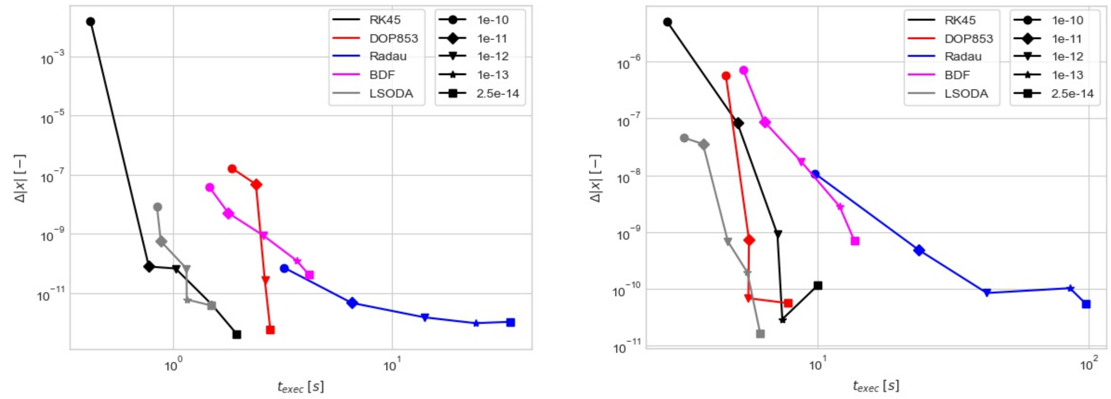

(a) Case 1 - motion far from the primaries

(b) Case 2 - motion around L_4

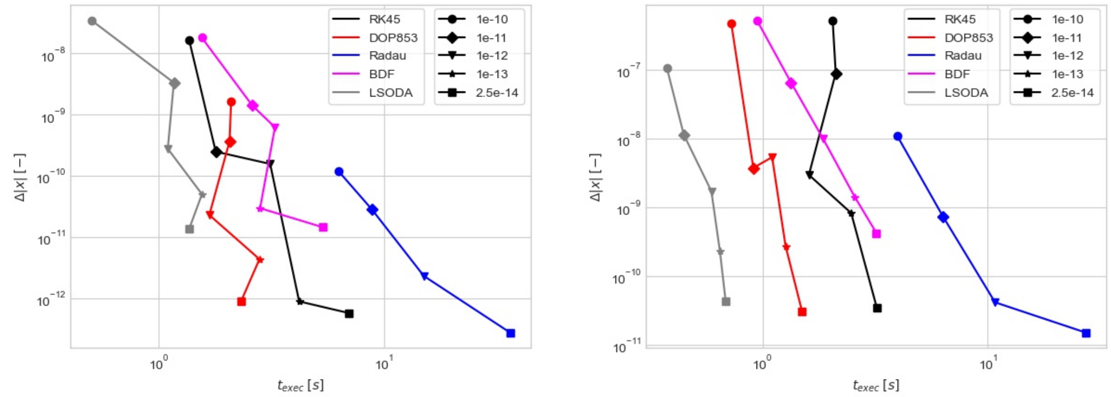

(c) Case 3 - motion in the vicinity to the Brillouin sphere

(d) Case 4 - motion around L_1

Figure B.3 Performance analysis of integration schemes in a non-Hamiltonian system - four cases of motion regime key factor in the selection process. Therefore, the DOP853 method with the absolute (`atol`) and relative tolerances (`rtol`) set to `atol=rtol=` 10^{-13} was chosen for the study in view of its remarkable accuracy and speed with respect to all other methods. The tolerance of 2.5×10^{-14} proved to be unstable in certain cases, which might be related to the level of precision native to the machine running the calculations.

Bibliography

[1] H Agrusa, D Richardson, A Davis, E Fahnestock, M Hirabayashi, N Chabot, A Cheng, A Rivkin, and P Michel. A benchmarking and sensitivity study of the full two-body gravitational dynamics of the DART mission target, binary asteroid 65803 Didymos. *Icarus*, 349(January), 2020.

[2] H Agrusa, K Tsiganis, I Gkolias, D Richardson, A Davis, E Fahnestock, and M Hirabayashi. On the post-impact spin state of the secondary component of the didymos-dimorphos binary asteroid system. In *AAS/Division for Planetary Sciences Meeting Abstracts*, volume 52, 2020.

[3] Applied Physics Laboratory, John Hopkins University. Double Asteroid Redirection Test, Mission Overview. URL `https://dart.jhuapl.edu`. Accessed: 20-11-2020.

[4] Astropy Collaboration, A. M. Price-Whelan, B. M. Sipőcz, H. M. Günther, P. L. Lim, S. M. Crawford, S. Conseil, D. L. Shupe, M. W. Craig, N. Dencheva, A. Ginsburg, J. T. Vand erPlas, L. D. Bradley, D. Pérez-Suárez, M. de Val-Borro, T. L. Aldcroft, K. L. Cruz, T. P. Robitaille, E. J. Tollerud, C. Ardelean, T. Babej, Y. P. Bach, M. Bachetti, A. V. Bakanov, S. P. Bamford, G. Barentsen, P. Barmby, A. Baumbach, K. L. Berry, F. Biscani, M. Boquien, K. A. Bostroem, L. G. Bouma, G. B. Brammer, E. M. Bray, H. Breytenbach, H. Buddelmeijer, D. J. Burke, G. Calderone, J. L. Cano Rodríguez, M. Cara, J. V. M. Cardoso, S. Cheedella, Y. Copin, L. Corrales, D. Crichton, D. D'Avella, C. Deil, É. Depagne, J. P. Dietrich, A. Donath, M. Droettboom, N. Earl, T. Erben, S. Fabbro, L. A. Ferreira, T. Finethy, R. T. Fox, L. H. Garrison, S. L. J. Gibbons, D. A. Goldstein, R. Gommers, J. P. Greco, P. Greenfield, A. M. Groener, F. Grollier, A. Hagen, P. Hirst, D. Homeier, A. J. Horton, G. Hosseinzadeh, L. Hu, J. S. Hunkeler, Ž. Ivezić, A. Jain, T. Jenness, G. Kanarek, S. Kendrew, N. S. Kern, W. E. Kerzendorf, A. Khvalko, J. King, D. Kirkby, A. M. Kulkarni, A. Kumar, A. Lee, D. Lenz, S. P. Littlefair, Z. Ma, D. M. Macleod, M. Mastropietro, C. McCully, S. Montagnac, B. M. Morris, M. Mueller, S. J. Mumford, D. Muna, N. A. Murphy, S. Nelson, G. H. Nguyen, J. P. Ninan, M. Nöthe, S. Ogaz, S. Oh, J. K. Parejko, N. Parley, S. Pascual, R. Patil, A. A. Patil, A. L. Plunkett, J. X. Prochaska, T. Rastogi, V. Reddy Janga, J. Sabater, P. Sakurikar, M. Seifert, L. E. Sherbert, H. Sherwood-Taylor, A. Y. Shih, J. Sick, M. T. Silbiger, S. Singanamalla, L. P. Singer, P. H. Sladen, K. A. Sooley, S. Sornarajah, O. Streicher, P. Teuben, S. W. Thomas, G. R. Tremblay, J. E. H. Turner, V. Terrón, M. H. van Kerkwijk, A. de la Vega, L. L. Watkins, B. A. Weaver, J. B. Whitmore, J. Woillez, V. Zabalza, and Astropy Contributors. The Astropy Project: Building an Open-science Project and Status of the v2.0 Core Package. , 156(3), September 2018.

[5] A Capannolo, F Ferrari, and M Lavagna. Families of Bounded Orbits near Binary Asteroid 65803 Didymos. *Journal of Guidance, Control, and Dynamics*, 42(1), 2019.

[6] F Damme, H Hussmann, and J Oberst. Spacecraft orbit lifetime within two binary near-Earth asteroid systems. *Planetary and Space Science*, 146(January), 2017.

[7] L Dell'Elce, N Baresi, S Naidu, L Benner, and D Scheeres. Numerical investigation of the dynamical environment of 65803 didymos. *Advances in Space Research*, 59(5), 2017.

[8] R. Dymock. *Asteroids and Dwarf Planets and How to Observe Them.* Astronomers' Observing Guides. Springer New York, 2010.

[9] European Space Research and Technology Centre. Asteroid impact mission: Didymos reference model. 2014.

[10] H Goldberg, Ö Karatekin, B Ritter, A Herique, P Tortora, C Prioroc, B Gutierrez, P Martino, I Carnelli, and B Garcia. The juventas cubesat in support of esa's hera mission to the asteroid didymos. In *Small Satellite Conference, Logan, Utah*, 2019.

[11] X Hou and L Liu. On lyapunov families around collinear libration points. *The Astronomical Journal*, 137 (6), 2009.

[12] Isabelle Jean, Arun K. Misra, and Alfred Ng. Solar radiation pressure-compatible trajectories in the vicinity of a binary asteroid. *Journal of Guidance, Control, and Dynamics*, 42(6):1319–1329, 2019.

[13] E Jones, T Oliphant, P Peterson, et al. Scipy: Open source scientific tools for python, 2001, 2016.

[14] R Lasagni Manghi, D Modenini, M Zannoni, and P Tortora. Preliminary orbital analysis for a CubeSat mission to the Didymos binary asteroid system. *Advances in Space Research*, 62(8), 2018.

[15] M List, S Bremer, B Rievers, and H Selig. Modelling of solar radiation pressure effects: Parameter analysis for the microscope mission. *International Journal of Aerospace Engineering*, 2015, 2015.

[16] L McFadden and R Binzel. *Near-Earth Objects*. Gale virtual reference library. Elsevier Science, 2006.

[17] SP Naidu, LAM Benner, M Brozovic, MC Nolan, SJ Ostro, JL Margot, JD Giorgini, T Hirabayashi, DJ Scheeres, P Pravec, et al. Radar observations and a physical model of binary near-Earth asteroid 65803 Didymos, target of the DART mission. *Icarus*, 348(March), 2020.

[18] NASA. *Missions to Asteroids*. URL `https://nssdc.gsfc.nasa.gov/planetary/planets/asteroidpage.html`. Accessed: 20-11-2020.

[19] R Negri and A Prado. Generalizing the bicircular restricted four-body problem. *Journal of Guidance, Control, and Dynamics*, 43(6), 2020.

[20] T Oliveira and A Prado. Search for stable orbits around the binary asteroid systems 1999 KW4 and didymos. *Revista Mexicana de Astronomia y Astrofisica*, 56(1), 2020.

[21] Safety & Security, European Space Agency. The story so far. URL `https://www.esa.int/Safety_Security/Hera/The_story_so_far`. Accessed: 20-11-2020.

[22] DJ Scheeres and F Marzari. Temporary orbital capture of ejecta from comets and asteroids: Application to the Deep Impact experiment. *Astronomy and Astrophysics*, 356(2), 2000.

[23] J Silva Neto, D Sanchez, and A Prado. Co-orbital orbits around the asteroid 65803 didymos (1996 GT). *Space Flight Mechanics Meeting, 2018*, 2018.

[24] S Soldini, S Takanao, H Ikeda, K Wada, T Yuichi, N Hirata, and N Hirata. A generalised methodology for analytic construction of 1:1 resonances around irregular bodies: Application to the asteroid Ryugu's ejecta dynamics. *Planetary and Space Science*, 180(September 2019), 2020.

[25] V Szebehely. Theory of orbits: the restricted three body problem, 1967.

[26] D Villegas Pinto, S Soldini, Y Tsuda, and J Heiligers. Temporary capture of asteroid ejecta into periodic orbits: Application to JAXA's Hayabusa2 impact event. *AIAA Scitech 2020 Forum*, 1 PartF, 2020. doi: 10.2514/6.2020-0221.

[27] K Wakker. *Fundamentals of Astrodynamics*. Institutional Repository. Delft University of Technology, 2015.

[28] W Yu, J Wang, and D Han. Numerical modeling of dust dynamics around small asteroids. *AIAA Space and Astronautics Forum and Exposition, SPACE 2016*, (September), 2016.

[29] Y Yu, P Michel, S Schwartz, S Naidu, and L Benner. Ejecta cloud from the AIDA space project kinetic impact on the secondary of a binary asteroid: I. mechanical environment and dynamical model. *Icarus*, 282, 2017.

[30] Y Yu, P Michel, M Hirabayashi, S Schwartz, Y Zhang, D Richardson, and X Liu. The Dynamical Complexity of Surface Mass Shedding from a Top-shaped Asteroid Near the Critical Spin Limit. *The Astronomical Journal*, 156(2), 2018.

[31] Y Yu, P Michel, M Hirabayashi, and D Richardson. The expansion of debris flow shed from the primary of 65803 Didymos. *Monthly Notices of the Royal Astronomical Society*, 484(1), 2019.

[32] Yun Zhang, Derek C. Richardson, Olivier S. Barnouin, Clara Maurel, Patrick Michel, Stephen R. Schwartz, Ronald Louis Ballouz, Lance A.M. Benner, Shantanu P. Naidu, and Junfeng Li. Creep stability of the proposed AIDA mission target 65803 Didymos: I. Discrete cohesionless granular physics model. *Icarus*, 294:98–123, 2017.